2023

Liquid-liquid phase transitions induced by molecular interconversion in polyamorphic substances

BOSTON UNIVERSITY

GRADUATE SCHOOL OF ARTS AND SCIENCES

Dissertation

LIQUID-LIQUID PHASE TRANSITIONS INDUCED BY MOLECULAR INTERCONVERSION IN POLYAMORPHIC SUBSTANCES

by

MYKOLA SHUMOVSKYI

B.S., Kharkiv National University, Ukraine, 2015
M.S., Kharkiv National University, Ukraine, 2017

Submitted in partial fulfillment of the

requirements for the degree of

Doctor of Philosophy

2023

Approved by

First Reader

Sergey Buldyrev, PhD
Professor of Physics

Second Reader

Andrei Ruckenstein, PhD
Professor of Physics

Third Reader

Karl Ludwig, PhD
Professor of Physics

LIQUID-LIQUID PHASE TRANSITIONS INDUCED BY MOLECULAR INTERCONVERSION IN POLYAMORPHIC SUBSTANCES

MYKOLA SHUMOVSKYI

Boston University, Graduate School of Arts and Sciences, 2023

Major Professor: Sergey Buldyrev, PhD
Professor of Physics

ABSTRACT

Fluid polyamorphism is the existence of different condensed amorphous states in a single-component fluid. It is either found or predicted, usually at extreme conditions, for a broad group of very different substances, including helium, carbon, silicon, phosphorous, sulfur, tellurium, cerium, hydrogen, and tin tetraiodide. This phenomenon is also hypothesized for metastable and deeply supercooled water, presumably located a few degrees below the experimental limit of homogeneous ice formation. In this dissertation, I firstly discuss a fluid composed of two molecular species that may undergo phase segregation or phase amplification when two molecular species may interconvert. Secondly, I investigate the emergence of dissipated structures in mixtures with molecular interconversion in the presence of a source. Lastly, motivated by recent discoveries of the liquid-liquid phase transition in sulfur and hydrogen, I propose a simple model to describe liquid polyamorphism in a variety of chemically reacting fluids. The model combines the ideas of two-state thermodynamics with the maximum-valence approach, in which atoms may form covalent bonds via a reversible reaction, changing their state according to their bond number. By mimicking the va-

lence structure and maximum bond number, z, our model predicts the liquid-liquid phase transition in systems with dimerization ($z = 1$), polymerization ($z = 2$), and gelation ($z > 2$). In particular, I show that when the bonded atoms repel or attract each other stronger than the unbonded atoms, phase separation is coupled to association generating the liquid-liquid phase transition in polyamorphic substances.

Contents

List of Figures

List of Abbreviations

ATP	.....	Adenosine triphosphate
HCS	.....	Hard-core shoulder
HDA	.....	High-Density Amorphous
HDL	.....	High-Density Liquid
HL	.....	Hybrid Lattice
LDA	.....	Low-Density Amorphous
LDL	.....	Low-Density Liquid
LGCP	.....	Liquid-Gas Critical Point
LGPT	.....	Liquid-Gas Phase Transition
LLCP	.....	Liquid-Liquid Critical Point
LLPT	.....	Liquid-Liquid Phase Transition
MD	.....	Molecular Dynamics
PT	.....	Phase transition
TP	.....	Triple point

Chapter 1

Overview of fluid polyamorphism and liquid-liquid phase transitions

1.1 Brief survey and motivation

The existence of two alternative liquid phases in a single-component substance is known as "liquid polyamorphism" (Stanely, 2013; Anisimov et al., 2018b; Tanaka, 2020). A substance may be found to be polyamorphic by experimentally or computationally detecting a liquid-liquid phase transition (LLPT), which could be terminated at a liquid-liquid critical point (LLCP) (Franzese et al., 2001; Sciortino, 2011). Liquid polyamorphism has been observed in a variety of substances including: hydrogen (Ohta et al., 2015; McWilliams et al., 2016; Dzyabura et al., 2013; Zaghoo et al., 2016; Zaghoo and Silvera, 2017), helium (Vollhardt and Wölfle, 1990; Schmitt, 2015), sulfur (Henry et al., 2020), phosphorous (Katayama et al., 2000; Katayama et al., 2004) and liquid carbon (Glosli and Ree, 1999), while being proposed to exist in selenium and tellurium (Brazhkin et al., 1999; Plašienka et al., 2015) and in various oxides (Tanaka, 2020) - *e.g.* silica (Saika-Voivod et al., 2004; Lascaris et al., 2014a; Chen et al., 2017). It has also been hypothesized in supercooled silicon (Sastry and Angell, 2003a; Sciortino, 2011) and in metastable deeply supercooled water below the temperature of spontaneous ice nucleation (Stanely, 2013; Anisimov et al., 2018b; Tanaka, 2020; Holten and Anisimov, 2012; Gallo et al., 2016a; Duška, 2020; Caupin and Anisimov, 2019; Poole et al., 1992; Holten et al., 2014; Debenedetti et al., 2020;

Biddle et al., 2017; Debenedetti, 1998).

The phenomenon of liquid polyamorphism could be understood through the interconversion of the two alternative molecular or supramolecular states via a reversible reaction (Anisimov et al., 2018b; Longo and Anisimov, 2022; Caupin and Anisimov, 2021). While for some polyamorphic systems, like supercooled water, this approach is still being debated, there are substances (such as hydrogen, sulfur, phosphorous, and liquid carbon) where liquid-liquid phase separation is indeed induced by a chemical reaction. For example, it was recently discovered that high-density sulfur, well above the liquid-gas critical pressure (in the range from 0.5 to 2.0 GPa), exhibits a LLPT indicated by a discontinuity in density from a low-density-liquid (LDL) monomer-rich phase to a high-density-liquid (HDL) polymer-rich phase (Henry et al., 2020). This liquid-liquid transition is found in a polymerized state of sulfur (observed above 160 °C at ambient pressure (Sauer and Borst, 1967; Bellissent et al., 1994; Kozhevnikov et al., 2004; Tobolsky and Eisenberg, 1959; Eisenberg and Tobolsky, 1960)). However, with further increase of temperature, as the system approaches the liquid-gas phase transition (LGPT), the polymer chains gradually dissociate. Another liquid-liquid transition accompanied by a chemical reaction has been predicted in hydrogen at extremely high-pressures (Morales et al., 2010; Pierleoni et al., 2016; Geng et al., 2019; Hinz et al., 2020; Cheng et al., 2020), and although the first-order phase transition is still a subject of debate in the literature (Goncharov and Geballe, 2017; Dalladay-Simpson et al., 2016a; Silvera et al., 2017), two liquid phases of hydrogen have been observed, in which liquid-molecular hydrogen (dimers) dissociates into atomistic-metallic hydrogen (Ohta et al., 2015; McWilliams et al., 2016; Dzyabura et al., 2013; Zaghoo et al., 2016; Zaghoo and Silvera, 2017).

In this dissertation, motivated by the recent discoveries of the LLPT in sulfur (Henry et al., 2020) and hydrogen (Ohta et al., 2015; McWilliams et al., 2016;

Dzyabura et al., 2013; Zaghoo et al., 2016; Zaghoo and Silvera, 2017; Dalladay-Simpson et al., 2016b), we propose a simple model to describe liquid polyamorphism in a variety of chemically-reacting fluids. The model combines the ideas of two-state thermodynamics (Anisimov et al., 2018b; Holten et al., 2014) with the maximum-valence approach (Zaccarelli et al., 2005; Speedy and Debenedetti, 1994; Speedy and Debenedetti, 1996), in which atoms may form covalent bonds via a reversible reaction, changing their state according to their bond number. By mimicking the valence structure and maximum bond number, z, our model predicts the LLPT in systems with dimerization ($z = 1$), polymerization ($z = 2$), and gelation ($z > 2$). As an example, we compare the molecular dynamics (MD) simulations with the phase behavior of sulfur. In particular, we show that when the bonded atoms attract each other stronger than to the unbonded atoms, phase separation is coupled to polymerization generating the LLPT in sulfur. Moreover, we show that when the atoms with maximal valence repel atoms with any valence, phase separation is coupled to dimerization ($z = 1$), polymerization ($z = 2$), and gelation ($z > 2$), thus generating the LLPT in polyamorphic substances.

1.2 Techniques used

1.2.1 Lattice Monte-Carlo

We perform mixed Kawasaki-Glauber dynamics on an Ising-spin system in zero field arranged on an $\ell \times \ell \times \ell$ cubic lattice using the conventional Ising model Hamiltonian (Kubo, 1988; Huang, 1987a)

$$H = -\frac{\epsilon}{2} \sum_{i=1}^{\ell^3} \sum_{j \in \Omega(i)} s_i s_j \tag{1.1}$$

where s_i, $s_j = \pm 1$ are spins, $\Omega(i)$ is the set of 6 nearest neighbors of spin i, and ϵ is the interaction energy. The critical temperature of this system is $T_c = 4.5115(1)\epsilon/k_B$ (Heuer, 1993b), where k_B is Boltzmann's constant. We start simulations with a random spin configuration in which $\ell^3/2$ spins are positive and $\ell^3/2$ spins are negative. In addition, we assume that at each MC step the probability of a random spin flip (a Glauber step) is p_r, while the probability of swapping a randomly selected pair of nearest neighbor spins (a Kawasaki step) is $1 - p_r$. Each step is accepted with a standard Metropolis criterion (Metropolis and Ashenhurst, 1963). We introduce a size-independent MC time as $t = n/\ell^3$, where n is the total number of MC steps. The frequency of spin flipping is absorbed into the time step, δt, so the Onsager coefficients, L and M (and consequently p_r), do not depend on temperature.

Note that the MC time must be renormalized if we want to relate it to the physical time $\tilde{t}$ and thus to a certain physical process, *e.g.* diffusion. Assume that in an interval of physical time $\tilde{\tau}$, each pair of spins, representing a pair of neighboring spins (particles), can swap, *i.e.* each particle makes two steps to neighboring lattice sites. The self-diffusion coefficient (mobility) of this process is $M = a^2/(3\tilde{\tau})$. In addition to the diffusion, the particles can interconvert and change from A to B and vice versa. This process occurs with a rate r, which is related to the spin flip probability, p_r by

$r = p_r/[(1-p_r)\tilde{\tau}]$. Then $\tilde{t} = (1-p_r)t\tilde{\tau}$. Having this in mind, in the rest of the dissertation we will use the MC time t.

1.2.2 Molecular Dynamics simulation/Hard-core-shoulder model

The hard-core-shoulder model imitates the Lattice Monte-Carlo model (without the constraints of the lattice) in Molecular Dynamics simulations while simplifying the interactions to allow for much faster computational times. In this case, we study a system initially consisting of an equal number of $N_A = N_B = N/2 = 32,000$ identical hard spheres of type A and B with diameter a. The two species repel each other at a shoulder of length $d = 1.3a$ with energy ΔU , causing the system to phase segregate. We simulate the interactions within the system via event-driven Molecular Dynamics with discrete potentials(Alder and Wainwright, 1959). Additionally, we introduce $N_{ph} = 10,000$ "photons" as an external source of energy, which collide with particles A and B at a distance $b < a$. The photons contain an additional energy, ϵ, which upon collision with particles A or B boost the probability of the interconversion of species ($A \longleftrightarrow B$). In our simulations, this reaction occurs instantaneously, without any metastable intermediate state of either species.

The system is simulated in an $l \times l \times l$ box of length $l = 40a$ with periodic boundaries at temperature $T = \epsilon/k_B$. To regulate the temperature and pressure, we use a Berendsen thermostat and barostat(Berendsen et al., 1984). The collision of photons with species A or B occurs with conservation of momentum, angular momentum, and energy between the pair. The spheres cannot spin, so only the velocities of colliding particles can change.

In the equilibrium formulation, the photons either contain no additional energy, ϵ, or the cross-sectional area of their interaction with the species, b^2, is zero, such that the photons pass through species A or B without interacting. In the nonequilibrium formulation, the photons possess both the additional energy and cross-sectional area necessary to interact and convert species A to B.

The effect of the photons can be summarized as follows: consider a scenario when

a photon collides with particle A. This collision incites an interconversion reaction, such that particle A may change its species to B. Depending on the species of the particles neighboring A, this reaction may be energetically favorable (if, for instance, particle A is surrounded by B-type particles) or it may be energetically costly (if particle A is surrounded by A-type particles). Without an external source of energy, an energetically costly interconversion reaction will violate the conservation laws, such that the particles will recoil and interconversion will not happen. Thus, without the source of energy, this model will lead to phase amplification. However, in the presence of an external source of energy provided by the photons, the interconversion reaction may happen both in favorable or unfavorable conditions, exactly as in the hybrid model.

The particles of type A and B have equal masses m. Accordingly, the unit of time is defined by $a\sqrt{m/\epsilon}$. The reaction rate can be defined as the inverse average time, $1/$, between the collisions of A or B particles with the photons, and as such, it is equal to the mean free path divided by the average relative speed(S. Chapman, 1970):

$$\frac{1}{\tau} = \frac{4b^2 N_{ph}\sqrt{\pi k_B T/m}}{l^3} = a_1 b^2 \sqrt{T} \tag{1.2}$$

where $a_1 = 4N_{ph}\sqrt{\pi k_B/m}/l^3$ is a constant throughout the simulations.

Chapter 2

Phase separation, Phase Amplification and Dissipative structures in substances with molecular interconversion

2.1 Phase separation and phase amplification for equilibrium Kawasaki-Ising Model

Competing Dynamics: The Phenomenon of Phase Amplification - When a fluid, composed of two immiscible molecular species, is quenched at appropriate concentration from a high temperature to a temperature below the critical point of demixing, into the unstable (spinodal) region, the fluid will phase separate into two stable phases - a process known as spinodal decomposition (Cahn, 1965). During spinodal decomposition, if the molecular species may easily interconvert (*e.g.* chiral molecules (Latinwo et al., 2016), chiral crystals (Ricci et al., 2013), or two isomorphs in a polyamorphic fluid (Anisimov et al., 2018a)), then the phenomenon of phase amplification, when one phase grows at the expense of another one, can be observed.

To model this phenomenon, we use the fact that the Ising model for an anisotropic ferromagnet and the lattice gas model for a fluid are mathematically equivalent (Lee and Yang, 1952). Within the same universality class, systems demonstrate the same critical singularities and the same critical equation of state, provided that the appropriately defined order parameters, ϕ, have the same symmetry. The one-component-vector order parameter (ϕ, the magnetization) in the Ising model and the scalar

order parameter ($\phi = 1 - 2\rho$, where ρ is the density) in the lattice gas posses the same symmetry (Kogut, 1979; Senthil and Fisher, 2000). In this work, we consider the incompressible symmetric binary mixture (Xu et al., 2004; Kubo, 1988), a popular version of the lattice gas model, where the conserved order parameter is $\phi = 1 - 2x$, in which x is the fraction of cells occupied by one of the components.

However, while the binary lattice and Ising model are equivalent in thermodynamics, they are fundamentally different in dynamics. The order parameter, the fraction of occupied cells, associated with fluid phase separation is conserved, while magnetization is not conserved. Thus, the order parameters in the binary lattice and Ising model belong to different universality classes in dynamics (Hohenberg and Halperin, 1977). This difference is characterized by the dynamic critical exponent $z = 2$ (Ising-model dynamics) and $z = 4$ (binary-lattice dynamics in the mean-field approximation) (Hohenberg and Halperin, 1977; Das et al., 2006).

To illustrate this difference, consider a binary lattice of particles. In the absence of an external ordering field, but in the presence of fluctuations of density, this system will remain in equilibrium provided that the particles can arrange themselves to minimize the free energy. To do this, the particles will "swap" locations with one another until the energy is minimized. As a result, below the critical temperature of demixing, two equilibrium fluid phases must coexist to conserve the total number of particles (occupied cells). Juxtapose this with the same lattice of up and down spins in the Ising model. Since the positions of the magnetic dipoles are fixed, to approach equilibrium, the spins will "flip" to minimize the free energy. Thus, in the Ising ferromagnet, only one of the alternative magnetizations, positive or negative, will survive - see Fig. 2·1a. Since the interface between the two alternative magnetic phases is energetically costly, eventually, one magnetic domain will win over the other.

Therefore, a phase separating fluid with interconversion of species can be de-

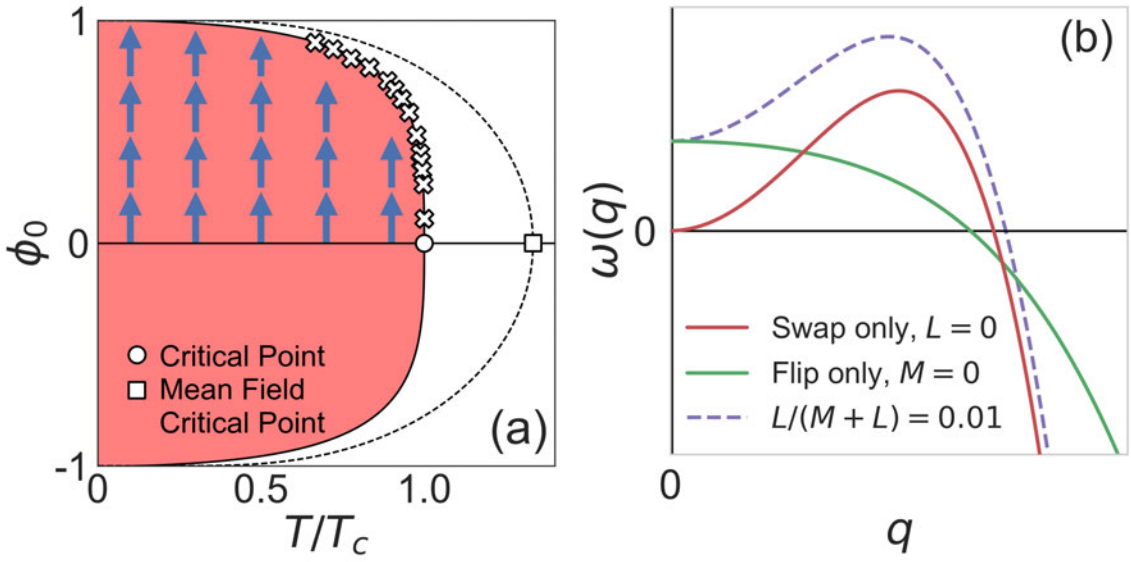

Figure 2·1: (a) The spontaneous equilibrium order parameter ($\phi = \phi_0$) in the lattice-gas / binary-lattice mixture along the liquid-vapor phase coexistence (red domain). One of the two alternative magnetizations ($\phi_0 > 0$ and $\phi_0 < 0$) in the Ising ferromagnet in zero field is shown in the red domain with blue arrows. The solid curve is the crossover from mean-field behavior (dashed) to the asymptotic scaling power law $\phi \propto \Delta\hat{T}^{\beta}$ with $\beta = 0.326$ (Povodyrev et al., 1999; Kim et al., 2003), while the crosses are our simulation data for $\ell = 100$ and averaged over 1,000 realizations. (b) The growth rate solution to Eq. (2.1), known as the amplification factor, for three probabilities: $p_r = 0$ (pure swapping dynamics - $L = 0$), $p_r = 1$ (pure flipping dynamics - $M = 0$), and $p_r = L/(M + L) = 0.01$ (mixed dynamics) after quenching the system into the unstable region at $\Delta\hat{T} = 0.1$.

scribed through a hybrid model combining diffusion-swapping dynamics, where the total number of particles of each species is conserved, and interconversion-flipping dynamics, where the total number of particles of each species is not conserved. By introducing a probability of interconversion, the conservation of the number of particles for a specific type will eventually be broken and the striking phenomenon of phase amplification (or "phase bullying", as originally coined by Latinwo, Stillinger, and Debenedetti (Latinwo et al., 2016)) can be observed.

In order to clarify the physics of phase amplification, we consider a simple Ising system that utilizes a hybrid model combining swapping (conserved order-parameter)

and flipping (nonconserved order-parameter) dynamics distinguished through a certain probability for the order parameter to exhibit interconversion dynamics. The characteristic time evolution equation for the growth of the order parameter, which contains both nonconserved and conserved features, is given by

$$\frac{\partial \phi}{\partial t} = -L\mu + M\nabla^2\mu \tag{2.1}$$

(Cahn, 1965; Cahn and Allen, 1977; Li and Cates, 2020; Longo and Anisimov, 2021) where the exchange chemical potential, μ, is the deviation of the chemical-potential difference between the two species from its equilibrium value - $\mu = 0$. It spatially depends on the order parameter (such that it characterizes local inhomogeneities within the system), the reduced distance to the critical temperature $\Delta\hat{T} = (T_c - T)/T_c$, and the correlation length of fluctuations, ξ. The first term in Eq. (2.1) describes the relaxation of the nonconserved order-parameter dynamics to equilibrium, and the second term describes the relaxation of the conserved order-parameter dynamics to equilibrium. The kinetic Onsager coefficients L and M correspond to the flipping and swapping dynamics respectively. When $M = 0$, the order parameter grows according to pure flipping dynamics, while when $L = 0$, the order parameter grows according to Cahn-Hilliard theory of spinodal decomposition (Cahn, 1965; Cahn and Allen, 1977) (pure swapping dynamics). We define the probability that the system will exhibit interconversion of species as $p_r = L/(M + L)$. The solution to Eq. (2.1) which characterizes the rate of spinodal decomposition, $\omega(q)$, is known as the "amplification factor" (Cahn, 1965; Longo and Anisimov, 2021), and it is illustrated in Fig. 2·1b for three different probabilities. If $p_r = 1$, then, as the system relaxes to equilibrium, eventually one phase will completely eliminate the other one via phase amplification. If $p_r = 0$, the system will reach phase coexistence at equilibrium (no phase amplification), and if $0 < p_r < 1$, we show in this work that the rate of phase amplification

depends on p_r, the system size ℓ, and the distance to the critical temperature $\Delta\hat{T}$.

The domain growth (Mazenko and Valls, 1984) and symmetry breaking in chiral molecules (Latinwo et al., 2016) and in chiral crystals (Ricci et al., 2013) have already been studied. However, phase amplification, the phenomenon of the growth of a nonconserved order parameter, at different interconversion probabilities has not yet been addressed. In this Letter, we report on the results of Monte Carlo (MC) simulations of a simple Ising model that utilizes a hybrid combination of Kawasaki-swapping (Kawasaki, 1966) and Glauber-flipping (Glauber, 1963) dynamics to account for the conserved and nonconserved dynamics of the order parameter respectively. Previous computational studies of this combination have been studied by Glotzer *et al.* (Glotzer et al., 1994; Glotzer et al., 1995), but their model has been shown not to be applicable to equilibrium systems (Lefever et al., 1995; Carati and Lefever, 1997; Lamorgese and Mauri, 2016). In this work, we present an equilibrium formulation of the model proposed by Glotzer *et al.* (Longo and Anisimov, 2021), and we show that under equilibrium conditions, the competition of swapping (Kawasaki) and flipping (Glauber) dynamics produces the phenomenon of phase amplification. We characterize the rate of phase amplification through the probability of Glauber dynamics, system size, and distance to the critical temperature. We also provide scaling arguments for the topological behavior of the resultant structures that occur during phase amplification.

Model Description - We perform mixed Kawasaki-Glauber dynamics on an Ising-spin system in zero field arranged on an $\ell \times \ell \times \ell$ cubic lattice using the conventional Ising model Hamiltonian (Kubo, 1988; Huang, 1987a)

$$H = -\frac{\epsilon}{2} \sum_{i=1}^{\ell^3} \sum_{j \in \Omega(i)} s_i s_j \tag{2.2}$$

where s_i, $s_j = \pm 1$ are spins, $\Omega(i)$ is the set of 6 nearest neighbors of spin i, and ϵ is the interaction energy. The critical temperature of this system is $T_c = 4.5115(1)\epsilon/k_B$ (Heuer, 1993b), where k_B is Boltzmann's constant. We start simulations with a random spin configuration in which $\ell^3/2$ spins are positive and $\ell^3/2$ spins are negative. In addition, we assume that at each MC step the probability of a random spin flip (a Glauber step) is p_r, while the probability of swapping a randomly selected pair of nearest neighbor spins (a Kawasaki step) is $1 - p_r$. Each step is accepted with a standard Metropolis criterion (Metropolis and Ashenhurst, 1963). We introduce a size-independent MC time as $t = n/\ell^3$, where n is the total number of MC steps. The frequency of spin flipping is absorbed into the time step, δt, so the Onsager coefficients, L and M (and consequently p_r), do not depend on temperature.

Results - In zero field, the order parameter for the Ising system generates phase domains when $T < T_c$. These domains will either grow or collapse according to the time evolution equation, Eq. (2.1) - see Fig. 2·1b, such that the competition between the two types of dynamics determines the initial growth of these domains. For a hybrid model of Glauber and Kawasaki dynamics, this competition eventually results in one phase completely eliminating the other - see Fig. 2·2a. However, the rate of phase amplification depends on the probability for the system to follow Glauber (nonconserved) order-parameter dynamics, see Fig. 2·2(b-d) where the phenomenon of phase amplification is shown for different interconversion probabilities from pure Glauber, $p_r = 1$, to extremely low probability $p_r = 1.0 \times 10^{-7}$. For this extremely low probability, most realizations just fluctuate around the average value of the order parameter, $\langle |\phi| \rangle = 0$. In principle, any nonconserved order-parameter dynamics, even with an extremely small probability, may eventually lead to phase amplification, but this is only true for an extremely large computational (or observational) time. For a certain low probability, these conditions would not be achievable in any computational

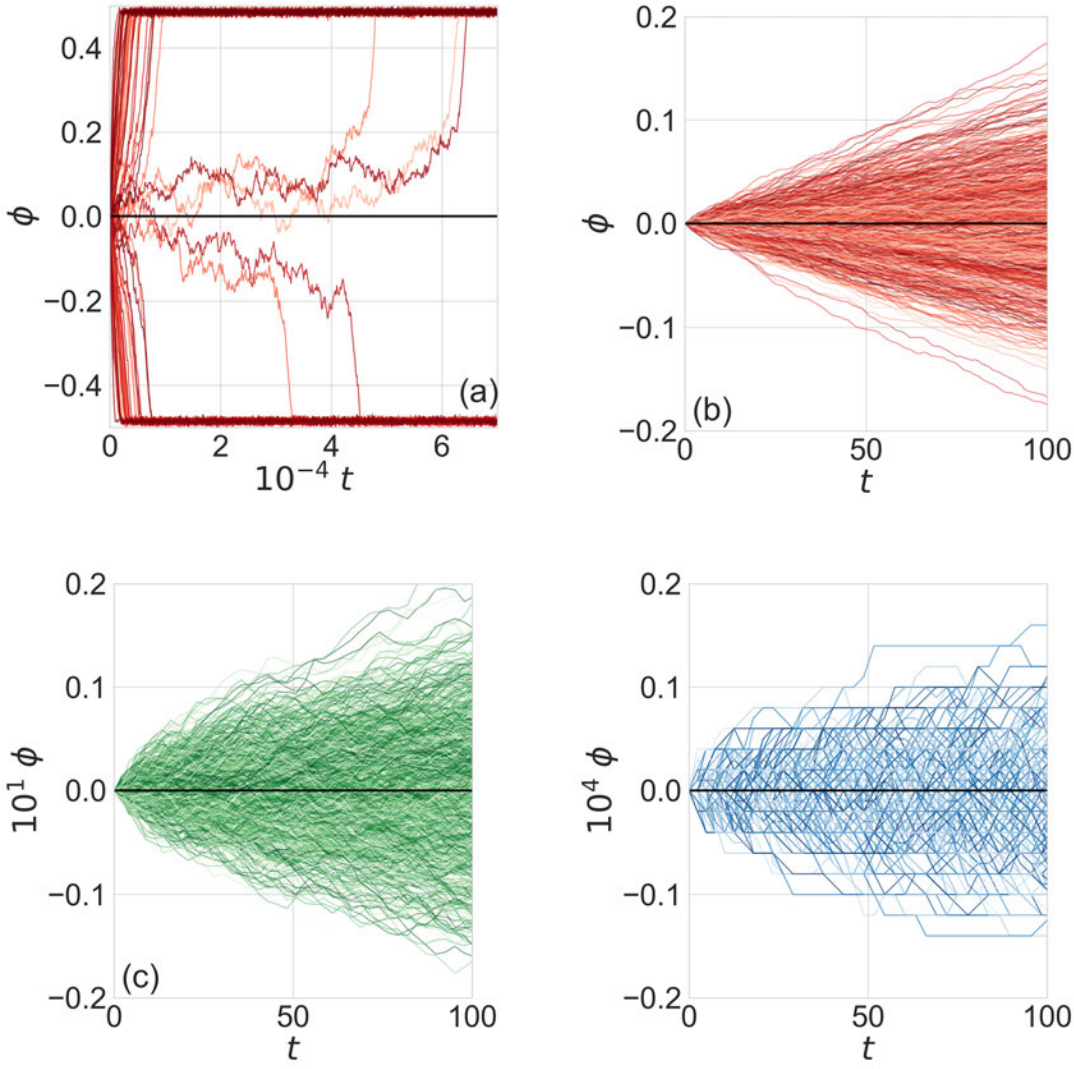

Figure 2·2: Phase amplification - the growth of the order parameter for different probabilities of Glauber dynamics at a system size $\ell = 100$. (a) Full-time behavior, $T = 4.4$ and 100 realizations, $p_r = 1$; (b-d) initial time behavior, $T = 4.0$ and 1,000 realizations: (b) $p_r = 1.0$, (c) $p_r = 0.1$, and (d) $p_r = 1.0 \times 10^{-7}$. The solid horizontal line, $\phi = 0$, corresponds to Kawasaki dynamics, $p_r = 0$.

or experimental studies.

One can notice from Fig. 2·2a, that even for systems with pure Glauber dynamics, there is a small fraction of realizations that survive for a long time, but eventually, one phase completely eliminates the other. We attribute this effect to the accidental formation of zero-curvature interfaces during the domain growth. We observed that at least two types of zero curvature interfaces are possible: a planar interface and a Schwarz-P interface (Schwarz, 1972). Of these two types, only the planar surface corresponds to stable equilibrium against phase amplification. In this case, a bump with positive curvature produced by a fluctuation shrinks, while a cavity with negative curvature will flatten. In periodic boundary conditions, this interface forms a strip with two parallel surfaces. Fluctuations will only produce random changes to the width of this strip, $w = \ell\Delta\hat{\phi}/2$ (where $\Delta\hat{\phi} = 1 - \phi/\phi_0$ is the reduced deviation from the equilibrium order parameter), corresponding to the longer lasting realizations in Fig. 2·2a. Eventually, when w becomes comparable to ξ, the domain will be punctured and a hole, with average positive curvature due to the growing domain, will be formed causing the strip to quickly disappear. In periodic boundary conditions, or locally, the growing domains can form other surfaces with zero curvature, for example, a Schwarz-P surface (Schwarz, 1972). This is especially likely when p_r is small and the system has time to evolve largely according to Kawasaki dynamics. Once such an interface is formed, the amplification process is "frozen", and the order parameter follows random walk behavior. However, such interfaces are unstable against fluctuations and will collapse when the growing phase forms an interface with negative curvature to break the phase domain of the receding phase.

One of the most evident characteristic of phase amplification is the increase in the width of the distribution of the growth rates as the Glauber-dynamics probability increases. Assuming that the distribution of the average rates (slopes) in Fig. 2·2(b-

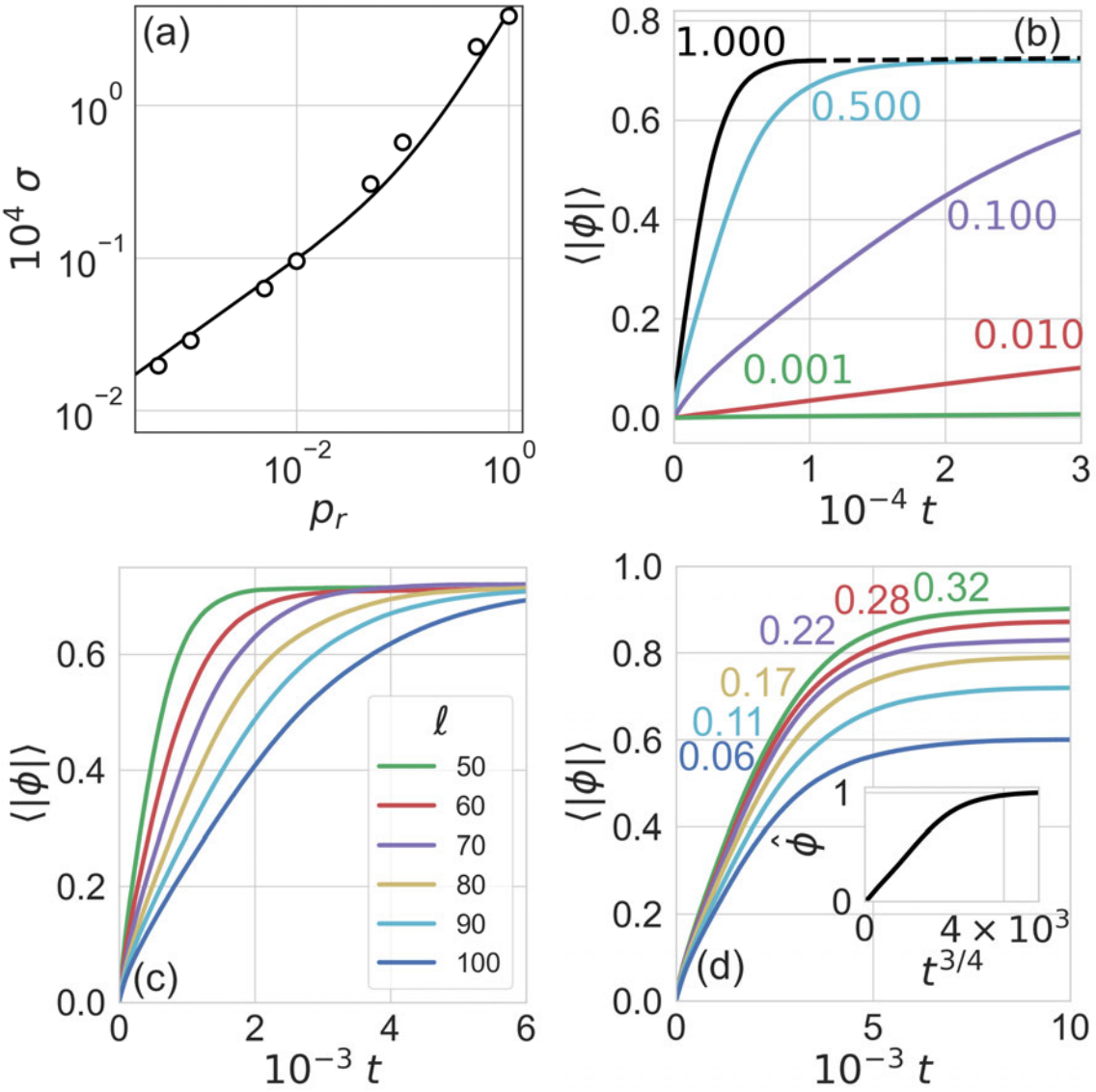

Figure 2·3: The evolution of the order parameter during phase amplification. (a) The RMS of the distribution of the growth rates for different probabilities captured at the same time, $t = 300$. The solid curve is the crossover between $\sigma \propto \sqrt{p_r}$ and $\sigma \propto p_r$, approximated as $\sigma = a\sqrt{p_r}(1+bp_r)/(1+\sqrt{p_r})$. (b-d) The growth of the order parameter for different (b) probabilities at $\Delta\hat{T} = 0.11$ and $\ell = 100$, (c) system sizes at $p_r = 1.0$ and $\Delta\hat{T} = 0.11$, and (d) distances to the critical point at $p_r = 1.0$ and $\ell = 100$; the colored values in (b,d) correspond to the colored curves of different p_r and $\Delta\hat{T}$ respectively. The inset of (d) shows the power law for the initial growth of the reduced order parameter, $\phi/\phi_0 \propto t^{3/4}$.

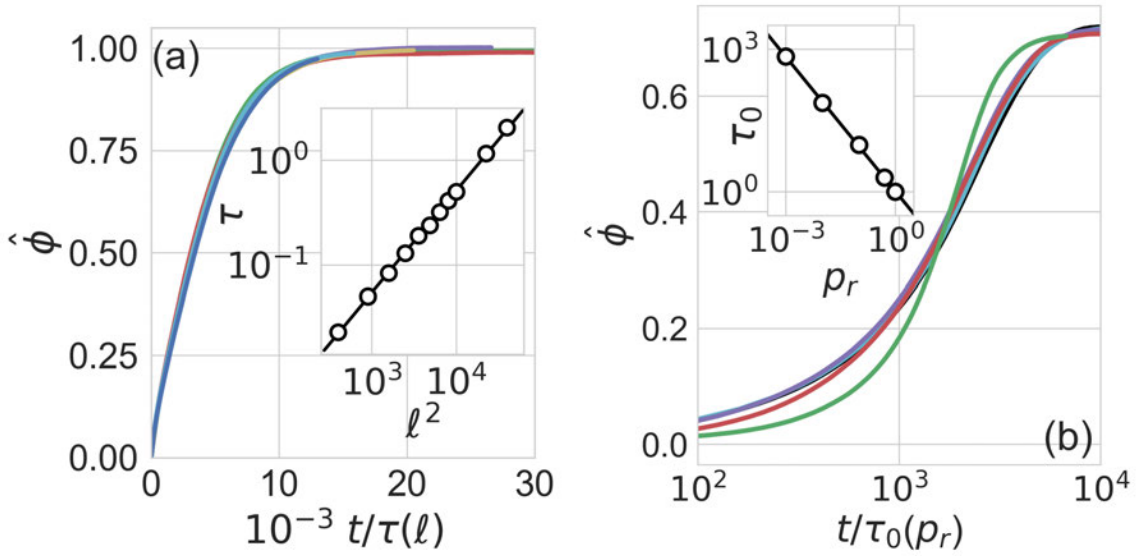

Figure 2·4: Scaling properties of the growth of the reduced order parameter, $\hat{\phi} = \langle|\phi|\rangle/\phi_0$. (a) The order parameter growth with time rescaled by system size. The size dependence of the rescaling parameter, $\tau(\ell)$, is shown in the inset; in the log-log scale with a slope of 1. The colors are the same as in Fig. 2·3c. (b) The order parameter growth with time rescaled by probability; the rescaling parameter $\tau_0(p_r)$, inversely proportional to the probability, is shown in the inset. The colors are the same as in Fig. 2·3b.

d) is Gaussian, we show in Fig. 2·3a that the standard deviation of this distribution (calculated at the same time, $t = 300$) changes from $\sigma \propto \sqrt{p_r}$ to $\sigma \propto p_r$ as the system transitions from Kawasaki to Glauber dynamic behavior. Next, we study the absolute value of the order parameter, averaged over 1000 independent realizations of the evolution, as a function of the three key parameters: Glauber probability p_r, system size ℓ (**?**), and distance to the critical point $\Delta\hat{T}$. As shown in Fig. 2·3(b-d), phase amplification is faster for larger p_r, smaller ℓ, and further distance to the critical point (larger $\Delta\hat{T}$).

By reducing the order parameter by its equilibrium value ($\hat{\phi} = \langle|\phi|\rangle/\phi_0$) and rescaling the time as $t/\tau(\ell)$ the system-size and temperature dependent $\phi(t)$ are collapsed as shown in Fig. 2·4a; the characteristic time $\tau(\ell)$ is proportional to ℓ^2 as shown in the inset for $p_r = 1$. After introducing another characteristic scaling time

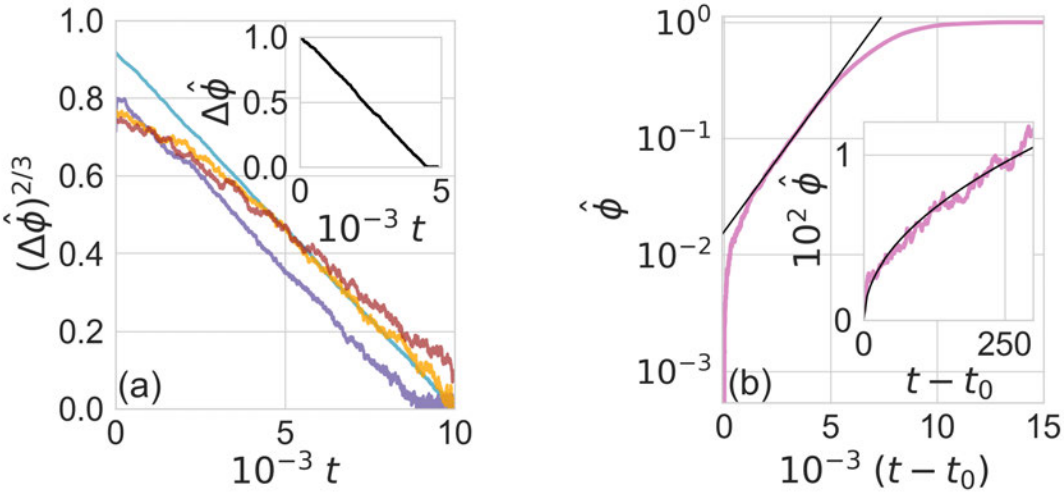

Figure 2·5: Topological characteristics of the time dependence of phase amplification for $\ell = 100$. (a) For spherical domains, the reduced deviation from the equilibrium order parameter, $\Delta\hat{\phi} = 1 - \phi/\phi_0$ scales as $t^{3/2}$. This is shown for temperatures, $\Delta\hat{T}$, as: 0.11 (cyan), 0.025 (purple), 0.014 (orange), and 0.009 (brown). The inset shows the effect for a cylindrical domain at $\Delta\hat{T} = 0.11$. (b) A zero curvature Schwarz-P interface is initially formed by simulating a system with Kawasaki dynamics ($p_r = 0$) for a long time. At $t - t_0 = 0$, the system obtains Glauber dynamics ($p_r = 1$) and the collapse of one of the phases is shown. Amplification transitions from random-walk behavior, $\sqrt{t}$, at short times (see inset) to exponential behavior before saturation, shown by the straight line.

$\tau(p_r)$, for relatively large probability ($p_r \geq 0.01$), we are able to collapse the order parameter growth in a set of curves which cross at the same inflection point as shown on Fig. 2·4b. As a result, for relatively large p_r, we may neglect the effects of Kawasaki dynamics on the system and develop scaling arguments to describe the growth of the order parameter under pure Glauber dynamics.

Scaling Analysis of Phase Amplification for Large p_r - To develop scaling arguments for the growth of the order parameter, we have observed that phase amplification occurs when one phase domain forms an interface with negative curvature against another, such that domains with positive curvature will quickly disappear. In

Fig. 2·5a, we illustrate this process by generating a system in the initial configuration of spherical or cylindrical domains and evolve the system under pure Glauber dynamics. Our simulations show that phase amplification of these topologies occurs with rates: $\phi \propto t^{3/2}$ and $\phi \propto t$ for the sphere and cylinder respectively. This observation is a result of the Kelvin theory (Huang, 1987a; Allen and Cahn, 1979) that the radius of curvature between domains grows with time as $1/q \sim \sqrt{t}$. Indeed, it is possible to show that the domain encapsulated by the convex surface with positive curvature shrinks, and eventually disappears at time $t = t_f$, so that the net order parameter of the system approaches its equilibrium value ϕ_0 as $\Delta\hat{\phi} \propto (t_f - t)^{(d^*+1)/2}$, where $d^* = d - 1$ is the dimension of the interface, *i.e.* $d^* = 2$ for a spherical domain and $d^* = 1$ for a cylindrical domain.

Based on our observations of the growth of individual domains, we may quantify the global dynamics of phase amplification by considering the shrinking and growing of multiple domains. Consider the number of growing phase domains as $(\ell q)^d$, where ℓ is the linear size of the system, q is the characteristic curvature (wave number) of the domain's interface, and d is the dimensionality of the space in which the domain may grow. If we neglect the interaction between different domains, the root-mean-square (RMS) fluctuation of the number of shrinking or growing domains with positive or negative curvature per unit volume is $\sqrt{(\ell q)^d}/\ell^d$. To obtain the growth rate of the average order parameter, this factor must be multiplied by the growth rate (υ/t) of the phase domain volume ($\upsilon \propto q^{-d}$). From our observations of Fig. 2·5a, the size of the domains will grow as a square root of time, $t \propto q^{-2}$, then $\upsilon/t \propto 1/q^{d-2}$. Thus, the growth rate of the averaged absolute value of the order parameter is $\partial\langle|\phi|\rangle/\partial t \propto \ell^{-d/2} q^{-d/2+2}$, and as a function of time this is equivalent to $\partial\langle|\phi|\rangle/\partial t \propto \ell^{-d/2} t^{d/4-1}$. Integrating gives

$$\langle|\phi(t,\ell,T)|\rangle = A\phi_0(T)\left(\frac{t}{\tau}\right)^{d/4} \tag{2.3}$$

where the characteristic time $\tau = \tau_0 \ell^2$, with τ_0 being inversely proportional to p_r (see the inset of Fig. 2·4b), and $\phi_0(T)$ is the equilibrium value of the order parameter. The amplitude, A, is practically independent of temperature. It can be shown from the Kelvin equation that $A \propto \sigma\xi/\phi_0^2$ (Huang, 1987a), where σ is the interfacial tension. This combination is a constant in mean-field theory in which $\sigma \propto \phi_0^3$ and $\xi \propto \phi_0^{-1}$, while in the Ornstein-Zernike approximation of scaling theory $\sigma \propto \xi^{-2}$ and $\phi_0^2 \propto \xi^{-1}$ (Fisher, 1983; Anisimov and Bertrand, 2010). Thus, for all practical purposes, A can be incorporated as a constant factor in τ. Eq. (2.3), as demonstrated in Fig. 2·4a, is strongly supported by the simulation data. It is shown that the growth of the average order parameter, in $d = 3$ space, closely follows the scaling law $\langle|\phi|\rangle \propto t^{3/4}$ for $t \ll \tau$ - see the inset of Fig. 2·3d - while, for $t \gg \tau$, it is constant. Therefore, Eq. (2.3) can be presented in the scaling form $\langle|\phi|\rangle/\phi_0(T) = f(X)$, where $X = t/\tau(\ell)$ and $f(X)$ is a scaling function such that $f(X) \to X^{d/4}$ for $X \ll 1$ and $f(X) = 1$ for $X \gg 1$.

Observations of Phase Amplification for Small p_r - While systems simulated with relatively large Glauber probabilities ($p_r \geq 0.01$) all collapse to the same master curve, as shown in Fig. 2·4b, systems with relatively small probabilities ($p_r < 0.01$) have a larger average amplification rate (slope) at the inflection point. Therefore, for large p_r the time evolution of the phase domain is controlled by fast, local interconversion due to Glauber dynamics, rather than the slow, global diffusion due to Kawasaki dynamics, which only dominates at very small Glauber-interconversion probabilities ($p_r < 0.01$). We attribute the dramatic change in the amplification rate, shown by the deviation from the master curve in Fig. 2·4b, to the increased chance of systems entering a metastable zero-curvature phase-domain state for smaller p_r. We clarify the effect of a system entering this metastable state in Fig. 2·5b, by allowing the system to reach an equilibrium Schwarz-P interface under Kawasaki dynamics ($p_r = 0$). The collapse of the Schwarz-P interface occurs after switching the system to Glauber

dynamics ($p_r = 1$) at $t = t_0$. When a zero curvature interface is first formed due to Kawasaki dynamics, then (no matter how small the Glauber probability, p_r) Glauber dynamics will proceed until, eventually, one of the phases will disappear. In this case, we use a renormalized time $t_G = tp_r$, which essentially counts only the Glauber steps. The sigmoidal shape of this curve shows a crossover from random, square root behavior (shown in the inset of Fig. 2·5b) corresponding to the initial random walk of the interface near unstable equilibrium to the quick exponential amplification when a part of the interface develops non-zero curvature. This phenomenon explains the increase in the rate of the growth of the order parameter for the small probability of Glauber dynamics in Fig. 2·4b through the transformation of t to $t_G = t/\tau_0 \propto p_r$.

Conclusion - In this work, we conceptualize the phenomenon of phase amplification, the growth of one phase at the expense of another one, and quantitatively characterize the speed of phase amplification through scaling laws based on the Kelvin equation. We simulate this phenomenon using a hybrid model, which combines Glauber-interconversion and Kawasaki-diffusion dynamics, in an Ising system. The developed approach is applicable to a broad spectrum of Ising-like systems with mixed dynamics. Such systems include ferromagnets, ferroelectrics, liquid crystals, and materials with order-disorder transitions and chemical reactions. For example, the developed approach explains the results of the first computational study of phase amplification in chiral crystals (Ricci et al., 2013), and can also be used to describe chiral amplification in a mixture of interconverting enantiomers (Latinwo et al., 2016) and real fluids (lacking the symmetry of the lattice gas (Anisimov and Wang, 2006)) - if they exhibit interconversion. In the future, we are interested in investigating phase amplification in polyamorphic liquids (Anisimov et al., 2018a) and in systems with coupled order parameters (Takae and Tanaka, 2020).

2.2 Phase separation and phase amplification for non-equilibrium Kawasaki-Ising Model (Hybrid-Lattice model)

This model was introduced, in its equilibrium formulation, in ref. (Shumovskyi et al., 2021), and the nonequilibrium formulation was introduced, and qualitatively considered, in ref. (Longo and Anisimov, 2022). To model diffusion and interconversion dynamics in a binary system, we consider a simple lattice model where the particles of different types are represented by spins of different orientations. Diffusion is simulated by "swapping" a pair of randomly selected neighboring spins and interconversion is simulated by "flipping" a spin at a randomly selected lattice cite. At each MC step the probability that a random spin will attempt to flip is p_r, while swapping a randomly selected pair of nearest neighbor spins will be attempted with probability $1 - p_r$. This step is accepted according to the standard Metropolis criterion (Metropolis and Ashenhurst, 1963). In the nonequilibrium formulation of the HL model, an additional energy, E, due to the external source of forced interconversion is incorporated into the Boltzmann factor for the Metropolis criterion of a spin flip as $p \sim \exp\{[-(U - E)/k_B T]\}$, where U is the difference in internal energy of the system for this step. When E = 0, the system evolves according to the equilibrium formulation detailed in ref. (Shumovskyi et al., 2021), which leads to phase amplification. If $E > 0$ and is large enough to overcome natural interconversion (and, consequently, phase amplification), then steady-state microphase separation occurs. The energy source, E, reduces the thermodynamic energy barrier between inhomogeneous and phase separated states. Thus, it promotes interconversion to an equal composition of species in opposition to natural interconversion where, in general, the relative population of interconverting species varies with thermodynamic conditions. For energy $E \geq 12$, the external source of forced interconversion is always greater than ΔU (cubic lattice in 3-d) such that spin interconversion in the Metropolis criterion

is always accepted. This scenario makes this model equivalent to the nonequilibrium binary-lattice model (Glotzer et al., 1994; Glotzer et al., 1995). For the diffusion dynamics, the spin-swap step is performed according to the standard Metropolis criterion without any additional energy source, such that diffusion is the same in both the equilibrium and nonequilibrium formulations of this model. For more information about the HL model see ref. (Longo and Anisimov, 2022).

The effect of the source of forced interconversion is introduced into the HL model through a tunable imbalance in the internal energy via the energy of forced interconversion (E), such that the source boosts the probability for two alternative species to interconvert into equal amounts. If forced interconversion is not strong enough to overcome natural interconversion (which corresponds to equilibrium conditions), then phase amplification (the growth of one stable phase at the expense of the other) is observed, provided that the natural interconversion probability is significant. If forced interconversion overcomes natural interconversion by a sufficient amount, we observe that the locally phase-separated domains stop growing upon reaching a characteristic size, as illustrated in Fig. 2·6a. We define the temperature and energy at which this occurs as the "onset" of microphase separation (T and E^*). As shown in Fig. 2·6b and Fig. 2·6c, for temperatures and energies, $T > T^*$ and $E > E^*$ (for a given probability, p_r), dissipative structures are observed and the steady-state domain size decreases as the energy of forced interconversion increases and as the temperature becomes closer to the critical temperature of demixing, T_c. We find that the dissipative domain structure has the form of spatially-modulated stripes due to the symmetry and boundary conditions of the lattice on which the MC simulations are performed. As shown by the simulation snapshots in Fig. 1b, the striped pattern becomes more disordered when the domain size becomes comparable with the correlation length of concentration fluctuations.

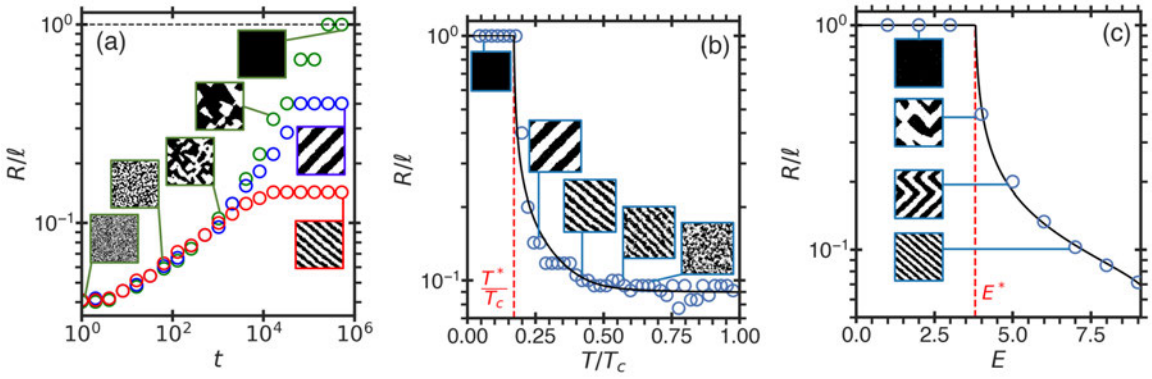

Figure 2·6: Effect of forced interconversion on domain size, R, normalized by the system size, l, in the HL model. (a) The time dependence of the domain growth for energy source $E = 5$ and interconversion probability $p_r = 1/128$ at $T/T_c = 0.24$ (green), $T/T_c = 0.27$ (blue), and $T/T_c = 0.40$ (red), where $T_c = 4.511$ (Heuer, 1993a). The horizontal dashed line indicates the size of the simulation box, $R = l$. (b) Temperature dependence of the steady-state domain size for $E = 5$ and $p_r = 1/128$. The vertical dashed line indicates the onset temperature, T^*/T_c. (c) Dependence of the steady-state domain size on the energy of forced interconversion for $p_r = 1/256$ and $T/T_c = 0.31$. The vertical dashed line denotes the onset source energy, E . In (a-c), the system is simulated on a 3-dimensional lattice of size $l = 100$. The open circles are the results of MC simulations, the images are snapshots of the system for selected conditions, and the curves are the theoretical predictions. In (a-c), black denotes up-spins and white denotes down-spins.

2.3 Phase separation, phase amplification and formation of dissipative structures for Hard-Core shoulder model with or without a source

Unlike the previous examples, this model, which has not been considered before, utilizes a tunable source of forced interconversion, implemented through the interactions with an external flux of energy carrying agents. In biological systems, these agents can be thought of as ATP molecules, which change the conformation of a protein between two phase-segregating states. We consider a system initially consisting of an equal number of $N_A = N_B = N/2 = 32,000$ identical hard spheres of type A and B with diameter σ. While all particles repel each other as hard spheres with diameter σ, phase segregation is generated by the additional repulsion between A and B particles via a square shoulder potential at distance $d = 1.3\sigma$, with energy ϵ_0. We simulate the interactions within the system via event-driven MD with discontinuous potentials (Alder and Wainwright, 1959; Rapaport, 2004). Additionally, we introduce $N_{ag} = 10,000$ agents as an external source of energy, which collide with particles A and B at a distance $b \leq \sigma$. The agents contain an additional energy ϵ (measured in units of ϵ_0), which upon collision with particles A or B boosts the probability of species interconversion ($A \Longleftrightarrow B$). Physically, can be regarded as an external energy carried by an ATP molecule or another active agent, which can compensate the effect of the heat of mixing arising from interconversion. In our simulations, this reaction occurs instantaneously, without any metastable intermediate state of either species.

The systems considered in this work are simulated in an $l \times l \times l$ box of length $l = 40\sigma$ with periodic boundaries at temperature T, measured in units of ϵ_0/k_B. To regulate the temperature, we use a Berendsen thermostat (Berendsen et al., 1984). The collision of the agents with species A or B occurs with conservation of linear and angular momentum of the pair as well as with total potential energy change, ΔU.

The total energy is composed of potential, kinetic, and external energy, in which the external energy is incorporated into the kinetic energy of the colliding particles. The equilibrium formulation occurs with conservation of energy, such that $\epsilon = 0$.

In the equilibrium formulation, the agents either contain no additional energy, ϵ, or the cross-sectional area of their interaction with the species, b^2, is zero, such that the agents pass through species A or B without interacting. Physically, this corresponds to a scenario when the energy is unable to transfer from the agents to the species in the system. In the nonequilibrium formulation, the agents possess both the additional energy and cross-sectional area necessary to interact and convert species A to B and vice-versa. Without an external source of energy, an energetically costly interconversion reaction violates the conservation laws, so that the particles will recoil and interconversion will not happen. However, in the presence of an external source of energy, provided by the agents, the interconversion reaction may happen both in favorable or unfavorable conditions, just as in the HL model.

The particles (A, B, and the agents) have equal masses m, and the simulation time is measured in units of $\sigma\sqrt{m/\epsilon_0}$. Overall, in the HCS model, the system is a dense fluid of hard spheres with a molecular mobility, $M \sim \sqrt{T}$, and interconversion rate proportional to the interaction cross section, b^2.

In the HCS model, non-relativistic energy-carrying particles are introduced as a source of forced interconversion. They carry energy, ϵ, and transfer this energy via molecular collisions with cross-sectional area b^2. When the additional particles carry no extra energy, $\epsilon = 0$, only natural interconversion, with a probability b, will occur. However, due to the external source of energy provided by the particles, forced interconversion will occur just like in the previously considered models. Similar to those models, in the HCS model, the characteristic domain size decreases as a function of temperature and interconversion probability, b, as depicted in Fig. 2·7. In this case,

when $b = 0$, then regardless of ϵ no interconversion will be possible. For conditions $b < b* \sim 0.02$ at $T < T^{=0.22T_c}$ and $\epsilon <^* = 10$, corresponding to the onset of microphase separation, the system enters a transient state with an interface, as illustrated by the simulation snapshots in Fig. 2·7b.

We note that below the onset of microphase separation, the characteristic steady-state domain size is comparable to the size of the simulation box, $l \sim 1/q^*$. Consequently, the onset conditions for all models depends on the system size. In addition, for small system sizes phase amplification occurs faster than for large systems, such that instead of entering a transient state below the onset, the system may undergo phase amplification. As observed in the HCS model, for large system sizes, in the microphase separation region, one could observe more regular structures, like the nonequilibrium spatially-modulated stripes observed in the HL model. The snapshots, presented in Fig. 2·7 demonstrate that the off-lattice MD simulations produce nonequilibrium bicontinuous "microemulsion" structures.

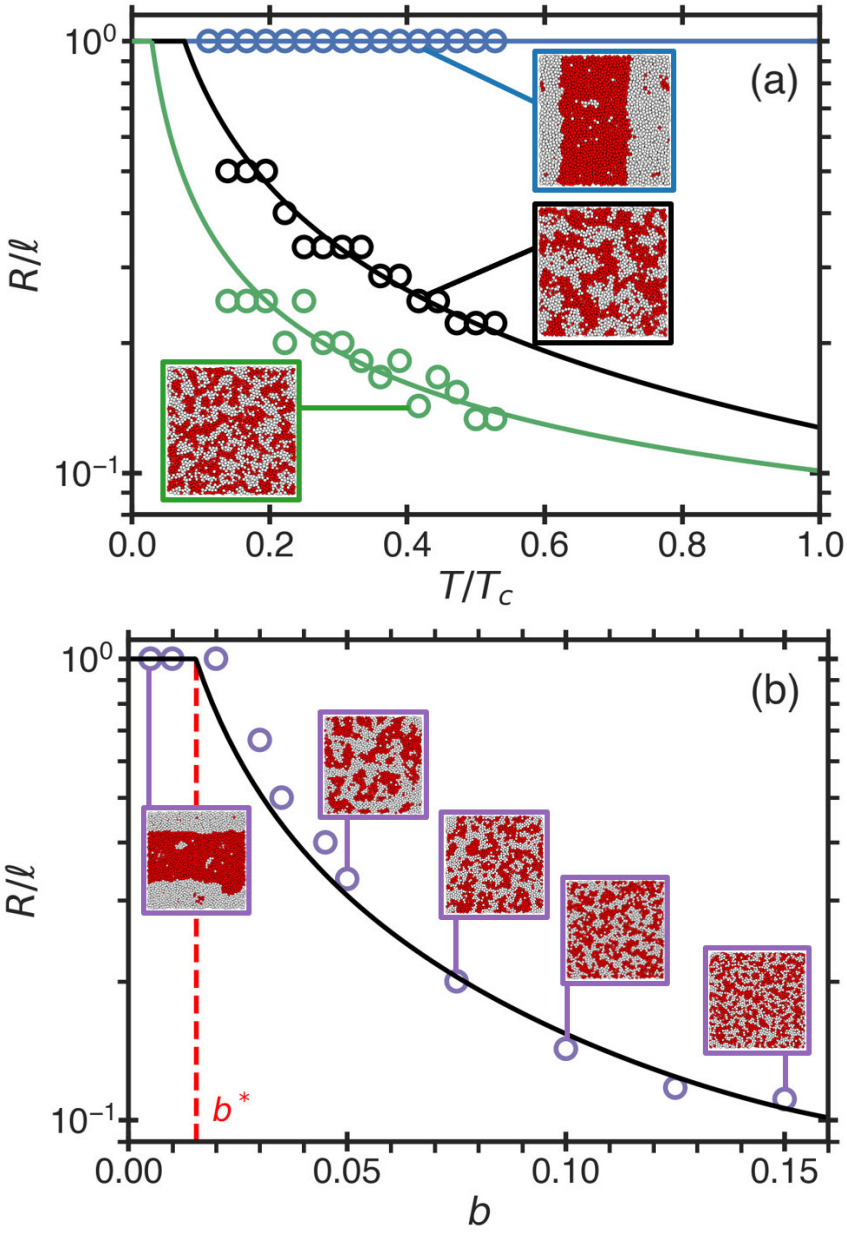

Figure 2·7: Steady-state domain size, R, normalized by the size of the system, l, in the HCS model. (a) The temperature-dependence of the normalized steady-state domain size for $b = 0.005$ (blue), $b = 0.050$ (black), and $b = 0.075$ (green) at $\epsilon = 10$. (b) The normalized steady-state domain size as a function of interconversion probability, b, for the energy source $\epsilon = 12$ and $T/T_c = 0.22$, where $T_c = 3.6 \pm 0.05$. The vertical dashed line indicates the onset interconversion probability, b. In (a) and (b), the open circles correspond to simulation of $64,000$ particles, the curves correspond to the theoretical predictions, and the images show snapshots of the system simulated at the indicated conditions

Chapter 3

Structure factor of a phase separating binary mixture with natural and forceful interconversion of species

3.1 Introduction

C. Austin Angell's pioneering work published 50 years ago hypothesized that the thermodynamic anomalies of liquid water could be attributed to the existence of two supramolecular states (Angell, 1971). Later, this idea was further developed to predict liquid-liquid phase separation in supercooled water below the temperature of homogeneous ice formation (Angell, 2004; Gallo et al., 2016b), as well as in the vitreous state of various substances (Sastry and Angell, 2003b; Xu et al., 2006; Bhat et al., 2007; Xu et al., 2009; Lascaris et al., 2014b; Lascaris et al., 2015). This phenomenon, known as "liquid and glassy polyamorphism" (Poole et al., 1997; Tanaka, 2020), could be attributed to the interconversion between two alternative molecular or supramolecular states (Anisimov et al., 2018a). In this work, we investigate the effects of interconversion between alternative species in a binary mixture on the phase separation and phase domain growth.

Previous studies of a hybrid Ising/lattice-gas model exhibiting both interconversion and diffusion dynamics (Shumovskyi et al., 2021) and a chiral model with interconversion of species (Petsev et al., 2021; Uralcan et al., 2021) have demonstrated that interconversion dynamics breaks the symmetry of phase separation. As a result,

depending on the rate of interconversion, to circumvent the energetically unfavorable formation of an interface, one phase will grow at the expense of the other, a phenomenon known as "phase amplification" (Shumovskyi et al., 2021; Longo and Anisimov, 2021). However, if the alternative species are forced to interconvert due to an external source, then the formation of interfaces between species may become more favorable and the system may phase separate into steady-state microphase domains (Longo and Anisimov, 2021). Previous studies of a phase separating binary-lattice in the presence of an external interconversion force (Glotzer et al., 1994; Glotzer et al., 1995; Christensen et al., 1996) and a chiral model with dissipative intermolecular forces (Uralcan et al., 2021) have demonstrated steady-state microphase separation.

In this work, we consider a binary mixture that, when quenched along critical composition below the critical temperature of demixing, will phase separate via spinodal decomposition (Cahn, 1965). Simultaneously, the alternative species may interconvert either naturally or forcefully. To characterize the formation of phase domains, we calculate the temporal evolution of the structure factor for the concentration fluctuations. We describe the time-dependent structure factor through two characteristic wavenumbers corresponding to the maximum and lower cut-off wavenumbers in the characteristic growth rate. We compare the theory to simulations of a nonequilibrium hybrid Ising/lattice-gas model exhibiting natural and forceful interconversion in addition to diffusion and obtain a qualitative agreement.

3.2 Modified Cahn-Hilliard-Cook Theory

In this section, we generalize the Cahn-Hilliard theory of spinodal decomposition to allow for both natural and forceful interconversion of species and derive the structure factor for concentration fluctuations.

3.2.1 Generalized Spinodal Decomposition

The effect of interconversion on the temporal evolution of the concentration for a binary mixture of species A and B in the presence of interconversion is given in the simplest form (Longo and Anisimov, 2021) as

$$\frac{\partial \hat{c}_A}{\partial t} = M\nabla^2\hat{\mu} - L\hat{\mu} - K\hat{c}_A \tag{3.1}$$

where $\hat{c}_A$ is the order parameter, related to the physical concentration of species A by $\hat{c}_A = 2c_A - 1$, M and L are kinetic coefficients for the diffusion and natural (spontaneous) interconversion dynamics respectively, and the third term is an external source of forceful interconversion. We consider the case when interconversion, both natural and forceful, occurs through a reaction $A<=>B$ where K is the forward and reverse reaction rate. Physically, a source of forceful interconversion could be introduced via irradiation through photons (Enrique and Bellon, 2001) which promote interconversion of species or it could be introduced through a flux of matter (Verdasca et al., 1995). In the absence of interconversion, when $L = 0$ and $K = 0$, then Eq. (3.1) reduces to the Cahn-Hilliard theory (Cahn, 1965). Lastly, the reduced chemical potential difference, $\hat{\mu} = \hat{\mu}_A - \hat{\mu}_B$, is found from the variational derivative of the dimensionless Landau-Ginzburg free-energy functional (Longo and Anisimov, 2021) as

$$\hat{\mu} = \frac{\mu}{k_{\mathrm{B}}T_{\mathrm{c}}} = \frac{1}{2}(1 + \Delta\hat{T}) \ln\left(\frac{1+\hat{c}_A}{1-\hat{c}_A}\right) - \hat{c}_A - \kappa\nabla^2\hat{c}_A \tag{3.2}$$

where the reduced distance to the critical temperature, $\Delta\hat{T} = 1 - T/T_{\mathrm{c}}$, is negative in the spinodal (unstable) region, k_B is Boltzmann's constant, and κ is the square of the range of intermolecular interactions. In this work, we adopt $\kappa = 1$ in the units of the square of the molecular size. Expanding Eq. (3.2) to first order and analytically evaluating Eq. (3.1) via a Fourier transform, the characteristic growth rate, known as the "amplification factor" (Shumovskyi et al., 2021; Longo and Anisimov, 2021;

Cahn, 1965), for spinodal decomposition in the presence of interconversion may be written in the form (Longo and Anisimov, 2021)

$$\omega(q,t) = M\kappa q_m^2(t)[q_m^2(t) - 2q_-^2] - M\kappa[q^2 - q_m^2(t)]^2 \tag{3.3}$$

where the two characteristic wavenumbers, q_m and q_-, are the maximum and the lower cut-off of the amplification factor, respectively (see Figure 3·1a). Using a first order approximation, they have the form

$$q_m^2 = -\frac{(M\hat{\chi}_{q=0}^{-1}(t) + L\kappa)}{2M\kappa} \quad \text{and} \quad q_-^2 = -\frac{(K + L\Delta\hat{T})}{M\Delta\hat{T} + L\kappa} \tag{3.4}$$

We note that the maximum of the amplification factor, $q_m = q_m(t)$ is time dependent, while we hypothesize that q_- is time independent. The time dependence of $q_m(t)$ is given through the higher order terms of the chemical potential, Eq. (3.2), and is introduced into the time-dependent inverse susceptibility, $\hat{\chi}_{q=0}^{-1}(t) = \partial\hat{\mu}/\partial\hat{c}_A(t)$. The origin of this temporal evolution is due to the change in concentration at constant temperature from the unstable ($\hat{c}_A = 0$) to the stable ($\hat{c}_A > 0$) regime; as such, in the second order approximation, $\hat{\chi}_{q=0}^{-1}(t) \simeq \Delta\hat{T} + (1 + \Delta\hat{T})\hat{c}_A^2(t)$ (Longo and Anisimov, 2021; Langer and Bar-on, 1973; Billotet and Binder, 1980). In contrast, q_- is an intrinsic property of the system, and since q_- determines the cut-off for the smallest possible growing domain modes, then the steady-state limit of the time evolution of the maximum wavenumber will also be cut-off by q_- as $q_m(t \to \infty) \propto q_-$. To verify this prediction, we numerically compute q_m from the wavenumber corresponding to the maximum of the structure factor, q_m^s, and compare our results with the steady-state domain modes obtained from simulations of a nonequilibrium hybrid model.

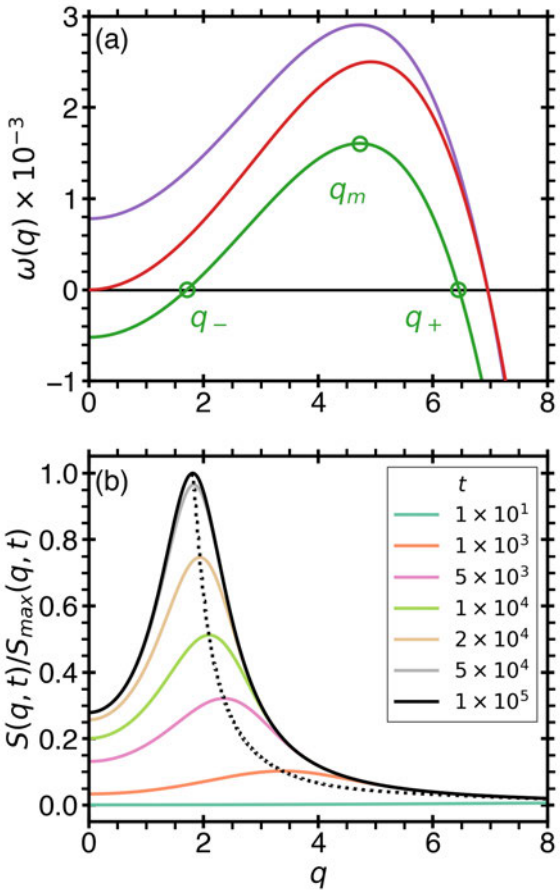

Figure 3·1: a) The amplification factor, $\omega(q)$, given by Eq. (3.3), for $\kappa = 1$ and $\Delta\hat{T} = -0.1$. The red curve represents the Cahn-Hilliard theory (phase separation) for $M = 1$, $L = 0$, $K = 0$; the purple curve represents phase amplification for $M = 1$, $L = 1/127$, and $K = 0$; the green curve represents the generalized Cahn-Hilliard theory in the presence of natural and forceful interconversion for $M = 1$, $L = 1/127$, $K = 1.3 \times 10^{-3}$. For the latter case (with forceful interconversion), the green circles indicate the three characteristic wavenumbers of the amplification factor: the maximum, q_m, the lower cut-off, q_-, and the upper cut-off, q_+. b) The time evolution of the structure factor, given by Eq. (3.9), for the same parameters used in the generalized Cahn-Hilliard-Cook theory in the presence of natural and forceful interconversion. The black dotted line depicts the evolution of the maximum of the structure factor. Due to the external source of forceful interconversion, the maximum of the structure factor is interrupted at the wavenumber q_-, while for complete phase separation and phase amplification, the maximum of the structure factor will evolve to $q = 0$ for an infinite-sized system.

3.2.2 Structure Factor Modified by Interconversion of Species

Defining the order parameter fluctuation variable as $\delta\hat{c}(\vec{r},t)$, the structure factor is given through the correlation function for the concentration fluctuations (Bray, 2002); such that

$$S(q,t) = \int \mathrm{d}\vec{r} < \delta\hat{c}(\vec{r},t)\delta\hat{c}(\vec{r}_0,t) > e^{i\vec{q}\cdot\vec{r}} \tag{3.5}$$

As shown by Cook (Cook, 1970) and Langer *et al.* (Langer et al., 1975), the equation of motion for $S(q,t)$ is found by introducing order-parameter fluctuations into the time evolution of the order parameter, Eq. (3.1), with $\delta\hat{c}(\vec{r})$ as the fluctuation variable and spatially integrating $\langle|\delta\hat{c}|^2\rangle$. Following this procedure, we obtain the first-order solution for mixed diffusion-interconversion dynamics as

$$\frac{\partial S(q,t)}{\partial t} = 2\omega(q,t)S(q,t) + 2\left(Mq^2 + L\kappa\right) \tag{3.6}$$

where $\omega(q,t)$ is given by Eq. (3.3) (Glotzer and Coniglio, 1994; Coniglio and Zannetti, 1989; Coniglio and Zannetti, 1990). We note that in the absence of interconversion and forceful racemization, this equation reduces to the result presented by Cook (Cook, 1970). Solving this differential equation for the structure factor, assuming a linear approximation (Langer and Bar-on, 1973), $\partial\omega/\partial t \ll \omega(q,t)$, gives (Billotet and Binder, 1980; Binder et al., 1978; Binder, 1983; Strobl, 1985)

$$S(q,t) = S_\infty(q) + \left[S(q,t=0) - S_\infty(q)\right] e^{2\omega(q,t)t} \tag{3.7}$$

where $S(q,t)$ represents the modified Cahn-Hilliard-Cook structure factor, which now includes natural and forceful interconversion. In the limit of infinite time, when $\partial S(q,t)/\partial t = 0$, the steady-state structure factor, $S_\infty(q)$, is given by

$$S(q,t\to\infty) = S_\infty(q) = \frac{Mq^2 + L\kappa}{-\omega(q,t\to\infty)} \tag{3.8}$$

It can be seen that when either $L = 0$ or $M = 0$, then this equation in equilibrium conditions ($K = 0$) reduces to the Ornstein-Zernike structure factor - $S_{OZ} = \xi^2/(1 + \xi^2 q^2)$, where the correlation length of concentration fluctuations is $\xi^2 = -\kappa/\Delta\hat{T}$.

The time-dependent structure factor, Eq. (3.7), can be simplified by applying the condition that at $t = 0$, the system is quenched from a sufficiently high temperature where $S(q, t = 0) = 0$. Therefore, Eq. (3.7) may be written as

$$S(q,t) = S_\infty(q)\left(1 - e^{2\omega(q,t)t}\right) \tag{3.9}$$

which is valid from the initial stages of spinodal decomposition to the coarsening regime (Binder, 1983; Cahn, 1966). Evaluating $\partial S_\infty/\partial q = 0$ to determine the wavenumber corresponding to the maximum of the structure factor gives $q_m^s = 2^{1/4} q_-$ in the steady-state limit. The time evolution of the structure factor is illustrated in Figure 3·1b. To account for the time dependence of $q_m(t)$, we assume a simple approximation of the transition in the form $q_m(t) = q_m(t = 0)\exp(-t/\tau) + q_-(1 - \exp(-t/\tau))$ based on the limiting values of q_m at $t = 0$ and $t \to \infty$, where $\tau = 100$, is a system dependent parameter that controls the crossover from spinodal decomposition to the coarsening regime. As shown in Figure 3·1, the wavenumber corresponding to the maximum of the steady-state structure factor, q_m^s, aligns with the prediction of q_- from the theory. To accurately match the predictions from the theory with the computational results presented in the following section, we scale the characteristic wavenumbers from the theory by the size of the system.

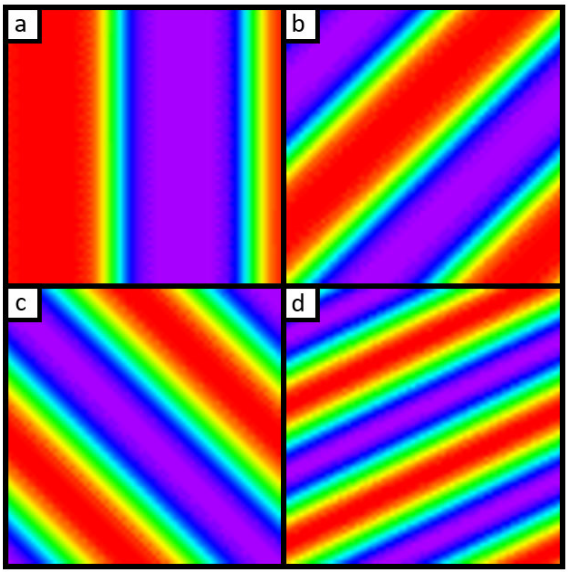

Figure 3·2: Steady-state phase domain morphology for different magnitudes of forceful interconversion (after $\sim 10^5$ time steps) computed from the time evolution of the order parameter, Eq. (3.1), with $M = 1$, $L = 1/127$, $\Delta\hat{T} = -0.1$, $\ell = 64$, $\sigma_i = 0.1$, $\eta = 10^{-5}$. Morphologies are shown for the middle slice of the three-dimensional system at (a) $K = 0$, (b) $K = 5 \times 10^{-4}$, (c) $K = 15 \times 10^{-4}$, and (d) $K = 25 \times 10^{-4}$. The red regions correspond to where the value of the normalized order parameter is $\hat{c}_A/\hat{c}_A^{\max} = 1$, the purple regions correspond to where the value of the normalized order parameter is $\hat{c}_A/\hat{c}_A^{\min} = -1$, and the other colors depict the interface between these two regions. The image in (a) depicts a metastable structure toward phase amplification (Shumovskyi et al., 2021), while the images in (b-d) are modulated steady-state structures with a characterize size, $1/q_-$.

3.3 Methods

3.3.1 Spatial and Temporal Evolution of the Order Parameter

Using the finite difference method (Press et al., 2007), with a spatial step $\Delta x = 1$ and a time step $\Delta t = 0.015$, we calculate the temporal evolution of the order parameter given by Eq. (3.1) with a chemical potential given by Eq. (3.2). We observed that for time steps $\Delta t > 0.015$, the solution diverges (Press et al., 2007). We include a random force term, η, to account for the thermal motion of the particles (Cook, 1970; Binder, 1983). The system is initialized on an $\ell \times \ell \times \ell$ cubic lattice with positions varied with initial random, Gaussian noise, σ_i. The structure factor is calculated via a Fast Fourier Transform (FFT) of the order parameter throughout the system (Press et al., 2007).

3.3.2 Nonequilibrium Ising/Lattice-Gas Hybrid Model

We consider an "Ising-like" lattice model where diffusion is modeled by "swapping" the position of two neighboring species and interconversion is modeled by "flipping" one species type to another (Shumovskyi et al., 2021). The diffusion and interconversion dynamics are simulated using a hybrid of Kawasaki and Glauber Monte Carlo (MC) methods (Bray, 2002; Kawasaki, 1966; Glauber, 1963), respectively. The species are arranged on an $\ell \times \ell \times \ell$ cubic lattice with a coordination number of 6. Using the Ising model Hamiltonian (Huang, 1987b)

$$H = -\frac{\varepsilon}{2} \sum_{i=1}^{\ell^3} \sum_{j \in \Omega(i)} s_i s_j \tag{3.10}$$

where s_i, $s_j = \pm 1$ are spins, $\Omega(i)$ is the set of 6 nearest neighbors of spin i, and ϵ is the interaction energy. The critical temperature of this system is $T_\mathrm{c} = 4.5115(1)\epsilon/k_\mathrm{B}$ (Heuer, 1993a). Realizations are initialized with a random spin configuration in which $\ell^3/2$ are positive and the other $\ell^3/2$ are negative. In addition, we assume that

at each MC step the probability of a random spin flip (a Glauber step) is p_r, while the probability of swapping a randomly selected pair of nearest neighbor spins (a Kawasaki step) is $1 - p_r$.

The equilibrium formulation, detailed in Ref. (Shumovskyi et al., 2021), is converted to nonequilibrium via the introduction of an additional energy, E, incorporated into the Boltzmann factor for the probability that a spin flip will be accepted as $p \sim \exp\left[-(\Delta U - E)/k_{\mathrm{B}}T\right]$, in which ΔU is the difference in internal energy of the system for this step (Metropolis and Ashenhurst, 1963). Thus, the effect of the energy source only affects the interconversion dynamics of the system. The diffusion dynamics, determined in each Kawasaki step, occur with a probability that two spins will swap according to the Metropolis criterion without any additional energy source. We introduce a size-independent MC time as $t = n/\ell^3$, such that in every time unit, each spin in the system has a chance, p_r, to flip, or a chance, $1 - p_r$, to swap with a neighboring spin. The probability of spin flipping is related to the diffusion and interconversion kinetic coefficients, M and L respectively, through $p_r = L/(M + L)$ (Shumovskyi et al., 2021). Additionally, the frequency of spin flipping is absorbed into the time step, δt, so that the kinetic coefficients, and consequently p_r, do not depend on temperature.

The dynamic structure factor is calculated using the method described in Kumar *et al.* (Kumar et al., 2005). This method differed from the FFT method, used in Sec. 3.2, since the maximum of the structure factor (after normalizing by ℓ^3) differed by a factor of π. Additionally, using the FFT method, the time evolution of the structure factor was interrupted at the wavenumber $q = 1$ (indicating that the size of the two phase domains were half the size of the simulation box, $\ell/2$), while using the method presented in Kumar *et al.*, the maximum of the structure factor was interrupted at a larger wavenumber. To correct for this difference, we scale the wavenumbers such

that complete phase separation occurs at $q = 1$.

3.4 Results and Discussion

We confirmed that the presence of a source of forceful interconversion causes the system to phase separate into steady-state microphase domains as presented in Figures 3·2(a-d). Due to the periodic boundary conditions imposed in the continuum finite-difference method used to compute Eq. (3.1), we found that the stripe morphologies will form at any angle with respect to the simulation box. The characteristic size of the stripe-like domains decreases with increasing forceful interconversion source strength, K. We note that a condition for microphase separation is that K must be sufficiently "strong" as to overcome the natural interconversion. If the magnitude of K is not strong enough, then (depending on the rate of natural interconversion) the system will either undergo phase amplification or complete phase separation. For instance, for $M = 1$, $L = 1/127$, $\Delta\hat{T} = -0.1$, and $K \leq 4 \times 10^{-4}$, then microphase separation is not observed. Since $L = 1/127$, the interconversion rate is relatively slow, and thus, the system has a higher probability of forming an interface between phases as shown in Figure 3·2a. However, for a system with natural interconversion this state is metastable, and eventually, the interface between phases will break down and phase amplification will occur (Shumovskyi et al., 2021).

The time-dependent structure factors, which produce the stripe-like morphology, as illustrated in Figures 3·2(a-d), are presented in Figures 3·3(a-d). We observe that the time evolution of the maximum of the structure factor in Figure 3·3a is interrupted at the wavenumber $q = 0$, which corresponds to a system undergoing phase amplification. For $K = 4 \times 10^{-4}$ (Figure 3·3b), the maximum of the time evolution of the structure factor is interrupted at $q = 1$, indicating complete phase separation where the phase domains have a characteristic size of half the simulation box, $\ell/2$. In

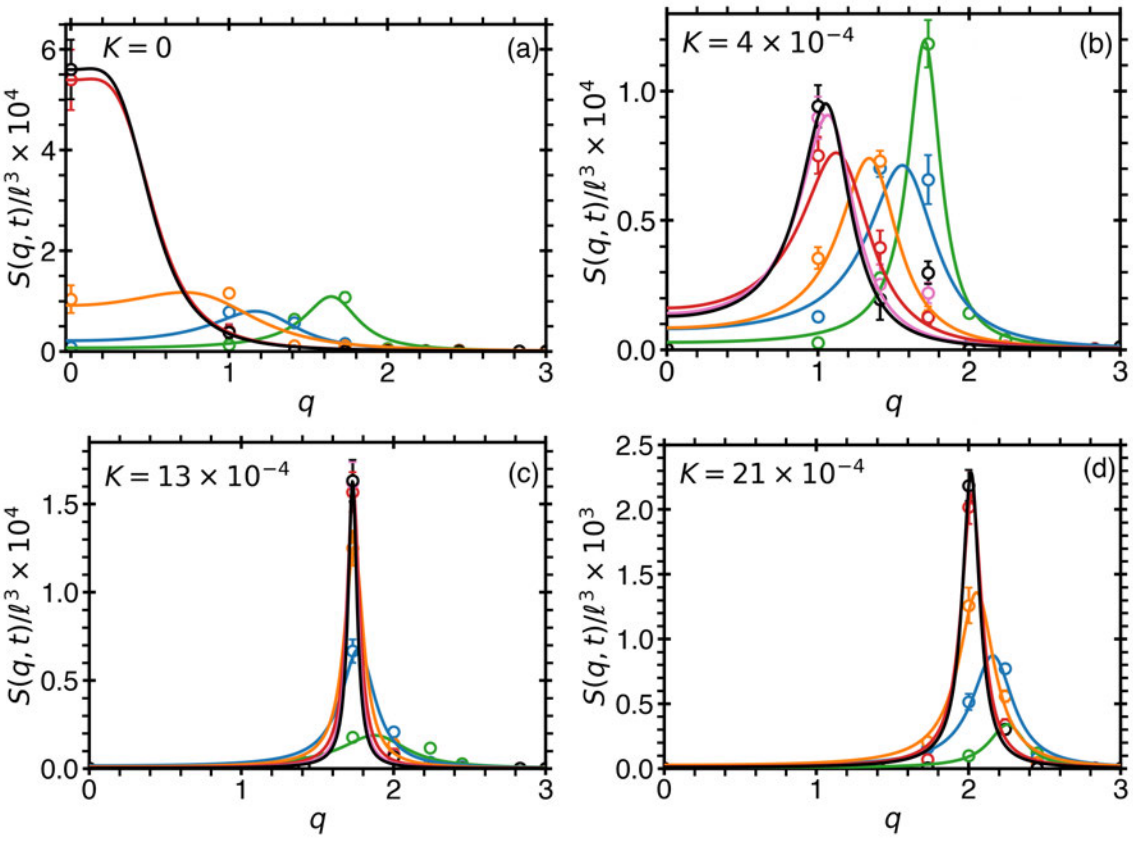

Figure 3·3: Time evolution of the structure factor computed from the Fast Fourier transform (FFT) of Eq. (3.1) for $M = 1$, $L = 1/127$, $\Delta\hat{T} = -0.1$, $\ell = 64$, $\sigma_i = 0.1$, $\eta = 10^{-5}$ depicted at times $t = 6 \times 10^3$ (green), $t = 1.2 \times 10^4$ (blue), $t = 2.4 \times 10^4$ (orange), $t = 5 \times 10^4$ (red), $t = 1 \times 10^5$ (pink), and $t = 2 \times 10^5$ (black). The open circles in (a-d) depict the computed structure factors for the four selected magnitudes of forceful interconversion averaged over $N = 100$ realizations with 95% confidence interval error bars, while the solid lines illustrate the behavior of the structure factors assuming a Gaussian distribution. In (a), the evolution of the maximum of the structure factor is interrupted at the wavenumber $q = 0$, corresponding to phase amplification, while in (b) the maximum is interrupted at $q = 1$, corresponding to phase domains with a characteristic size of half the simulation box, $\ell/2$. In (c,d), the evolution of the maximum of the structure factor is interrupted at wavenumbers $q = q_- > 1$ corresponding to microphase separation.

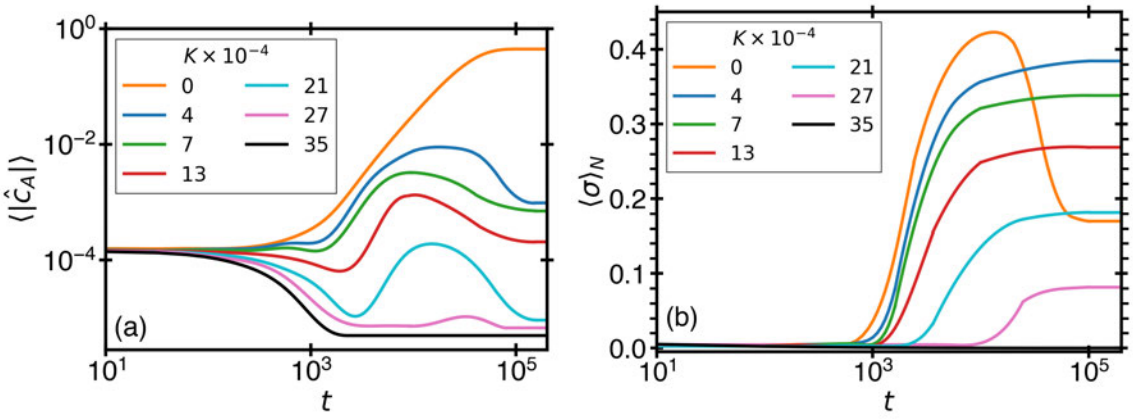

Figure 3·4: The temporal evolution of the symmetry of phase separation. a) The time evolution of the average order parameter, calculated by first averaging over all space and second by averaging the absolute value over $N = 100$ realizations, for $M = 1$, $L = 1/127$, $\Delta T = -0.1$, $\sigma_i = 0.1$, $\eta = 1.0 \times 10^{-5}$, and various magnitudes of forceful interconversion, K. b) The time evolution of the N-averaged standard deviation of the averaged order parameter, calculated by first determining the standard deviation of the spatially averaged order parameter and second by averaging over $N = 100$ realizations. This method of averaging highlights the behavioral deviation from an equal concentration of species A and B, $\hat{c}_A = 0$.

Figures 3·3(c,d), the time evolution of the maximum of the structure factor is interrupted at higher wavenumbers depending on K. These wavenumbers correspond to the characteristic size of the stripe-like phase domains and are independent of the size of the system. We also observe that the structure factor at the maximum wavenumber (q_m) contains the largest uncertainty, with respect to the other wavenumbers. The non-monotonic temporal evolution of the structure factor observed in Figures 3·3b can be attributed to $\tau \approx 1.5 \times 10^3$, a large characteristic crossover time scale between spinodal decomposition and coarsening. This observation suggests that the crossover time scale, $\tau = \tau(K)$, may depend on forceful interconversion.

The temporal evolution of the order parameter was calculated from Eq. (3.1) using the chemical potential given in Eq. (3.2). The average value of the order parameter, calculated by first averaging over all space and second averaging the absolute value over $N = 100$ realizations, is presented in Figure 3·4a. This method of averaging

highlights the behavioral deviation from $\hat{c}_A = 0$, when the concentration of species A is equivalent to species B; therefore, this figure represents the temporal evolution of the symmetry of phase separation. We observed that the initial value $\langle|\hat{c}_A|\rangle$ is determined by σ_i, the random initial configuration, whereas the steady-state behavior of $\langle|\hat{c}_A|\rangle$ is determined by η, the thermal noise to be included in Eq. (3.1). We find that $\langle|\hat{c}_A|\rangle$ develops a peak during the formation of the stripe-like patterns. As the phase domains coarsen, the averaged order parameter reaches a steady-state value, $\langle|\hat{c}_A(t \to \infty)|\rangle = c_0$ indicating the stable formation of the stripe-like domains.

In Figure 3·4b, we show the temporal evolution of the standard deviation of the averaged order parameter, calculated by first determining the standard deviation over all space and second by averaging over $N = 100$ realizations. We observed that the N-averaged standard deviation, $\langle\sigma\rangle_N$, was constant through the early stages of spinodal decomposition, but dramatically increased during the formation of the stripe-like patterns. We note that in the $K = 0$ case due to phase amplification $\langle\sigma\rangle_N$ rapidly increases as the domains coarsen, but then decreases when one phase grows at the expense of the other. In this case, the constant steady-state limit of the averaged standard deviation, $\langle\sigma(t \to \infty)\rangle_N = \sigma_0$, indicates that the order parameter has reached its equilibrium value, $|\hat{c}_A| = c_0$, which depends on the distance to the critical temperature.

In Figures 3·5(a,b), we compare the structure factor theory with simulations of the nonequilibrium hybrid model (defined in Sec. 3.2). In Figure 3·5a, we show the steady-state structure factor from simulations at three different additional energy values, E, at constant temperature, $\Delta\hat{T} = -0.4$, averaged over $N = 60$ realizations. Unlike the morphologies computed from Eq. (3.1) via the finite-difference method, the snapshots of the MC simulations shown in the insets of Figure 3·5a depict stripe-like phase domains that form along the diagonal of the simulation box. We attribute

this affect to the lattice structure utilized in the MC simulations. We introduce three system-dependent constants into the steady-state structure factor (when $q_m \sim q_-$) and use Eq. (3.8) in the form

$$S_\infty(q) = \frac{S_0 a^2 (q^2 + L_{\text{eff}})}{a^2 q_-^4 + [q^2 - (1+a)q_-^2]^2} \tag{3.11}$$

where the amplitude ratio relating the theory to the nonequilibrium hybrid model is $S_0 = 46.5$ and the effective interconversion kinetic coefficient is $L_{\text{eff}} \sim L/M = 0.0012$. The constant $a = 0.2$, which describes the relationship between $q_m(t \to \infty)$ and q_-, broadens or sharpens the scattering peak. At the maximum of the structure factor, when $q = q_-$, then Eq. (3.11) reduces to $S_\infty(q_-) = S_0/(2q_-^2)$, which is independent of a. We note that in this form, Eq. (3.11) resembles the scattering intensity distribution of microemulsions (Teubner and Strey, 1987).

In Figure 3·5b, the dependence of the wavenumber corresponding to the maximum of the structure factor, q_m^s, on the magnitude of forceful interconversion, K is illustrated for the theoretical prediction (curves), computations of the time evolution of the order parameter (circles), and simulations of the nonequilibrium hybrid model (triangles). The curves are determined from the full expression for the lower cut-off wavenumber, q_-, found from Eq. (3.3), when $\omega(q, 0) = 0$. A variable amplitude and shift are introduced to scale the theoretical prediction of q_- such that microphase separation begins at $q = 1$. An additional system dependent constant is introduced to describe the relationship between $q_m(t \to \infty)$ and q_-. The numerical computations of q_m^s (averaged over $N = 100$ realizations) from the time evolution of the order parameter, Eq. (3.1), are shown in the steady-state regime (after $t \sim 10^5$ time steps). The magnitude of forceful interconversion, K, (for different external energies, E) was obtained for the nonequilibrium hybrid model using Eq. (3.11). In the insert of Figure 3·5b, we illustrate the relationship between theory and the nonequilibrium hybrid

model, as $K \propto E^2$.

In addition, as illustrated by Figure 3·5b, we find two values of forceful interconversion, K^* and K^{**} (indicated by the vertical lines), that bound the formation of microphase domains. Both boundaries increase with $\Delta\hat{T}$; such that, for $\Delta\hat{T} > -0.1$, K^{**} is located off the scale of the figure. For $K < K^*$ phase amplification was observed, while for $K > K^{**}$, no striped patterns were observed; instead, only a homogeneous solution persisted, in which an apparent structure on a small scale may be attributed to the correlations between concentration fluctuations. In this case, the particles are forced to interconvert so rapidly that diffusion is impossible. As shown in Figure 3·5b, the lower bound, K^*, is associated with the characteristic wavenumber, $q^* = q = 1$, which corresponds to phase domains that form at half the size of the simulation box, $\ell/2$. In contrast, the characteristic wavenumber associated with the upper bound, q^{**}, is strongly dependent on temperature (Uralcan et al., 2021; Longo and Anisimov, 2021).

We note that for $\Delta\hat{T} = -0.1$, no structured microphase separation was observed in the nonequilibrium hybrid model. We attribute the lack of structured domains to the increase in concentration fluctuations facilitated by the close proximity to the critical point. This effect was not observed in the time evolution of the order parameter, shown in Figure 3·2(a-d), as the mean-field theory described in Sec. 2. is only applicable sufficiently far away from the critical point.

Lastly, as shown in Sec. 2, the wavenumber corresponding to the maximum of the structure factor, q_m^s, scales linearly with the lower cut-off wavenumber, q_-. Consequently, we observe the scaling law that $q_m^s \sim \sqrt{K} \propto \sqrt{f(T)}E$, where the temperature dependent prefactor is $f(T) \simeq 9.71T/(T_c - T)$. This result, which verifies our initial hypothesis, has also been confirmed in studies of a chiral model where the source of forceful interconversion is established internally via dissipative intermolec-

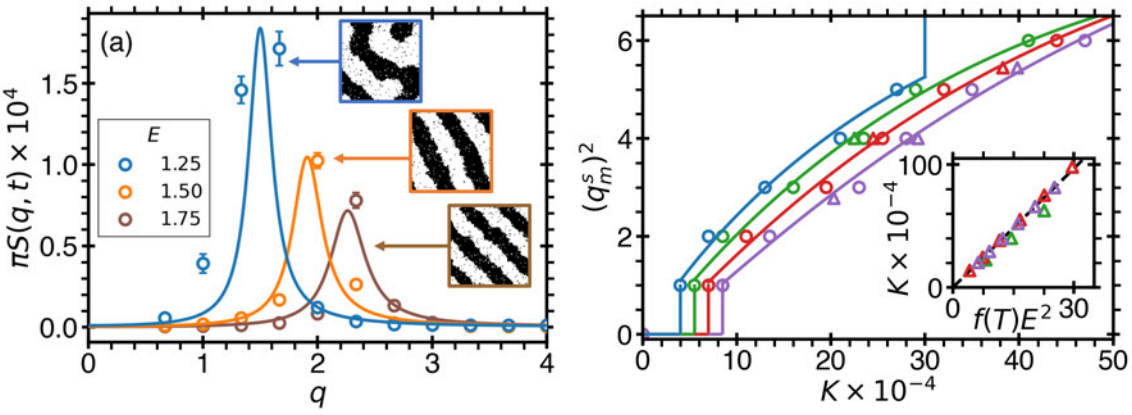

Figure 3·5: a) Steady-state structure factors computed for the nonequilibrium hybrid model (open circles) and the prediction given by Eq. (3.11) (solid lines) for selected external energy sources (E) at $\Delta\hat{T} = -0.4$, $M = 1$, $L = 1/127$, $\ell = 100$, and averaged over $N = 60$ realizations with 95% confidence interval error bars. The insets show steady-state ($t \sim 3 \times 10^5$) domain morphologies observed in the nonequilibrium hybrid model for the selected energies. b) The dependence of forceful interconversion on the wavenumber corresponding to the maximum of the structure factor, q_m^s, in the steady-state limit. The open circles are numerical computations of structure factors determined from FFTs of the time evolution of the order parameter, given by Eq. (3.1), in the steady-state limit ($t \sim 10^5$) for $M = 1$, $L = 1/127$, $\sigma_i = 0.1$, and $\eta = 10^{-5}$, averaged over $N = 100$ realizations. The triangles correspond to the predictions of K determined from fits of Eq. (3.11) to the structure factor for the nonequilibrium hybrid model, like those presented in (a). The curves illustrate the theoretical prediction $q_m(t \to \infty) \propto q_-$, given by the full expression for q_-, found from evaluating $\omega(q, 0) = 0$ using Eq. (3.3). The colors correspond to temperatures: $\Delta\hat{T} = -0.1$ (blue), $\Delta\hat{T} = -0.2$ (green), $\Delta\hat{T} = -0.3$ (red), and $\Delta\hat{T} = -0.4$ (purple). The inset shows the relationship between K and E.

ular forces (Uralcan et al., 2021). Interestingly, previous studies of phase separating block copolymers in the presence of forceful interconversion found that $q_m^s \sim K^{1/4}$ (Christensen et al., 1996; Glotzer and Coniglio, 1994). As these previous studies considered an n-component order parameter to describe the block copolymer system (whereas, in this work, we describe our binary mixture via a single-component order parameter), this implies that the effect of K on q_m^s is system dependent and could depend on the nature of the order parameter.

3.5 Conclusion

We have demonstrated that the presence of a source of forceful interconversion in a hybrid binary system that possess both diffusion and natural interconversion dynamics may produce microphase separation. We characterize the time evolution of the phase formation through two characteristic wavenumbers, q_m and q_-, which correspond to the maximum and lower cut-off wavenumbers of the amplification factor obtained from the generalized theory of spinodal decomposition. In the infinite time (steady-state) limit, we showed that $q_m(t \to \infty) \propto q_- \propto K^{1/2}$, where K is the rate of forceful interconversion. We compared the structure-factor theory with Monte Carlo simulations of a nonequilibrium hybrid model and demonstrated that the origin of microphase separation may be related to an external energy source, as $E \propto K^{1/2}$, which allows domain formation to be more energetically favorable.

Our symmetric binary mixture with molecular interconversion of species represents the simplest case of liquid polyamorphism – the possibility of liquid-liquid transition in a single-component substance. Indeed, the interconversion of species allows the concentration to be a thermodynamically dependent property, equivalent to the reaction coordinate. Therefore, the system, in terms of its thermodynamic degrees of freedom, behaves like a single-component substance (Anisimov et al., 2018a). Thus,

in our simple system, as in the Ising model, the equilibrium value of the reaction coordinate is always 50% above the critical temperature and contains two equilibrium values, corresponding to the coexisting liquid phases, below the critical temperature. Another simple system exhibiting liquid polyamorphism is a mixture of interconverting enantiomers (Uralcan et al., 2021). In this system, the equilibrium interconversion fraction does not depend on temperature and pressure, like in our model. In the future, our approach could be generalized to more complex systems exhibiting or suggesting liquid polyamorphism, such as supercooled water (Gallo et al., 2016b), where the fraction of interconversion of alternative molecular of supramolecular states is usually a function of temperature and pressure (Anisimov et al., 2018a; Longo and Anisimov, 2021).

Another possible application of our approach could be glassy polyamorphism, a largely unexplored area. It is commonly believed that the hypothesized liquid polyamorphism in supercooled water, which is possibly caused by the interconversion of alternative supramolecular structures, is related to the experimentally established existence of two glassy waters, high-density glass and low-density glass (Gallo et al., 2016b; Giovambattista et al., 2012; Amann-Winkel et al., 2013; Loerting et al., 2015). In this respect, it would be interesting to consider effects of structural interconversion in glassy systems. In addition, forceful interconversion, as a result of an external source of energy, may generate nonequilibrium microphase separation in glasses, similar to that studied in this work. These structures could be similar to the nonequilibrium nano-scale phase separation formed by "frozen" spinodal decomposition, as observed in metallic glasses (Kim et al., 2013). This is another unexplored area of research.

Chapter 4

Generic Maximum Valence Model

In this section, motivated by the recent discoveries of the LLPT in hydrogen (Dalladay-Simpson et al., 2016b) and in sulfur (Henry et al., 2020), we propose a simple generic model to describe liquid polyamorphism in a variety of chemically-reacting fluids. The model combines the ideas of two-state thermodynamics (Anisimov et al., 2018b; Holten et al., 2014) with the maximum-valence approach (Zaccarelli et al., 2005; Speedy and Debenedetti, 1994; Speedy and Debenedetti, 1996), in which atoms may form covalent bonds via a reversible reaction, changing their state according to their bond number. By mimicking the valence structure by maximum bond number, z, our model predicts the LLPT in systems with dimerization ($z = 1$), polymerization ($z = 2$), and gelation ($z > 2$). We show that when the atoms with maximal valence repel atoms with any valence, phase separation is coupled to dimerization ($z = 1$), polymerization ($z = 2$), and gelation ($z > 2$), thus generating the LLPT in polyamorphic substances.

4.1 Maximum-Valence Model

We model LLPT induced by molecular interconversion in polyamorphic substances by characterizing each atom by its coordination number $k \leq z$, the number of bonds it has with other atoms. Depending on the coordination number, each atom is assigned to distinguished $z + 1$ states: B_0 (with zero bonds), B_1 (with one bond), B_k (with k bonds), and finally B_z (with z bonds). Atoms cannot form more than z bonds

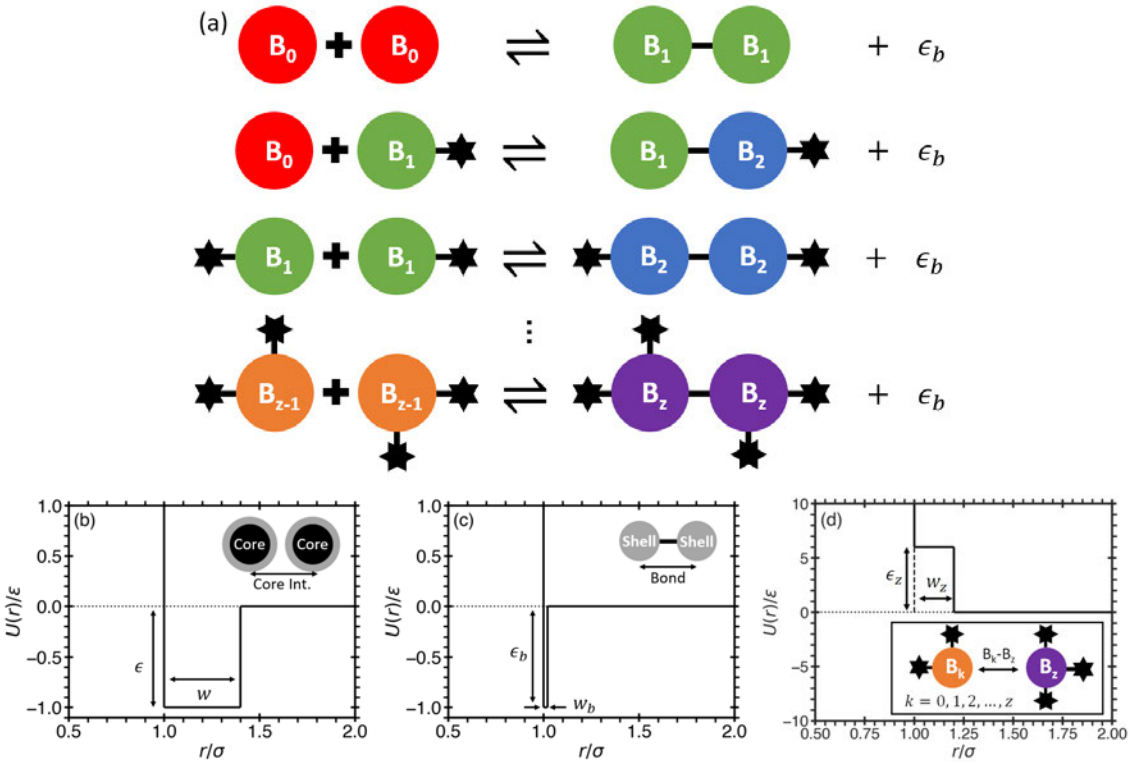

Figure 4·1: Reactions and interactions in the generic maximum-valence model with repulsion. (a) $z(z+1)/2$ types of covalent bond-forming reversible chemical reactions that may occur in the system. If two atoms without bonds (B_0) collide with each other, they may form a bond and become B_1 atoms. If a B_0 and B_1 atom collide, they may form a bond and become B_1 and B_2 atoms, respectively. If two B_1 atoms collide with each other, they form an additional bond and become B_2 atoms. This continues until the atoms reach their maximum valency - state B_z. (b-d) The three major interactions between atoms, in which each atom is composed of a core and shell, both with a diameter σ and mass m. $U(r)$ is the pair potential energy and r is the distance from the centers of the particles. (b) The cores of each atom interact with an attractive square well of depth ϵ and width w. (c) The shells may react to form covalent bonds that consist of a narrow well with depth ϵ_b and width w_b. (d) Phase segregation is coupled to dimerization, polymerization, gelation, etc., via the additional repulsive interactions between atoms in state B_z and atoms in a state B_k with $k \leq z$, described by a square shoulder of height $-\epsilon_z$ and width w_z.

and, consequently, will associated into either dimers, for $z = 1$, or linear polymers, $z = 2$, or some network structure $z > 2$. All of the atoms in the system may change their state by forming or breaking a covalent bond via a reversible reaction. Fig. 4·1a depicts all $z(z+1)/2$ types of reversible reactions that may occur in the system. In this work, we demonstrate that the minimum ingredients required to produce a LLPT are the following: i) the van der Waals interactions between atoms, which produce a LGPT; ii) covalent bonds between atoms, which induce association; and iii), as we hypothesize, additional repulsive interactions between atoms with maximum valence ($k = z$) and atoms with any valence ($k \leq z$), that are needed to couple phase segregation to dimerization, polymerization or gelation. These three ingredients are illustrated by square-well potentials in Fig. 4·1(b-d).

In case of hydrogen, the additional repulsive interactions between bonded atoms and non-bonded atoms mimic the fact that the atoms in the molecules H_2 have a larger repulsive diameter than atoms in metallic state which lacks bonded electrons.

To verify our hypothesis, we implement these three ingredients of interactions via an event-driven MD technique (Alder and Wainwright, 1959; Rapaport, 2004); in particular, we use a discrete MD package (DMD) that only includes particles interacting through spherically-symmetric step-wise potentials, which may form bonds via reversible reactions (Buldyrev, 2009). We simulate an NVT ensemble of $N = 1000$ atoms in a cubic box with periodic boundaries at various constant densities and temperatures. The temperature is controlled by a Berendsen thermostat (Berendsen et al., 1984). The van der Waals and covalent-bonding interactions are implemented by separating each atom into two overlapping hard spheres (a core and a shell), with the same diameter σ and mass m, see Fig. 4·1(b-d). The connection between the core and its shell is represented by an infinite square-well potential of width $d \ll \sigma$. The cores and shells of different atoms do not interact with each other. The core

represents the atom without its valence electrons. It interacts with other cores via a wide potential well with depth ϵ and width $w \sim \sigma$. We use σ, m, and ϵ as units of length, mass, and energy, respectively, and measure all other physical quantities using combination of these units. For example, temperature T is measured in units of ϵ/k_B; pressure, P is measured in units of ϵ/σ^3; and time t is measured in units of $\sigma\sqrt{m/\epsilon}$. We note that all physical parameters reported below are normalized by the appropriate combination of mass m, length σ, and energy ϵ units, as used in (Fried et al., 2022). Meanwhile, the shell represents the outer valence electron cloud. It can form bonds with other shells via a narrow potential well with depth $\epsilon_b = \epsilon$ and width w_b (Fig. 4·1c), which models the breaking and forming of covalent bonds. When the shell interactions are included and the system may form covalent bonds, the location of the LGCP changes, but not significantly. Also we introduce an additional repulsive potential well (with depth ϵ_z and width w_z, Fig. 4·1d) for the van der Waals interaction for the shells of the atoms with z bonds, which are not chemically bonded to each other. Here we assume that $\epsilon_z < 0$ means repulsion, while the $\epsilon_z > 0$ means attraction. We also emphasize the key difference between the case of repulsion in this work and attraction for the atoms of maximal valence model for sulfur(Shumovskyi et al., 2022). In case of attraction the shells in the state B_z attract each other, but do not interact with other shells other than by hard-core repulsion with diameter σ. Conversely, for the case of repulsion shells in the state B_z repel from each other and from all other shells, while other shells do not interact with each other except by forming and breaking bonds, with the condition that two non-bonded atoms with $k < z$ cannot be within distance from each other smaller than the bond length w_b. Technically, this is achieved by assigning to such a pair a very strong repulsive potential at distance w_b.

We note that during either the formation or breaking of a bond, the new state

of the reacting particles may modify the potential energy of their interactions with their non-bonded neighboring particles. In our model, this occurs when particles in the state B_k convert to the state B_{k-1} (or vice versa). To maintain the conservation of energy, we calculate the change of the total potential energy, ΔU, due to the change of the state of the reacting particles and subtract it from the kinetic energy of the reacting pair. As a consequence, the equations for computing the new velocities (Buldyrev, 2009) may not have real solutions. In this case, the bond will not form or break, and the reacting particles will conserve their states through an elastic collision.

The applicability of the maximum-valence model has been already tested for the case of sulfur ($z = 2$, $\epsilon_z > 0$)(Shumovskyi et al., 2022). Here we will focus on an arbitrary value of z and additional repulsive interactions $\epsilon_z < 0$. Note that for the case of attraction ($\epsilon_z > 0$) the high density phase is polymerized. In the case of repulsion $\epsilon_z < 0$, the low density phase is dimerized, polymerized or forms network with coordination number z. By tuning z, the phase behavior of a variety of substances can be described. For instance, for $z = 1$, dimerization-induced phase separation (such as in high-pressure hydrogen (Morales et al., 2010; Zaghoo et al., 2016; Dalladay-Simpson et al., 2016b)) is investigated, while for $z > 2$, gelation-induced phase separation is investigated. In particular, the phase behavior of more complex chemically-reacting systems, such as phosphorous ($z = 3$) (Katayama et al., 2000; Katayama et al., 2004) and supercooled water, forming hydrogen instead of covalent bonds, ($z > 3$) (Gallo et al., 2016b; Eisenberg and Tobolsky, 1960; Speedy and Debenedet, 1994; Zaccarelli et al., 2005; Anisimov et al., 2018a; Brazhkin et al., 1999; Duška, 2020; Holten and Anisimov, 2012), can be investigated.

4.2 Dimerization (Z = 1)

We start with the simplest case of $z = 1$, i.e. dimerization. We are allowing our system to have only two types of atoms, B_0 and B_1, which interact and may react by the scheme described by Fig. 1 with the maximal valence $z = 1$. We found that in the case of repulsion between the atoms with the maximal valence, B_1, we see liquid-liquid phase transition produced by dimerization of atoms while reducing pressure. To mimic the behavior of the hydrogen we select the following set of parameters $w = 0.5$, $w_b = 0.1$, $\epsilon_b = 6$, $w_1 = 0.2$, $\epsilon_1 = -12$. The choice of a very large values of ϵ_b and ϵ_z, comparatively to ϵ of the van der Waals forces is motivated by the desire to make the temperature and pressure of the liquid gas critical point to be much smaller than the temperature and pressure of the liquid-liquid critical point. For the selected set of parameters, the LGCP is located at $T_c^{LG} = 0.91 \pm 0.02$, $P_c^{LG} = 0.030 \pm 0.002$, $\rho_c^{LG} = 0.225 \pm 0.005$. Fig. 4·2a shows the $P - T$ phase diagram for this set of parameters near the LLCP with the crossing of isochores at $T_c^{LL} = 2.12$, $P_c^{LL} = 8.1655$, $\rho_c^{LL} = 0.5775$, the liquid-liquid coexistence line shown with blue line ending in the LLCP marked with a red ellipse. Note, that at the vicinity of the critical point the slopes of the isochores becomes negative which means that there exists a region of density anomaly in which the density of liquid decreases upon cooling. Moreover, it may indicate that the critical point is located in the region of density anomaly which implies that the critical isochores and the liquid-liquid coexistence line have a negative slope. Fig. 4·2b shows the apparent van der Waals loops on the $P - \rho$ phase diagram, which correspond to the Liquid-liquid phase transition.

Another interesting feature of the model is found by looking at the temperature-density phase diagram, as well as the plot of temperature vs fraction of bonded atoms $\phi = N_1/N$, where N is the total number of atoms and N_1 is the number of atoms in state B_1. In these diagrams we used reduced variables $\phi_r = (\phi - \phi_c)/\phi_c$,

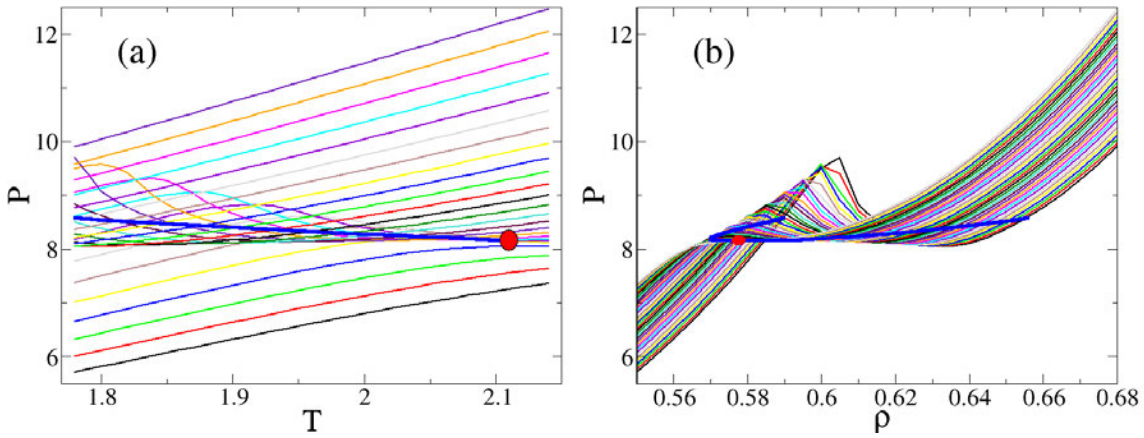

Figure 4·2: Phase diagrams for the maximum-valence model of dimerization, $z = 1$, ($w_b = 0.10$) obtained in an NVT ensemble after $t = 10^6$ time units. (a) The isochores in the $P-T$ plane withe $\rho = 0.550 - 0.680$ in steps $\Delta\rho = 0.005$. (b) The isotherms in the P-ρ plane with $T = 1.78 - 2.14$ in steps $\Delta T = 0.01$. In both figures, the liquid-liquid coexistence curves are calculated via the Maxwell construction and indicated by the blue curves. The liquid-liquid ($T_c^{LL} = 2.12$, $P_c^{LL} = 8.1655$, $\rho_c^{LL} = 0.5775$) critical points are indicated by the red circles.

$T_r = (T - T_c)/T_c$, and $\rho_r = (\rho - \rho_c)/\rho_c$ with $\rho_c = 0.5775$, $T_c = 2.12$, $\phi_c = 0.350$ for $w_b = 0.10$ and $\rho_c = 0.76$, $T_c = 2.14434$, $\phi_c = 0.578$ for $w_b = 0.06$. Fig. 4·3 shows that while the coexistence line on the T_r - ρ_r phase diagram is highly skewed to the right, the coexistence line on the T_r - ϕ_r phase diagram is quite symmetric, which resembles the actual distribution in liquid-liquid coexistence line in hydrogen (Fried et al., 2022). Note, that one might apply two-state thermodynamics approach and compare the exact solution for hydrogen with our results from the simulations. This comparison is one of our future works in progress which requires a thorough analysis of the hydrogen system.

Next, we studied the dependence of the phase diagram on the parameters: ϵ_1 and w_b, the strength of the additional interaction between the atoms in states with maximal valence, i.e. B_1 with z = 1, as well as the width of the bonds. As can be seen in the Fig. 4·4, upon increasing the strength ϵ_1 all the LLCP parameters decrease - critical temperature, critical pressure, as well as critical density. Physically

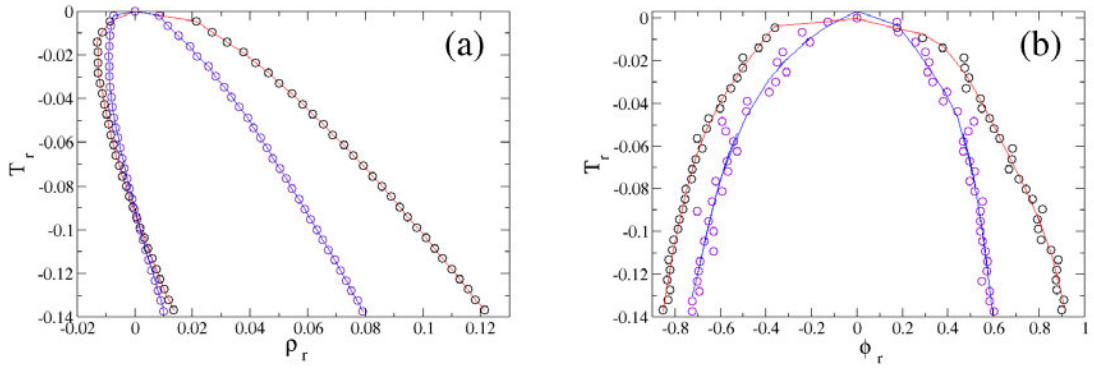

Figure 4·3: (a) T_r - ρ_r phase diagram for the maximum-valence model for dimerization, $z = 1$, (with $w_b = 0.10$, red, and $w_b = 0.06$, blue) obtained in an NVT ensemble after $t = 10^6$ time units. (b) The reduced temperature dependence of the reduced fraction of atoms with one bond, ϕ_r, in two coexisting liquid phases.

it means that upon increasing the repulsive energy between the bonded atoms, we effectively make the bonds less stable, and hence the temperature must be reduced to increase stability of the bonds necessary for the liquid-liquid phase segregation. As the repulsive energy between dimers increases the dimers get less penetrable and their density as well as the pressure required to create such a density drops. Thus we expect that both the density and the pressure of the second critical point decreases, as the repulsive energy increases. Fig. 4·4(d) shows that we can force our system to have a negative slope of a liquid-liquid coexistence line on a $P - T$ phase diagram by increasing $|\epsilon_1|$, which qualitatively reproduces the negative slope of a real hydrogen. Another important note is that upon increasing further the interaction energy between atoms with maximal valence, all four plots reach the plateau which corresponds to the limit $|\epsilon_1|/\epsilon_b \to \infty$, when the repulsion strength between B_1 atoms is much larger than bond strength and the system reaches the limit when the dimers become effectively impenetrable, so the system behaves like a system of quasi-hard spheres made of dimers which have larger effective radius rather than hydrogen monomers, and the LGCP parameters and the slope of the coexistence line rapidly acquire the values

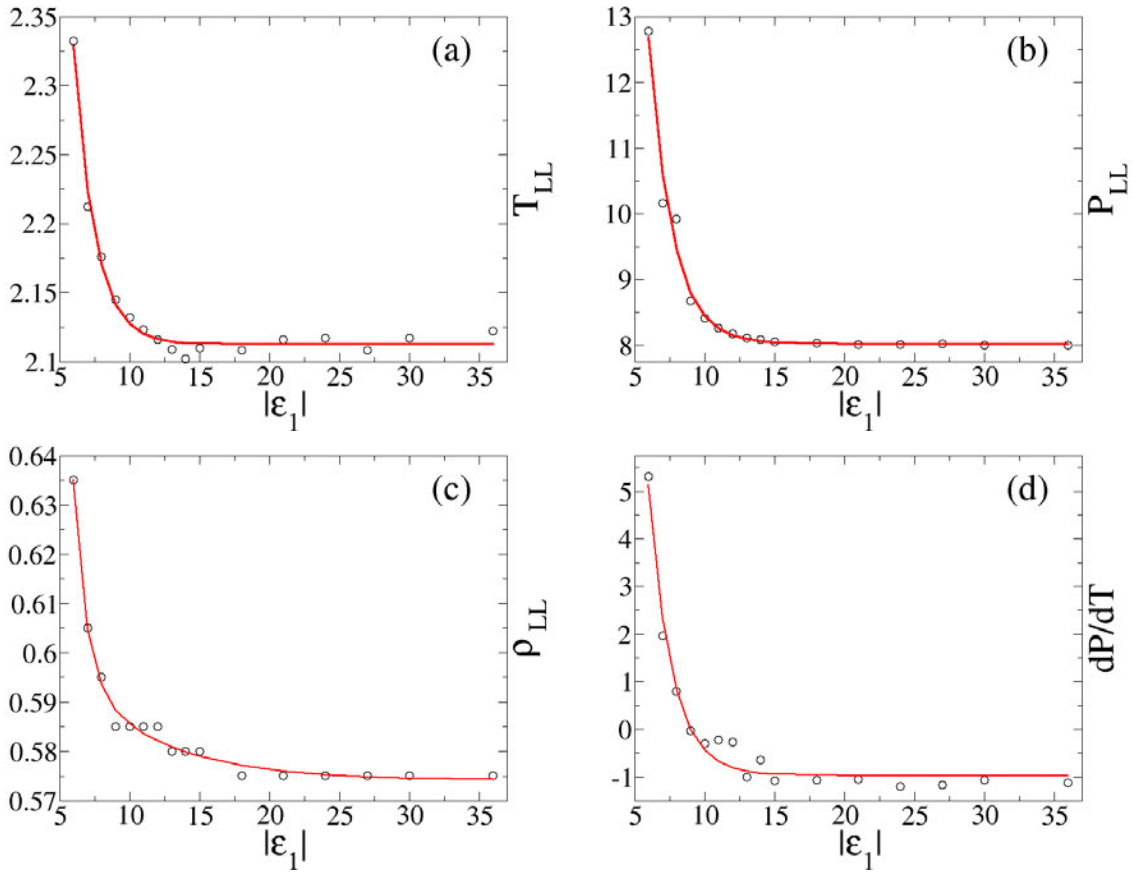

Figure 4·4: The dependence of the Liquid-liquid critical point parameters on the additional interaction strength $|\epsilon_1|$ for $z = 1$, $w = 0.5$, $d = 0.1$, $w_b = 0.1$, $w_1 = 0.2$, $\epsilon_b = 6$

corresponding to this limiting case, because the probability to find an atom sitting on repulsive shoulder decreases according to Arhenius law $\exp[\epsilon_1/(k_B T)]$. Indeed, all four parameters approach their limit exponentially with $\epsilon_1 \to -\infty$. The limit $\epsilon_1 \to -\infty$ corresponds to the impenetrable electron shells of the H_2 molecules, which cannot exist if another atom enters their electron shells and must break if such an event happens.

Fig. 4·5 shows the dependence of liquid-liquid critical pressure and critical density on the bond width at $\epsilon_b = 6$, $\epsilon_1 = -12$, keeping $w_1 = 2w_b$: as we increase the bond width, the system doesn't require that much pressure, or doesn't need to be in such a

squeezed state, for monomers to start dimerization, so the LLCP moves down in both P and ρ axis, however, the temperature of LLCP stays approximately the same, since the increase of the bond width only plays the entropic effect, not the energetic one. We note that upon decreasing the bond width further below $w = 0.06$, the LLCP becomes submerged below the crystallization line, and the phase transition is not observed anymore. However, increasing the bond width further will only decrease the (P_c, ρ_c) further, up to the point when liquid-liquid critical pressure becomes negative or LLCP is getting destroyed by LG spinodal. The phase diagrams corresponding to $w_b = 0.06$ are show in Fig. 4·6.

Note, that when we compare the $T - \rho$ phase diagrams, as well as the plots of $T - \phi$, for the two values of the bond width $w_b = 0.10$ and $w_b = 0.06$, we find that the the coexistence regions are indeed squeezed, when we reduce w_b from $w_b = 0.10$ to $w_b = 0.06$. The percentage difference of the densities of the HDL and LDL away from the critical point is about 11.5% for $w_b = 0.10$, while for $w_b = 0.06$ it is 6.9% (see Fig. 3). Note, that in hydrogen it is approximately 2% (Fried et al., 2022). In theory, upon decreasing the bond width we should obtain the desired 2%, however our simulations show that below $w_b = 0.06$ the LLCP is submerged below the crystallization line.

The same effect can be achieved by the reducing the width of repulsive interactions w_1, while keeping w_b constant. The differences in densities decreases when $(w_1 - w_b)/\sigma$ decreases, and reach 6% when $(w_1 - w_b)/\sigma = 0.06$, but further decrease leads to instantaneous crystallization in the region where the LLCP would be expected.

4.3 Polymerization (Z = 2)

In this section, motivated by the recent discoveries of the LLPT in sulfur (Henry et al., 2020) and hydrogen (Ohta et al., 2015; McWilliams et al., 2016; Dzyabura et al., 2013; Zaghoo et al., 2016; Zaghoo and Silvera, 2017), we propose a simple

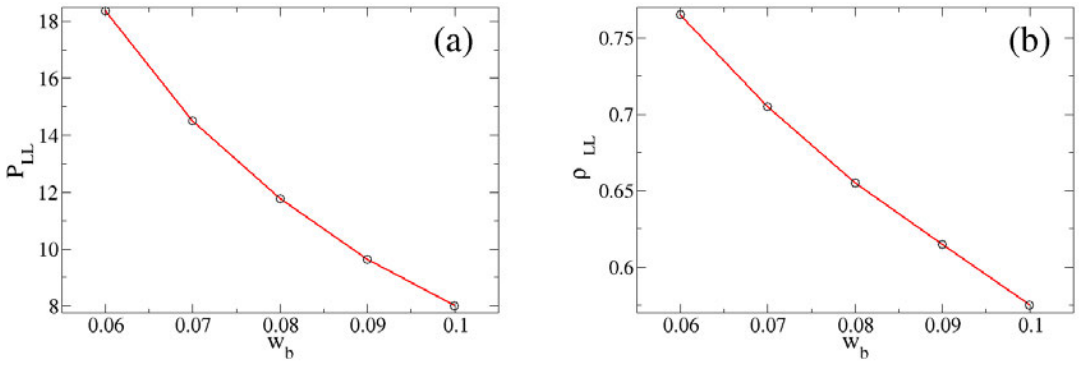

Figure 4·5: The dependence of the liquid-liquid critical point parameters on the bond width for $z = 1$, $\epsilon_1 = -12$, $w = 0.5$, $d = 0.1$, $\epsilon_b = 6$, $w_1 = 2w_b$

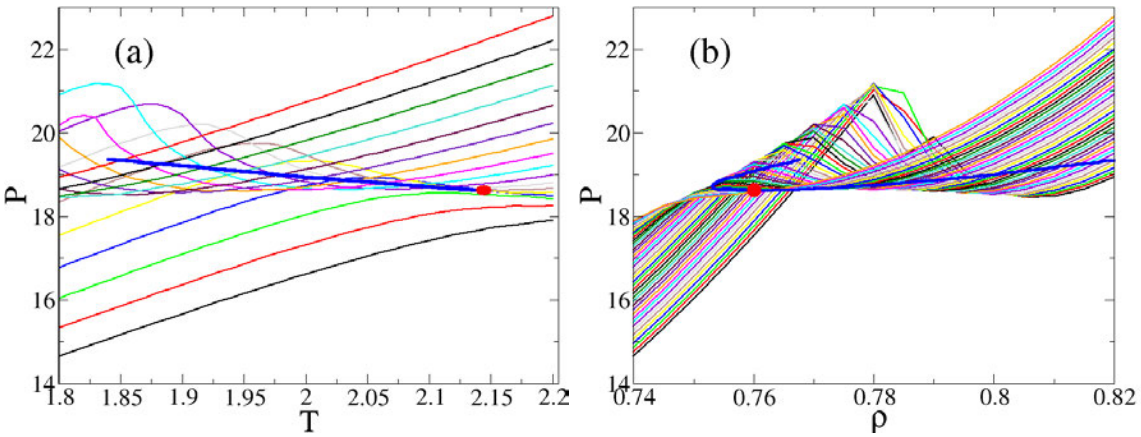

Figure 4·6: Phase diagrams for the maximum-valence model of dimerization, $z = 1$, ($w_b = 0.06$) obtained in an NVT ensemble after $t = 10^6$ time units. (a) The isochores in the $P - T$ plane are $\rho = 0.96 - 1.20$ for $\rho = 0.760 - 0.820$ in steps $\Delta T = 0.01$. (b) The isotherms in the P-ρ plane fir $T = 1.80 - 2.20$ in steps $\Delta T = 0.01$. In both figures, the liquid-liquid coexistence curves are calculated via the Maxwell construction and indicated by the blue curves. The liquid-liquid ($T_c^{LL} = 2.14434$, $P_c^{LL} = 18.618$, $\rho_c^{LL} = 0.670$) critical points are indicated by the red circles. Other parameters are the same as in Fig. 4·4

model to describe liquid polyamorphism in a variety of chemically-reacting fluids. The model combines the ideas of two-state thermodynamics (Anisimov et al., 2018b; Holten et al., 2014) with the maximum-valence approach (Zaccarelli et al., 2005; Speedy and Debenedetti, 1994; Speedy and Debenedetti, 1996), in which atoms may form covalent bonds via a reversible reaction, changing their state according to their bond number. By mimicking the valence structure and maximum bond number, z, our model predicts the LLPT in systems with dimerization ($z = 1$), polymerization ($z = 2$), and gelation ($z > 2$). As an example, we compare the molecular dynamics (MD) simulations with the phase behavior of sulfur. In particular, we show that when the bonded atoms attract each other stronger than to the unbonded atoms, phase separation is coupled to polymerization generating the LLPT in sulfur.

4.3.1 Maximum-Valence Model

We model the polymerization of a sulfur-like system ($z = 2$) by characterizing each atom by its coordination number, the number of bonds it has with other atoms. Depending on the coordination number, each atom is assigned to distinguished states: S_0 (with zero bonds), S_1 (with one bond), and S_2 (with two bonds). Atoms cannot form more than two bonds and, consequently, will polymerize into a linear polymer. All of the atoms in the system may change their state by forming or breaking a covalent bond via a reversible reaction. Fig. 4·7a depicts the three types of reversible reactions that may occur in the system. In this work, we demonstrate that the minimum ingredients required to produce a LLPT are the following: i) the van der Waals interactions between atoms, which produce a LGPT; ii) covalent bonds between atoms, which induce polymerization; and iii), as we hypothesize, additional van der Waals interactions between atoms with maximum valency (having two bonds), which couple phase segregation to polymerization. These three ingredients are illustrated by square-well potentials in Figs. 4·7(b-d).

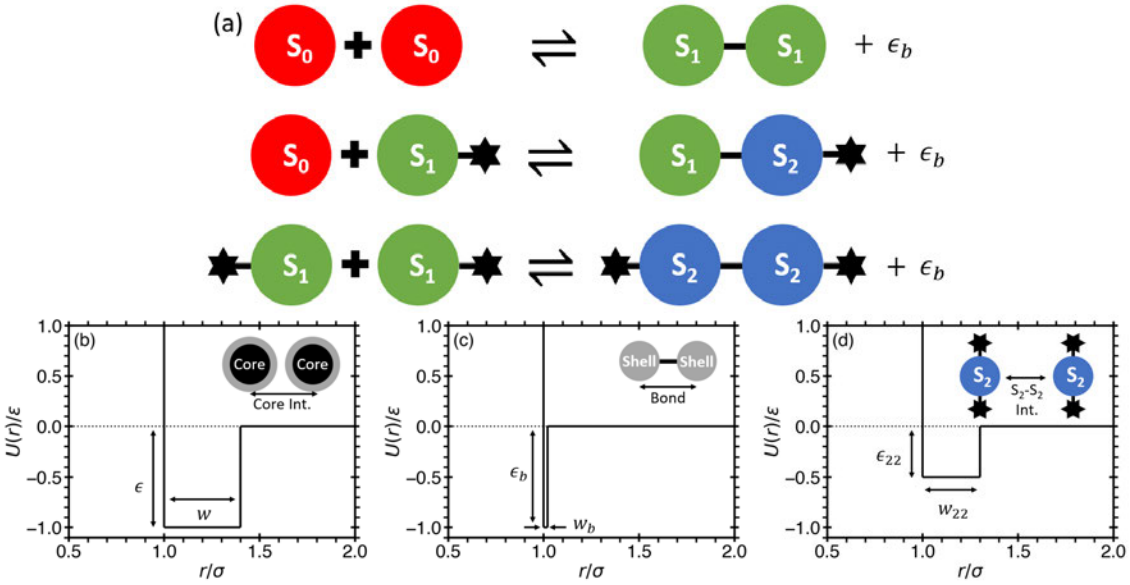

Figure 4·7: Reactions and interactions in the maximum-valence model. (a) The three types of covalent bond-forming reversible chemical reactions that may occur in the system. If two atoms without bonds (S_0) collide with each other, they may form a bond and become S_1 atoms. If a S_0 and S_1 atom collide, they may form a bond and become S_1 and S_2 atoms, respectively. If two S_1 atoms collide with each other, they form an additional bond and become S_2 atoms. (b-d) The three major interactions between atoms, in which each atom is composed of a core and shell, both with a radius σ and mass m. $U(r)$ is the pair potential energy and r is the distance from the center of an atom. (b) The cores of each atom interact with an attractive square well of depth $\epsilon = 1$ and width $w = 0.4$. (c) The shells may react to form covalent bonds that consist of a narrow well with depth $\epsilon_b = 1$ and width $w_b = 0.02$. (d) Phase segregation is coupled to polymerization via the additional attractive interactions between atoms in state S_2, described by a square well of depth $\epsilon_{22} = 0.5$ and width $w_{22} = 0.3$.

Physically, the additional attraction between atoms in neighboring chains may stem from the fact that in real polymers the covalent bond is shorter than the diameter of the unbonded ("free") atoms, such that the attractive wells of bonded atoms in neighboring chains overlap with each other (Stell and Hemmer, 1972; Stillinger and Head-Gordon, 1993; Jagla, 2001; Franzese et al., 2001; Gibson and Wilding, 2006; Skibinsky et al., 2004). This effectively creates an additional zone of attraction between polymer chains, which is a common attribute that produces LLPTs in soft-core potentials (Jagla, 2001; Franzese et al., 2001). In these models, the atoms which

penetrate the soft-core, can be regarded as bonded, which generate an additional "effective" attractive well due to the fact that such "bonded" atoms have more neighbors in their attractive range (Buldyrev et al., 2010). However, the explicit shortening of the covalent bonds between atoms would require the development of a microscopic Hamiltonian for this phenomenon, which would be most desirable for a future study. Therefore, in this work, for simplicity, instead of shortening the length of the covalent bonds, this effect is accounted for in the model through the additional "effective" square-well attraction (iii). Without this potential, with characteristic energy ϵ_{22}, and consequently, in the absence of polymerized atoms, no LLPT will occur. We note that this simplification is in the spirit of common semi-phenomenological models of non-ideal binary mixtures, such as the Flory-Huggins theory of polymer solutions (Flory, 1941; Huggins, 1941; Chan and Rey, 1996; Luo, 2006) or a regular-solution model (Hildebrand and Scott, 1962).

To verify our hypothesis, we implement these three ingredients of interactions via an event-driven MD technique (Alder and Wainwright, 1959; Rapaport, 2004); in particular, we use a discrete MD package (DMD) that only includes particles interacting through spherically-symmetric step-wise potentials, which may form bonds via reversible reactions (Buldyrev, 2009). We simulate an NVT ensemble of $N = 1000$ atoms in a cubic box with periodic boundaries at various constant densities and temperatures. The temperature is controlled by a Berendsen thermostat (Berendsen et al., 1984). The van der Waals and covalent-bonding interactions are implemented by separating each atom into two overlapping hard spheres (a core and a shell), with the same diameter σ and mass m, see Figs. 4·7(b-d). The connection between the core and its shell is represented by an infinite square-well potential of width $d \ll \sigma$. The cores and shells of different atoms do not interact with each other. The core represents the atom without its valence electrons. It interacts with other cores via a wide poten-

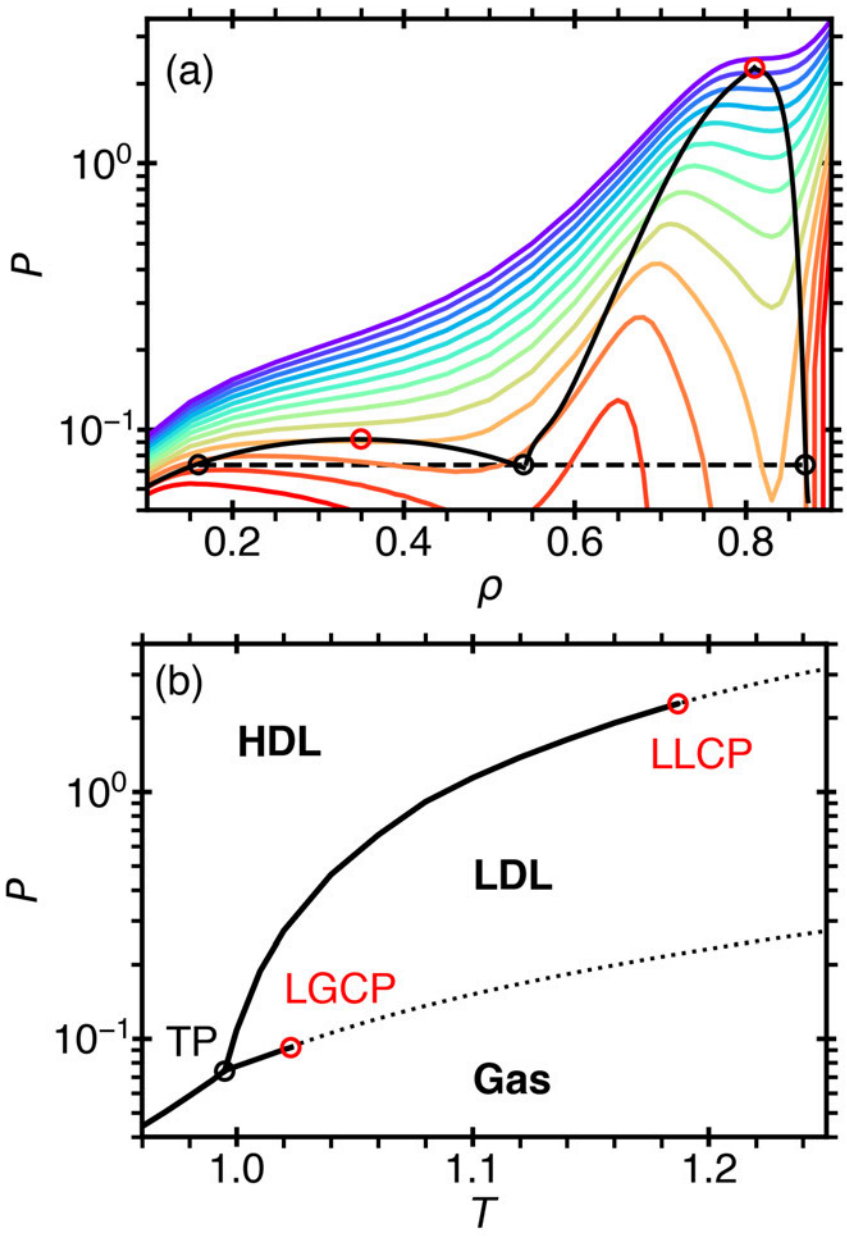

Figure 4·8: Phase diagrams for the maximum-valence model (with $\epsilon_{22} = 0.5$ and $\epsilon_b = 1.0$) obtained in an NVT ensemble after $t = 10^6$ time units. (a) The isotherms in the P-ρ plane are $T = 0.96 - 1.20$ (red-purple) in steps $\Delta T = 0.02$. (b) The liquid-gas and liquid-liquid critical isochores in the P-T plane are $\rho_c^{\rm LG} = 0.35$ and $\rho_c^{\rm LL} = 0.81$ as indicated by the lower and upper dashed lines, respectively. In both figures, the liquid-gas and liquid-liquid coexistence curves are calculated via the Maxwell construction and indicated by the solid curves. The liquid-gas ($T_c^{\rm LG} = 1.023$, $P_c^{\rm LG} = 0.0922$, $\rho_c^{\rm LG} = 0.35$) and liquid-liquid ($T_c^{\rm LL} = 1.187$, $P_c^{\rm LL} = 2.28$, $\rho_c^{\rm LL} = 0.81$) critical points are indicated by the red open circles, while the triple point ($P^{\rm TP} = 0.0738$, $T^{\rm TP} = 0.995$) is indicated by the black open circles.

tial well with depth ϵ and width $w = 0.4\sigma$ (the parameters are chosen as an example, Fig. 4·7b), which models the van der Waals interactions in the system. Meanwhile, the shell represents the outer valence electron cloud. It interacts with other shells via a narrow potential well with depth $\epsilon_b = \epsilon$ and width $w_b = 0.02\sigma$ (Fig. 4·7c), which models the breaking and forming of covalent bonds. In the absence of the shell, this system has a liquid-gas critical point (LGCP) at $\rho_c^{\mathrm{LG}} = N/V = 0.35 \pm 0.05$, $T_c^{\mathrm{LG}} = 1.04 \pm 0.01$, and $P_c^{\mathrm{LG}} = 0.094 \pm 0.005$ (Skibinsky et al., 2004), well above the equilibrium crystallization line, which we force to be at low temperature by selecting the appropriate width, w, of the potential. We note that all physical parameters are normalized by the appropriate combination of mass m, length σ, and energy ϵ units, as used in Ref. (Skibinsky et al., 2004). When the shell interactions are included and the system may form covalent bonds, the location of the LGCP changes, but not significantly. In addition to the wide and narrow wells, we introduce an additional attractive potential well (with depth $\epsilon_{22} = 0.5\epsilon$ and width $w_{22} = 0.3\sigma$, Fig. 4·7d) for the van der Waals interaction between the shells of the atoms with two bonds (both in the state S_2), which are not chemically bonded to each other.

We note that during either the formation or breaking of a bond, the new state of the reacting particles may modify the potential energy of the interactions with their non-bonded neighboring particles (Buldyrev, 2009). In our model, this occurs when particles in the state S_1 convert to the state S_2 (or vice versa). To maintain the conservation of energy, we calculate the change of the total potential energy, ΔU, due to the change of the state of the reacting particles and subtract it from the kinetic energy of the reacting pair. As a consequence, the equations for computing the new velocities (Buldyrev, 2009) may not have real solutions. In this case, the bond will not form or break, and the reacting particles will conserve their states through an elastic collision.

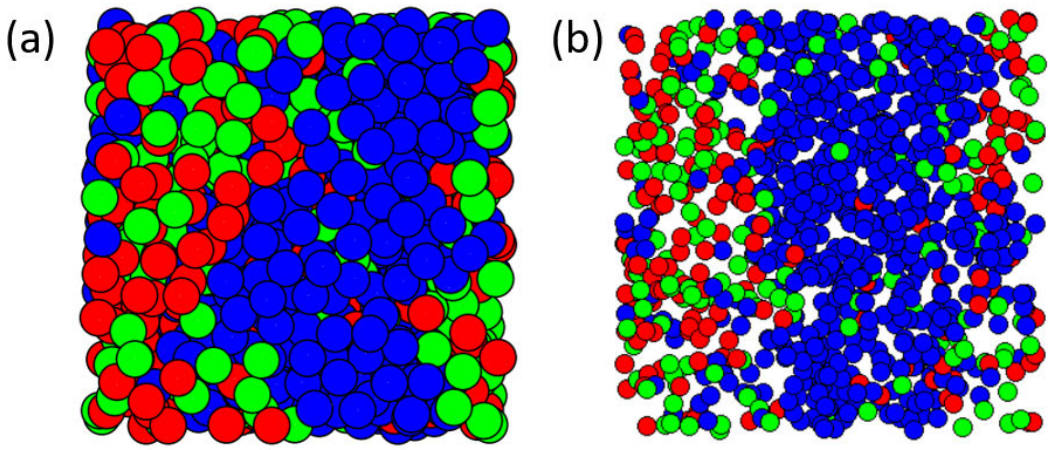

Figure 4·9: Simulation snapshots of the system exhibiting phase segregation at $T = 1.00$ and $\rho = 0.75$ in the LL coexistence region for a) $N = 1000$ and b) $N = 8000$ (in which the image size is reduced by a factor of two). Red, green, and blue spheres indicate atom states: S_0, S_1 and S_2, respectively.

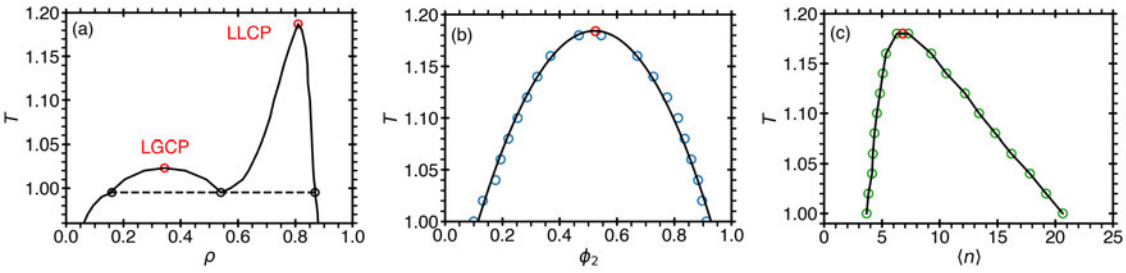

Figure 4·10: (a) T-ρ phase diagram for the maximum-valence model (with $\epsilon_{22} = 0.5$ and $\epsilon_b = 1.0$) obtained in an NVT ensemble after $t = 10^6$ time units. The temperature dependence of the fraction of atoms with two bonds, ϕ_2, (b) and the average chain-length, $\langle n \rangle$, (c) in two coexisting liquid phases. The simulation data in (b) is fit to a second order polynomial, while in (c) the curve is provided as a guide.

In this work, we obtain a detailed phase diagram of the model using the values of the square-well depths and widths illustrated in Figs. 4·7(b-d). In addition, we investigate the effect of ϵ_b and ϵ_{22} on the position of the liquid-liquid (LLCP) and liquid-gas (LGCP) critical points.

4.3.2 Results: Liquid-Liquid Phase Transition

Figure 4·8a illustrates isotherms on a pressure-density (P-ρ) plane, which exhibit two sets of van der Waals loops. The loops correspond to the LGCP, located at low density and pressure, and the LLCP, located at a higher density and pressure. Fig. 4·8b illustrates the LG and LL coexistence on a P-T plane along with the critical isochores. At the triple point (TP), the gaseous, LDL, and HDL phases coexist. In contrast to the ST2 model for water (Poole et al., 1992), but in agreement with spherically symmetric models (Franzese et al., 2001; Luo et al., 2015), the P-T line of the LL coexistence has a positive slope. Simulation snapshots depicted in Fig. 4·9 show the segregation of polymer-rich, HDL, and polymer-poor, LDL, phases.

Figure 4·10a presents the LG and LL coexistence curves on a T-ρ phase diagram. Although there is a distribution of polymer chains with varying lengths, a simple way to characterize the degree of polymerization is to find the fractions ϕ_0, ϕ_1 and ϕ_2 of atoms in states S_0, S_1 and S_2. Due to the conservation of the number of atoms, $\phi_0 + \phi_1 + \phi_2 = 1$. The fraction ϕ_2 was computed based on the asymmetric LL coexistence curve (Fig. 4·10a). Remarkably, ϕ_2 was found to be symmetric and centered around $\phi_2 = 0.5$ as shown in Fig. 4·10b. Consequently, the sum $\phi_0 + \phi_1 = 1 - \phi_2$ has the same symmetry. This feature suggests that $1 - \phi_2$ may be viewed as the appropriate order parameter for the LLPT coupled with polymerization. In contrast, the density, $\rho - \rho_c^{LG}$, is the order parameter for the LGPT, as commonly accepted. The symmetric nature of ϕ_2, and the fact that S_1 atoms are the intermediate states in the formation of polymer chains, enables a two-state thermodynamic approach (Anisimov

et al., 2018b) by reducing this model to two alternative states, with fractions ϕ_2 and $\phi_0 + \phi_1$.

The LLPT coexistence curve on the T-$\langle n \rangle$ plane (Fig. 4·10c), where $\langle n \rangle$ is the average length of a polymer chain among those containing at least one atom in state S_2, namely trimers or longer polymer chains. The strong temperature dependence of $\langle n \rangle$ in the phase segregation region proves that the LLPT is associated with polymerization. Neither ϕ_2 nor $\langle n \rangle$ shows any discontinuity as a function of density and temperature, although $\langle n \rangle$ shows a strong asymmetry toward the HDL phase.

4.3.3 Location of the Critical Points

With the values of parameters considered in the previous sections, the system acquires a LLPT terminating at a second critical point located at $T_c^{LL} = 1.187$, $P_c^{LL} = 2.28$ and $\rho_c^{LL} = 0.81$. We have investigated the dependency of the location of the LLCP and LGCP on the the three key parameters of the model: the range of van der Waals interactions w, the bond strength ϵ_b, and the interaction energy between bonded and unbonded atoms, ϵ_{22}, presented in Fig. 4·11. Each of the parameter sets produced a LLCP at much higher pressures than the LGCP, which practically remains the same as the square-well model without bonds (Xu et al., 2005). We observed that the reduction of the interaction energy, ϵ_{22} proportionally reduces T_c^{LL} and P_c^{LL} (see Figs. 4·11a,b). This indicates that the attraction between atoms in state S_2 is crucial for the existence of the LLPT, since decreasing the interaction energy further decreases P_c^{LL} to negative pressures and, eventually, to a point in the metastable region below the liquid-gas coexistence curve, where the LLCP effectively disappears. We find that for all simulations with $\epsilon_{22} > 0.55\epsilon$, the LGCP moves into the metastable region of the LLCP and effectively disappears, while for $\epsilon_{22} < 0.35\epsilon$, the interactions between polymer chains are too weak to produce the LLCP.

In contrast, increasing the bond strength, ϵ_b, does not indicate that the LLCP is going to disappear. Increasing the bond energy produces a slight increase in T_c^{LL} and ρ_c^{LL}, while producing a significant decrease in P_c^{LL} as shown in Figs. 4·11(a-c). We note that when the bond energy becomes larger than the van der Waals interaction energy, $\epsilon_b > \epsilon$, the LLCP drops to negative pressures (or in some cases, drops below the crystallization line) and may disappear. This indicates that increasing the strength of polymer bonds is not crucial for the existence of the LLPT. In addition, we found that by increasing the width of the van der Waals interaction potential attraction between cores, w, causes T_c^{LL} to increase slightly, while producing a greater increase in T_c^{LG} (see Fig. 4·11d). Meanwhile, increasing w causes the inverse effect in P_c^{LL} and P_c^{LG}, while leaving ρ_c^{LL} and ρ_c^{LG} essentially unaffected. We note that the maximum-valence model produces a LLCP even when the bond energy is zero (as shown for in Figs. 4·11(a-c) for $w = 0.4\sigma$). This indicates that the interplay between the van der Waals interaction and the attraction between bonded atoms is crucial to generate the LLPT, while the strength of the bond is secondary to this effect.

To compare the critical point behavior in the maximum-valence model with sulfur, we considered the ratio of the LLCP and LGCP critical-point parameters. For sulfur, these ratios are $P_c^{LL}/P_c^{LG} = 104$, $T_c^{LL}/T_c^{LG} = 0.78$, and $\rho_c^{LL}/\rho_c^{LG} = 3.4$ (Henry et al., 2020; Lide, 2003). Fig. 4·11 depicts the behavior of the critical-point parameters for the maximum valence model. As illustrated in Fig. 4·11a, we find that the ratio of critical pressures scales linearly with ϵ_{22} and exponentially with ϵ_b as $P_c^{LL}/P_c^{LG} \sim 460(\epsilon_{22}/\epsilon)e^{-\epsilon_b/(0.55\epsilon)}$. We also find that the liquid-liquid critical temperature is linearly related to ϵ_b and ϵ_{22} as $T_c^{LL}/T_c^{LG} \sim -1.27\epsilon_b\epsilon_{22}/\epsilon^2$ (see Fig. 4·11b), while also being inversely proportional to w as the ratio $T_c^{LL}/T_c^{LG} \approx 0.54\sigma/w$ (see Fig. 4·11d). Meanwhile, as illustrated in Fig. 4·11c, the critical density shows a general decreasing trend with increase of ϵ_b. From the general trends presented in Fig. 4·11,

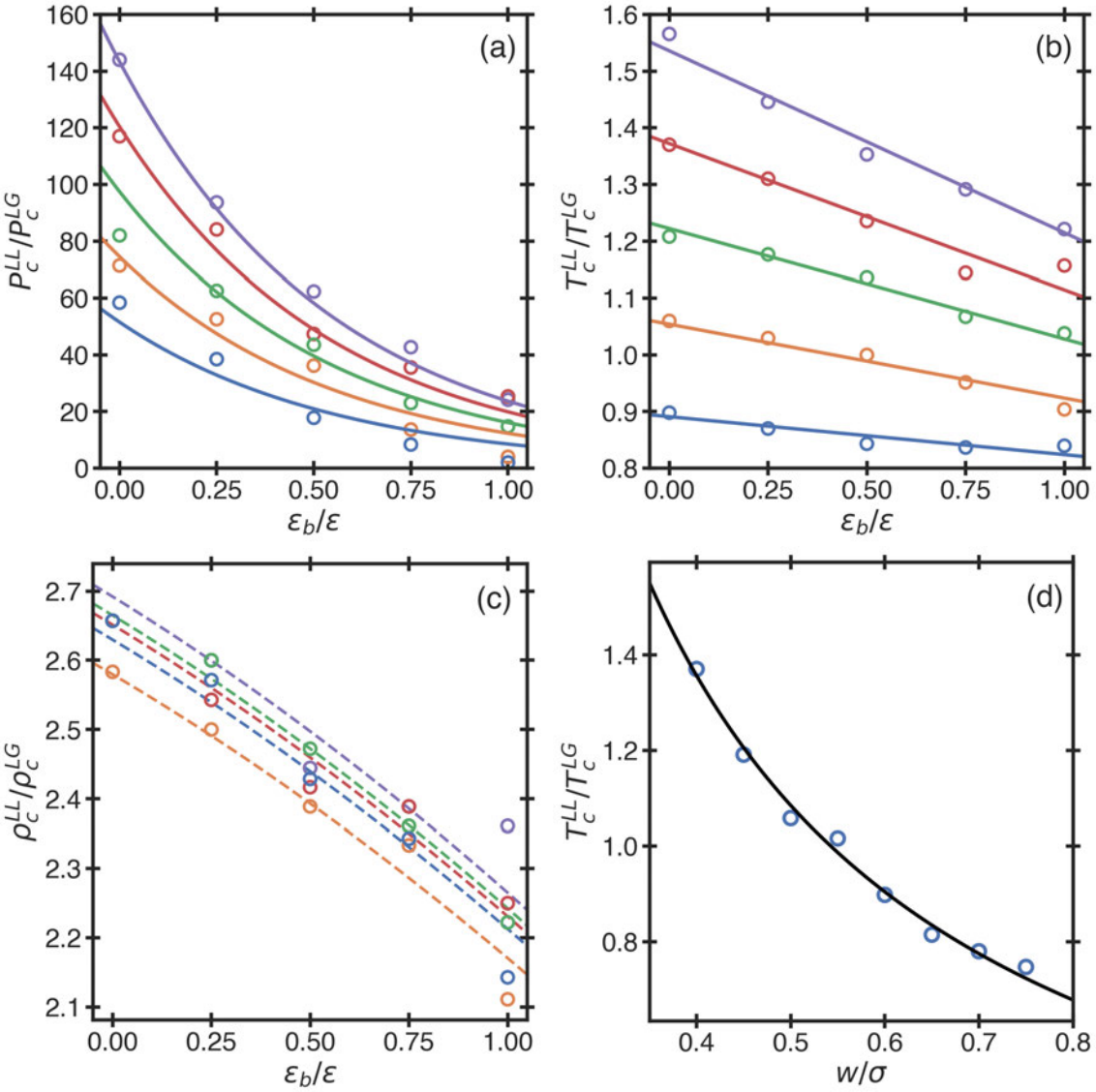

Figure 4·11: The effect of different interaction parameters on the critical point locations in the maximum-valence model. In (a-c), for $w = 0.4\sigma$ for increasing the bond energy, ϵ_b, with interaction energy between bonded atoms: $\epsilon_{22} = 0.55\epsilon$ (purple), $\epsilon_{22} = 0.50\epsilon$ (red), $\epsilon_{22} = 0.45\epsilon$ (green), $\epsilon_{22} = 0.4\epsilon$ (orange), and $\epsilon_{22} = 0.35\epsilon$ (blue). In (a), the ratio of the critical pressures exponentially decreases as $P_c^{LL}/P_c^{LG} \sim 460(\epsilon_{22}/\epsilon)\exp\left[-\epsilon_b/(0.55\epsilon)\right]$, while in (b) the ratio of the critical temperatures decreases linearly as $T_c^{LL}/T_c^{LG} \sim -1.27\epsilon_b\epsilon_{22}/\epsilon^2$, and in (c), the ratio of critical densities shows a general decreasing trend indicated by the second-order polynomial guidelines (dashed). In (d), the ratio of the critical temperatures is inversely related to the width of the van der Waals interaction well, $T_c^{LL}/T_c^{LG} = 0.54\sigma/w$, for $\epsilon_{22} = 0.5\epsilon$ and $\epsilon_b = 0.5\epsilon$.

we find that the best parameter sets in the maximum-valence model that produce ratios that match with sulfur exist for large van der Waals interaction potential, w, and small bond energies, $\epsilon_b \ll \epsilon$ at large interaction potentials between bonded atoms ϵ_{22}. For $w = 0.7\sigma$, $\epsilon_{22} = 0.5\epsilon$, and $\epsilon_b = 0.0\epsilon$, producing $P_c^{LL}/P_c^{LG} = 69.5$, $T_c^{LL}/T_c^{LG} = 0.78$, and $\rho_c^{LL}/\rho_c^{LG} = 3.30$, values which are close to the ratio in sulfur (Henry et al., 2020; Lide, 2003).

4.3.4 Further Comparisons with the Behavior of Sulfur

Qualitatively, the phase diagram of sulfur matches that of the maximum-valence model with a specific set of interaction parameters. In sulfur, the LGCP is located at $T_c^{LG} = 1314\,\mathrm{K}$, $P_c^{LG} = 20.7\,\mathrm{MPa}$, and $\rho_c^{LG} = 563\,\mathrm{kg/m^3}$ (Lide, 2003), while the LLCP is located at $T_c^{LL} = 1035\,\mathrm{K}$, $P_c^{LL} = 2.15\,\mathrm{GPa}$, and $\rho_c^{LL} \approx 2000\,\mathrm{kg/m^3}$ (Henry et al., 2020), such that the ratio of the LL to LG critical parameters qualitatively matches the predictions of the maximum-valence model. We note that the behavior of sulfur is more complicated away from the LLPT since liquid sulfur contains octamers that (above the lambda transition (Tobolsky and Eisenberg, 1959; Sauer and Borst, 1967; Bellissent et al., 1994; Kozhevnikov et al., 2004; Eisenberg and Tobolsky, 1960)) are to be broken down upon heating before polymerization can occur (Tobolsky and Eisenberg, 1959). Since in the considered formulation of the maximum-valence model, we consider atoms that form linear polymers, this mimics the valence structure and bond formation of sulfur in the vicinity of the LLPT.

Also, the computed structure factor contains qualitative similarities with the LLPT in sulfur. In Fig. 4·12, we depict the structural differences between the LDL and HDL phases through the density correlation function, $g(r)$, and the structure factor, $S(q)$, for several densities at constant temperature near the liquid-liquid coexistence (computed for the atom cores). In Fig. 4·12a, the $g(r)$ shows a sharp peak corresponding to the covalent bond length $r = 1.02\sigma$, in the HDL phase. Correspond-

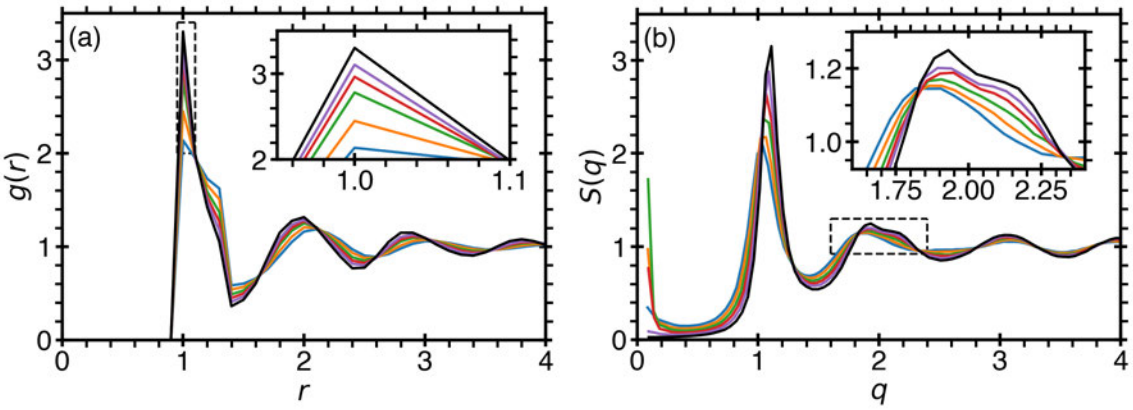

Figure 4·12: (a) The density correlation function $g(r)$ and (b) the structure factor $S(q)$ across the liquid-liquid transition at $T = 1.00$ for densities of $\rho = 0.65$ (blue), $\rho = 0.70$ (orange), $\rho = 0.75$ (green), $\rho = 0.80$ (red), $\rho = 0.85$ (purple), and $\rho = 0.90$ (black). In (a), the sharp peak, around $r = 1$ (in units of σ), corresponds to the length of the covalent bond, which increases upon increasing density. Simultaneously, in (b), the maximum of the structure factor (the first peak) shifts to larger wavenumbers upon increasing density, while the second peak acquires a characteristic bump, similar to what was recently observed in sulfur (Henry et al., 2020). The divergence of the structure factor at $q = 0$ indicates the divergence of the isothermal compressibility in the vicinity of the LLCP. The insets (dashed boxes) highlight the behavior of the maximum of the correlation function and second peak of the structure factor.

ingly, the structure factor shows a shift in the first peak to a larger wavenumber q, while the second peak changes due to polymerization. This change is similar to what was observed in a recent experiment on sulfur (Henry et al., 2020). In addition, $S(q)$ shows a dramatic increase as $q \to 0$ for the points corresponding to the equilibrium between two liquid phases (see Fig. 4·12b), which is indicative of the divergence of the isothermal compressibility. We note that in this work, we find a gas-LDL-HDL triple point, while in the recent experimental work on sulfur (Henry et al., 2020), the solid-LDL-HDL triple point is observed. In principle, this triple point may be reproduced in the maximum-valence model by fine-tuning the parameters, which requires further investigation.

4.3.5 Conclusion

The maximum-valence model describes liquid polyamorphism in a variety of chemically-reacting fluids. By tuning the maximum valency, z (maximum coordination number), of the model, the liquid-liquid phase transitions (LLPT) in these systems could be investigated. We show that when the bonded atoms attract each other stronger than the non-bonded atoms or when the bonded and non-bonded atoms repel each other, the LLPT is generated by the coupling between phase separation and the chemical reaction. In this work, we compared the model with $z = 2$ to the behavior of liquid sulfur. Our results show that the LLPT predicted by the model qualitatively reproduces the LLPT in sulfur at a high pressure and temperature.

The model could also be used to study the LLPTs in systems with other maximum valence numbers. For instance, when $z = 1$, the LLPT is induced by dimerization (e.g. hydrogen at extremely large pressures (Ohta et al., 2015; McWilliams et al., 2016; Dzyabura et al., 2013; Zaghoo et al., 2016; Zaghoo and Silvera, 2017)). For $z \geq 3$, the LLPT could be induced either by gelation or by molecular network formation (Zaccarelli et al., 2005). For example, it could be used to model the phase behavior

of liquid phosphorous with $z = 3$ (Katayama et al., 2000; Katayama et al., 2004) as well as silicon (Sciortino, 2011), silica (Lascaris et al., 2014a; Chen et al., 2017), or supercooled water with $z > 3$ (Gallo et al., 2016a; Speedy and Debenedetti, 1996). In a future study, the two-state thermodynamics of liquid polyamorphism (Anisimov et al., 2018b; Caupin and Anisimov, 2021; Longo and Anisimov, 2022) could be applied to these systems to develop the equation of state, which would determine the anomalies of the physical properties in this system, especially near the critical points.

4.4 Gelation / Network Formation (Z = 3, 4, 5, 6)

We can generalize our model for any arbitrary coordination number z. So far we have discussed in details only dimerization, $z = 1$, and polymerization, $z = 2$ for attractive interaction between B_2 atoms (Shumovskyi et al., 2022). Upon studying other $z > 2$, we found that our generic maximal valence model also produces liquid-liquid phase transitions induced by molecular interconversion in polyamorphic substances for higher z as well, up to the point the critical density becomes so high that the LLCP moves below the crystallization line.

Fig. 4·13 shows the dependence of critical parameters, critical temperature T_c, critical pressure P_c and critical density ρ_c, on the coordination number z, while keeping all other parameters constant ($w = 0.5$, $w_b = 0.1$, $w_z = 0.2$, $d = 0.1$, $\epsilon_b = 6$, $\epsilon_z = -6$). Upon increasing z the liquid-liquid critical temperature decreases, while the liquid-gas critical temperature increases. Physically the temperature of LGCP increases upon increasing the coordination number z, because the overall attraction increases. However, as z increases both LG and LL critical pressures increase. We know that since T_c^{LG} is increasing, it forces the pressure of liquid-gas also to increase. As for the density of LGCP, it only slightly increases for high z. On the other hand, the density of the LLCP increases from approximately 0.6 to 1. This is because the

density of the low density phase which consists of atoms with coordination number z increases with z at a constant bond length. When $z = 6$ the network density coincides with the density of the simple cubic lattice which has coordination number 6. For higher z the LLPT becomes submerged below the crystallization line of the body-centered cubic lattice. The pressure needed to create such a density also increases, so we see that the LLCP pressure increases with z. However the temperature of the LLCP decreases with z because the entropy difference between more ordered low density phase with maximal coordination number z and disordered high density phase with coordination number $z - 1$, becomes smaller and hence a lower temperature is needed to stabilize the low density phase.

The choice of parameters for our model is quite simple and natural. In reality, a wide region in the parameter space produces a phase diagram with a region of density anomaly and a LLCP with a negatively sloped coexistence line, like it happens in water(Poole et al., 1992). In the previous section we find that for $z = 1$, the slope of the coexistence line is negative only for large additional repulsive interaction for the dimerized atoms $\epsilon_1 \approx -2\epsilon_b$. For larger z the the slope becomes more negative even for weaker repulsion $\epsilon_z = -\epsilon_b$ (Fig. 4·14). We also observe (Fig. 4·13) that for larger z the LLCP temperature decreases and becomes much smaller than LGCP like in water. This indicates that the maximal valence model with $z = 4$ is a plausible model for water and other substances forming tertrahedral networks such as silica and silicon.

4.5 Conclusion

The maximum-valence model describes liquid polyamorphism in a variety of chemically-reacting fluids. By tuning the maximum valency, z (maximum coordination number), of the model, the liquid-liquid phase transitions (LLPT) in these systems can be in-

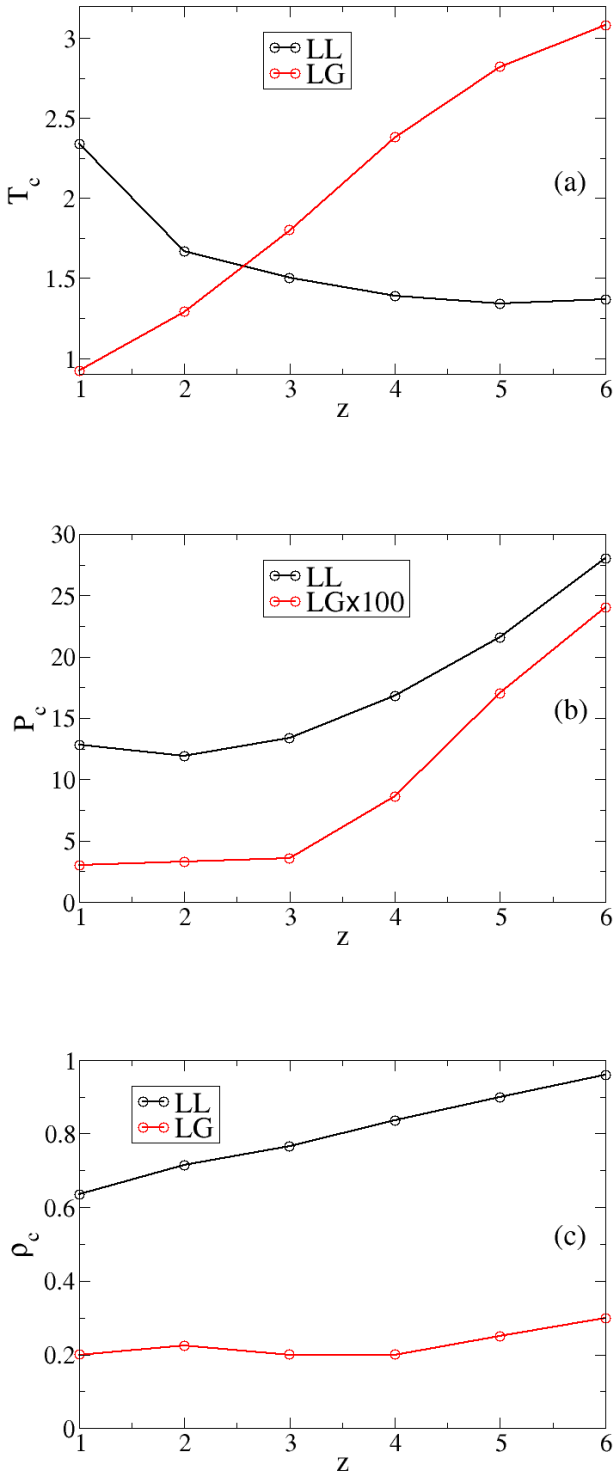

Figure 4·13: The dependence of the Liquid-liquid critical point parameters on coordination number z. The parameters are: $w = 0.5$, $w_b = 0.1$, $w_z = 0.2$, $d = 0.1$, $\epsilon_b = 6$, $\epsilon_z = -6$

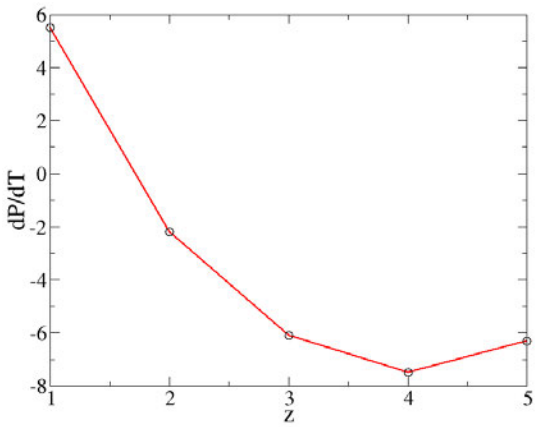

Figure 4·14: The dependence of the slope of the liquid-liquid coexistence line on coordination number z. The parameters are: $w = 0.5$, $w_b = 0.1$, $w_z = 0.2$, $d = 0.1$, $\epsilon_b = 6$, $\epsilon_z = -6$

vestigated. We show that when the atoms with maximal valence $k = z$ repel atoms with valence $k \leq z$, the LLPT is generated by the coupling between phase separation and the chemical reactions.

We showed that when $z = 1$, the LLPT is induced by dimerization (e.g. hydrogen at extremely large pressures(Dalladay-Simpson et al., 2016b)). We described how by tuning the size of the molecule relatively to the atomic hydrogen radius, our model may be used to reproduce the real hydrogen. By decreasing the difference between the bond length, w_b, and the repulsive range of the atoms in the molecule, w_1, one may reduce the difference between percentage of high- and low- density phases to 6%, while in the real hydrogen this difference is reported to be approximately 2% (Fried et al., 2022). After reducing the difference between the w_b and w_1 even further, the system crystallizes. Since the exact position of the LLCP in hydrogen is still under debate(Fried et al., 2022), our results suggest that 2% difference between high- and low- density phases is inconsistent with the existence of the LLPT above the crystallization line.

In our previous work for $z = 2$, we showed that LLPT induced by polymerization

could describe LLPT in sulfur(Shumovskyi et al., 2022). For $z \geq 3$, the LLPT could be induced either by gelation or by molecular network formation (Zaccarelli et al., 2005). For example, it could be used to model the phase behavior of liquid phosphorous with $z = 3$ (Katayama et al., 2000; Katayama et al., 2004) or supercooled water with $z > 3$ (Gallo et al., 2016a; Speedy and Debenedetti, 1996). Indeed for high values of z we obtained the negative slope of the coexistence line on $P-T$ plane as well as the relationships between the critical parameters of the model, $T_c^{LG} \gg T_c^{LL}$ and $P_c^{LG} \ll P_c^{LL}$, which qualitatively reproduces the real water experiments (Kim et al., 2020) and simulations of more accurate all-atom models.

In a future study, the two-state thermodynamics of liquid polyamorphism (Anisimov et al., 2018b; Caupin and Anisimov, 2021; Longo and Anisimov, 2022; Fried et al., 2022) could be applied to these systems to develop the equation of state, which would determine the anomalies of the physical properties in these systems, especially near the critical points.

Chapter 5

Summary and outlook

In this dissertation, we explored liquid-liquid phase transitions induced by molecular interconversion in polyamorphic substances. Firstly, we talked about the history of liquid-liquid phase transitions, as well as the motivation to study such systems using theoretical and numerical techniques, such as simulations of Hybrid Lattice Model using Monte-Carlo approach and Hard-Core Shoulder model using Discrete Molecular Dynamics.

Further, in the second chapter, we studied the phenomenon of phase amplification, phase separation and emergent dissipative structures in the substances with molecular interconversion. At first, we investigated a fluid, composed of two immiscible molecular species, which are allowed to interconvert. We modeled the system using Kawasaki-Ising model, which combines Glauber-interconversion and Kawasaki-diffusion dynamics, that produced us the phenomenon of phase amplification, the growth of one phase at the expense of another one. We found that whenever the probability of Glauber dynamics is not zero, the phase amplification always takes place, and we derived and verified numerically the scaling laws of the growth of the order-parameter in the system. Secondly, we investigated the effects of the source of forced interconversion, when it is introduced into the Hybrid Lattice model through a tunable imbalance in the internal energy via the energy of forced interconversion, such that the source boosts the probability for two alternative species to interconvert into equal amounts. If forced interconversion is not strong enough to overcome natural

interconversion (which corresponds to equilibrium conditions), then phase amplification (the growth of one stable phase at the expense of the other) is observed, provided that the natural interconversion probability is significant. If forced interconversion overcomes natural interconversion by a sufficient amount, we observe that the locally phase-separated domains stop growing upon reaching a characteristic size. So the dissipative structures are observed and the steady-state domain size decreases as the energy of forced interconversion increases and as the temperature becomes closer to the critical temperature of demixing. Moreover, we find that the dissipative domain structure has the form of spatially-modulated stripes due to the symmetry.

As the last thing of the second chapter, we study the effect of the external source of the interconversion in an actual molecular system, using Hard-Core Shoulder model via Molecular Dynamics Simulations. In the HCS model, non-relativistic energy-carrying particles are introduced as a source of forced interconversion. Physically, it can be regarded as an external energy carried by an ATP molecule or another active agent, which can compensate the effect of the heat of mixing arising from interconversion. When the additional particles carry no extra energy, only natural interconversion will occur. However, due to the external source of energy provided by the particles, forced interconversion will occur just like in the previously considered model. As observed in the HCS model, for large system sizes, in the microphase separation region, one could observe more regular structures, like the nonequilibrium spatially-modulated stripes observed in the HL model. However, the off-lattice MD simulations produce nonequilibrium bicontinuous "microemulsion" structures.

Next in the 3rd chapter, we talked about the structure factor of a phase separating binary mixture with natural and forceful interconversion of species. We started from generalizing Cahn-Hilliard-Cook theory of spinodal decomposition to allow for both natural and forceful interconversion of species to derive the structure factor

for concentration fluctuations. Then we obtained the first-order solution for mixed diffusion-interconversion dynamics, which we compared to our numerical results of the spatial and temporal evolution of the order parameter from Landau-Ginzburg formalism, as well as the results of our simulations of nonequilibrium Ising/Lattice-Gas Hybrid model. We confirmed that the presence of a source of forceful interconversion causes the system to phase separate into steady-state microphase domains. Due to the periodic boundary conditions imposed in the continuum finite-difference method, we found that the stripe morphologies will form at any angle with respect to the simulation box. We have demonstrated that the presence of a source of forceful interconversion in a hybrid binary system that possesses both diffusion and natural interconversion dynamics may produce microphase separation. We also characterized the time evolution of the phase formation through two characteristic wavenumbers, q_m and q_-, which correspond to the maximum and lower cut-off wavenumbers of the amplification factor obtained from the generalized theory of spinodal decomposition. In the infinite time (steady-state) limit, we showed that $q_m(t \to \infty) \propto q_- \propto K^{1/2}$, where K is the rate of forceful interconversion. We compared the structure-factor theory with Monte Carlo simulations of a nonequilibrium hybrid model and demonstrated that the origin of microphase separation may be related to an external energy source, as $E \propto K^{1/2}$, which allows domain formation to be more energetically favorable.

Finally, chapter four is about our main topic of the dissertation, the Generic Maximal Valence Model. The outline is quite straightforward - first, we introduced our Maximal Valence Model. Next, we talked quite in details about the dimerization, the model with coordination number $z = 1$, then polymerization, the model with coordination number $z = 2$, and then we showed our results for any generic model with any other values of coordination number $z > 2$, which corresponds to gelation and network formation. We demonstrated, that the minimum ingredients required

to produce a LLPT are the following: i) the van der Waals interactions between atoms, which produce a LGPT; ii) covalent bonds between atoms, which induce polymerization; and iii), as we hypothesized, additional van der Waals interactions between atoms with maximum valency which couple phase segregation to association. We showed that when the bonded atoms attract each other stronger than the non-bonded atoms or when the bonded and non-bonded atoms repel each other, the LLPT is generated by the coupling between phase separation and the chemical reaction. Moreover, we showed that when the atoms with maximal valence $k = z$ repel atoms with valence $k \leq z$, the LLPT is generated by the coupling between phase separation and the chemical reactions.

Our generic maximal valence model produces liquid-liquid phase transitions induced by molecular interconversion in polyamorphic substances for any z up until to the point the critical density becomes so high LLCP moves below the crystallization line. Also, when z = 6 the network density coincides with the density of the simple cubic lattice which has coordination number 6. For higher values of z the LLPT becomes submerged below the crystallization line of the body-centered cubic lattice.

The future work could focus on the application of the two-state thermodynamics of liquid polyamorphism (Anisimov et al., 2018b; Caupin and Anisimov, 2021; Longo and Anisimov, 2022; Fried et al., 2022) to these systems to develop the equation of state, which would determine the anomalies of the physical properties in these systems, especially near the critical points.

References

Alder, B. J. and Wainwright, T. E. (1959). Studies in molecular dynamics. i. general method. *J. Chem. Phys.*, 31:459.

Allen, S. M. and Cahn, J. W. (1979). A microscopic theory for antiphase boundary motion and its application to antiphase domain coarsening. *Acta Metallurgica*, 27(6):1085–1095.

Amann-Winkel, K., Gainaru, C., Handle, P. H., Seidl, M., Nelson, H., Böhmer, R., and Loerting, T. (2013). Water's second glass transition. *PNAS*, 110(44):17720–17725.

Angell, C. A. (1971). Two-state thermodynamics and transport properties for water as zeroth-order results of a "bond lattice" model. *J. Physical Chemistry,* 75(24).

Angell, C. A. (2004). Amorphous water. *Annual Review of Physical Chemistry*, 55(1):559–583.

Anisimov, M. A. and Bertrand, C. E. (2010). *Thermodynamics of Fluids at Meso and Nano Scales*, chapter 7, pages 172–214.

Anisimov, M. A., Duska, M., Caupin, F., Amrhein, L. E., Rosenbaum, A., and Sadus, R. J. (2018a). Thermodynamics of Fluid Polyamorphism. *Physical Review X*, 8(1):011004.

Anisimov, M. A., Duška, M., Caupin, F., Amrhein, L. E., Rosenbaum, A., and Sadus, R. J. (2018b). Thermodynamics of fluid p olyamorphism. *P hys. R ev. X*, 8:011004.

Anisimov, M. A. and Wang, J. (2006). Nature of Asymmetry in Fluid Criticality. *Physical Review Letters*, 97(2):025703.

Bellissent, R., Descotes, L., and Pfeuty, P. (1994). Polymerization in liquid sulphur. *Journal of Physics: Condensed Matter*, 6(23A):A211–A216.

Berendsen, H. J. C., Postma, J. P. M., van Gunsteren, W. F., DiNola, A., and Haak, J. R. (1984). Molecular-dynamics with coupling to an external bath. *Journal of Chemical Physics*, 81(8):3684–3690.

Bhat, M. H., Molinero, V., Soignard, E., Solomon, V. C., Sastry, S., Yarger, J. L., and Angell, C. A. (2007). Vitrification of a monatomic metallic liquid. *Nature*, 448:787–790.

Biddle, J. W., Singh, R. S., Sparano, E. M., Ricci, F., González, M. A., Valeriani, C., Abascal, J. L. F., Debenedetti, P. G., Anisimov, M. A., , and Caupin, F. (2017). Two-structure thermodynamics for the tip4p/2005 model of water covering supercooled and deeply stretched regions. *J. of Chemical Physics*, 146:034502.

Billotet, C. and Binder, K. (1980). Dynamic correlation of fluctuations during spinodal decomposition. *Physica A: Statistical Mechanics and its Appl*, 103(1):99–118.

Binder, K. (1983). Collective diffusion, nucleation, and spinodal decomposition in polymer mixtures. *Journal of Chemical Physics,* 79:6387.

Binder, K., Billotet, C., and Mirold, P. (1978). On the theory of spinodal decomposition in solid and liquid binary mixtures. *Zeitschrift für Physik B Condensed Matter*, 30(2):183–195.

Bray, A. J. (2002). Theory of phase-ordering kinetics. *Adv. Physics,* 51(2):481–587.

Brazhkin, V. V., Popova, S. V., and Voloshin, R. N. (1999). Pressure -temperature phase diagram of molten elements: selenium, sulfur and iodine. *Physica B*, 265:64–71.

Buldyrev, S. (2009). Application of discrete molecular dynamics to protein folding and aggregation. In Franzese, G. and Rubi, M., editors, *Aspects of Physical Biology*, volume 752 of *Lecture Notes in Physics*, pages 97–132. Springer-Verlag, Berlin, Heidelberg.

Buldyrev, S. V., Kumar, P., Sastry, S., Stanley, H. E., and Weiner, S. (2010). Hydrophobic collapse and cold denaturation in the jagla model of water. *Journal of Physics: Condensed Matter*, 22:284109.

Cahn, J. W. (1965). Phase Separation by Spinodal Decomposition in Isotropic Systems. *The Journal of Chemical Physics*, 42(1):93–99.

Cahn, J. W. (1966). The later stages of spinodal decomposition and the beginnings of particle coarsening. *Acta Metallurgica*, 14:1685–1962.

Cahn, J. W. and Allen, S. M. (1977). A Microscopic Theory for Domain Wall Motion and Its Experimental Verification in Fe-Al Alloy Domain Growth Kinetics. *Le Journal de Physique Colloques*, 38(C7):C7–51–C7–54.

Carati, D. and Lefever, R. (1997). Chemical freezing of phase separation in immiscible binary mixtures. *Physical Review E*, 56(3):3127–3136.

Caupin, F. and Anisimov, M. A. (2019). Thermodynamics of supercooled and stretched water: Unifying two-structure description and liquid-vapor spinodal. *Journal of Chemical Physics*, 151:034503.

Caupin, F. and Anisimov, M. A. (2021). Minimal microscopic model for liquid polyamorphism and waterlike anomalies. *Physical Review Letters*, 127:185701.

Chan, P. K. and Rey, A. D. (1996). Polymerization-induced phase separation. 1. droplet size selection mechanism. *Macromolecules*, 29(27):8934–8941.

Chen, R., Lascaris, E., , and Palmer, J. C. (2017). Liquid–liquid phase transition in an ionic model of silica. *Journal of Chemical Physics,* 146:234503.

Cheng, B., Mazzola, G., Pickard, C. J., and Ceriotti, M. (2020). Evidence for supercritical behaviour of high-pressure liquid hydrogen. *Nature*, 585:217–220.

Christensen, J. J., Elder, K., and Fogedby, H. C. (1996). Phase segregation dynamics of a chemically reactive binary mixture. *Physical Review. E*, 54:R2212–R2215.

Coniglio, A. and Zannetti, M. (1989). Multiscaling in growth kinetics. *Europhysics Letters (EPL)*, 10(6):575–580.

Coniglio, A. and Zannetti, M. (1990). Novel dynamical scaling in kinetic growth phenomena. *Physica A: Statistical Mechanics and its Applications*, 163(1):325–333.

Cook, H. E. (1970). Brownian motion in spinodal decomposition. *Acta Metallurgica*, 18(3):297–306.

Dalladay-Simpson, P., Howie, R. T., and Gregoryanz, E. (2016a). Evidence for a new phase of dense hydrogen above 325 gigapascals. *Nature*, 529:63–67.

Dalladay-Simpson, P., Howie, R. T., and Gregoryanz, E. (2016b). Evidence for a new phase of dense hydrogen above 325 gigapascals. *Nature*, 529:63–67.

Das, S. K., Horbach, J., Binder, K., Fisher, M. E., and Sengers, J. V. (2006). Static and dynamic critical behavior of a symmetrical binary fluid: A computer simulation. *Journal of Chemical Physics*, 125:024506.

Debenedetti, P. G. (1998). One substance, two liquids? *Nature*, 392:127–128.

Debenedetti, P. G., Sciortino, F., and Zerze, G. H. (2020). Second critical point in two realistic models of water. *Science*, 369(6501):289–292.

Duška, M. (2020). Water above the spinodal. *J. Chem. Phys.*, 152:174501.

Dzyabura, V., Zaghoo, M., and Silvera, I. F. (2013). Evidence of a liquid-liquid phase transition in hot dense hydrogen. *Proceedings of the National Academy of Sciences U.S.A.*, 110(20):8040–8044.

Eisenberg, A. and Tobolsky, A. V. (1960). Equilibrium polymerization of selenium. *Journal of Polymer Science*, 46.

Enrique, R. A. and Bellon, P. (2001). Compositional patterning in immiscible alloys driven by irradiation. *Physical Review B*, 63(134111):45–65.

Fisher, M. E. (1983). Scaling, universality and renormalization group theory. In Hahne, F. J. W., editor, *Critical Phenomena*, Lecture Notes in Physics, pages 1–139, Berlin, Heidelberg.

Flory, P. J. (1941). Thermodynamics of high polymer solutions. *Journal of Chemical Physics,* 9:660.

Franzese, G., Malescio, G., Skibinsky, A., Buldyrev, S. V., and Stanley, H. E. (2001). Generic mechanism for generating a liquid-liquid phase transition. *Nature*, 409.

Fried, N. R., Longo, T. J., and An, M. A. (2022). Modeling fluid polyamorphism through a maximum-valence approach. *Journal of Chemical Physics,* 157:101101.

Gallo, P., Amann-Winkel, K., Angell, C. A., Anisimov, M. A., Caupin, F., Chakravarty, C., Lascaris, E., Loerting, T., Panagiotopoulos, A. Z., Russo, J., Sellberg, J. A., Stanley, H. E., Tanaka, H., Vega, C., Xu, L., and Pettersson, L. G. M. (2016a). Water: A tale of two liquids. *Chemical Reviews,* 116:7463–7500.

Gallo, P., Amann-Winkel, K., Angell, C. A., Anisimov, M. A., Caupin, F., Chakravarty, C., Lascaris, E., Loerting, T., Panagiotopoulos, A. Z., Russo, J., Sellberg, J. A., Stanley, H. E., Tanaka, H., Vega, C., Xu, L., and Pettersson, L. G. M. (2016b). Water: A tale of two liquids. *Chemical Reviews*, 116(13):7463–7500.

Geng, H. Y., Wu, Q., Marqués, M., and Ackland, G. J. (2019). Thermodynamic anomalies and three distinct liquid-liquid transitions in warm dense liquid hydrogen. *Physical Review. B*, 100:134109.

Gibson, H. M. and Wilding, N. B. (2006). Metastable liquid-liquid coexistence and density anomalies in a core-softened fluid. *Physical Review. E*, 73:061507.

Giovambattista, N., Loerting, T., Lukanov, B. R., and Starr, F. W. (2012). Interplay of the glass transition and the liquid-liquid phase transition in water. *Scientific Reports*, 2:390.

Glauber, R. J. (1963). Time-Dependent Statistics of the Ising Model. *Journal of Mathematical Physics*, 4(2):294–307.

Glosli, J. N. and Ree, F. H. (1999). Liquid-liquid phase transformation in carbon. *Physical Review Letters*, 82:4659–4662.

Glotzer, S. C. and Coniglio, A. (1994). Self-consistent solution of phase separation with competing interactions. *Physical Review. E*, 50:4241–4244.

Glotzer, S. C., Di Marzio, E. A., and Muthukumar, M. (1995). Reaction-Controlled Morphology of Phase-Separating Mixtures. *Physical Review Letters*, 74(11):2034–2037.

Glotzer, S. C., Stauffer, D., and Jan, N. (1994). Monte Carlo simulations of phase separation in chemically reactive binary mixtures. *Physical Review Letters*, 72(26):4109–4112.

Goncharov, A. F. and Geballe, Z. M. (2017). Comment on "evidence of a first-order phase transition to metallic hydrogen". *Physical Review. B*, 96:157101.

Henry, L., Mezouar, M., Garbarino, G., Sifré, D., Weck, G., and Datchi, F. (2020). Liquid–liquid transition and critical point in sulfur. *Nature*, 584:382–386.

Heuer, H.-O. (1993a). Critical crossover phenomena in disordered ising systems. *Journal of Physics A: Mathematical and General,* 26(6):L333–L339.

Heuer, H.-O. (1993b). Critical crossover phenomena in disordered ising systems. *Journal of Physics A: Mathematical and General*, 26:1333–1339.

Hildebrand, J. and Scott, R. (1962). *Regular Solutions.* Prentice-Hall international series in chemistry. Prentice-Hall.

Hinz, J., Karasiev, V. V., Hu, S. X., Zaghoo, M., Mejía-Rodríguez, D., Trickey, S. B., and Calderín, L. (2020). Fully consistent density functional theory determination of the insulator-metal transition boundary in warm dense hydrogen. *Physical Review Research*, 2:032065.

Hohenberg, P. C. and Halperin, B. I. (1977). Theory of dynamic critical phenomena. *Reviews of Modern Physics*, 49(3):435–479.

Holten, V. and Anisimov, M. A. (2012). Entropy-driven liquid–liquid separation in supercooled water. *Scientific Reports*, 2:713.

Holten, V., Palmer, J. C., Poole, P. H., Debenedetti, P. G., and Anisimov, M. A. (2014). Two-state thermodynamics of the st2 model for supercooled water. *Journal of Chemical Physics,* 104502.

Huang, K. (1987a). *Statistical Mechanics.* John Wiley and Sons, Inc., 2nd edition.

Huang, K. (1987b). *Statistical Mechanics.* John Wiley and Sons, Inc., 2nd edition.

Huggins, M. L. (1941). Solutions of long chain compounds. *J. Chem. Phys.*, 9:440.

Jagla, E. A. (2001). Liquid-liquid equilibrium for monodisperse spherical particles. *Physical Review. E*, 63:061501.

Katayama, Y., Inamura, Y., Mizutani, T., Yamakata, M., Utsumi, W., and Shimomura, O. (2004). Macroscopic separation of dense fluid phase and liquid phase of phosphorus. *Science*, 306(5697):848–851.

Katayama, Y., Mizutani, T., Utsumi, W., Shimomura, O., Yamakata, M., and ichi Funakoshi, K. (2000). A first-order liquid–liquid phase transition in phosphorus. *Nature*, 403:170–173.

Kawasaki, K. (1966). Diffusion Constants near the Critical Point for Time-Dependent Ising Models. I. *Physical Review*, 145(1):224–230.

Kim, D., Kim, W., Park, E., Mattern, N., and Eckert, J. (2013). Phase separation in metallic glasses. *Progress in Materials Science*, 58(8):1103–1172.

Kim, K. H., Amann-Winkel, K., Giovambattista, N., Späh, A., Perakis, F., Pathak, H., Parada, M. L., Yang, C., Mariedahl, D., Eklund, T., Lane, T. J., You, S., Jeong, S., Weston, M., Lee, J. H., Eom, I., Kim, M., Park, J., Chun, S. H., Poole, P. H., and Nilsson, A. (2020). Experimental observation of the liquid-liquid transition in bulk supercooled water under pressure. *Science*, 370(6519):978–982.

Kim, Y. C., Anisimov, M. A., Sengers, J. V., and Luijten, E. (2003). Crossover Critical Behavior in the Three-Dimensional Ising Model. *Journal of Statistical Physics*, 110(3):591–609.

Kogut, J. B. (1979). An introduction to lattice gauge theory and spin systems. *Reviews of Modern Physics*, 51(4):659–713.

Kozhevnikov, V. F., Payne, W. B., Olson, J. K., McDonald, C. L., and Inglefield, C. E. (2004). Physical properties of sulfur near the polymerization transition. *Journal of Chemical Physics,* 121.

Kubo, R. (1988). *Statistical Mechanics: An Advanced Course with Problems and Solutions*. North-Holland Physics Publishing, 7th edition.

Kumar, P., Buldyrev, S. V., Sciortino, F., Zaccarelli, E., and Stanley, H. E. (2005). Static and dynamic anomalies in a repulsive spherical ramp liquid: Theory and simulation. *Physical Review. E*, 72:021501.

Lamorgese, A. and Mauri, R. (2016). Spinodal decomposition of chemically reactive binary mixtures. *Physical Review. E*, 94:022605.

Langer, J. and Bar-on, M. (1973). Theory of early-stage spinodal decomposition. *Annals of Physics*, 78(2):421–452.

Langer, J. S., Bar-on, M., and Miller, H. D. (1975). New computational method in the theory of spinodal decomposition. *Physical Review A*, 11(4):1417–1429.

Lascaris, E., Hemmati, M., Buldyrev, S. V., Stanley, H. E., and Angell, C. A. (2014a). Search for a liquid-liquid critical point in models of silica. *Journal of Chemical Physics*, 140:224502.

Lascaris, E., Hemmati, M., Buldyrev, S. V., Stanley, H. E., and Angell, C. A. (2014b). Search for a liquid-liquid critical point in models of silica. *Journal of Chemical Physics*, 140:224502.

Lascaris, E., Hemmati, M., Buldyrev, S. V., Stanley, H. E., and Angell, C. A. (2015). Diffusivity and short-time dynamics in two models of silica. *Journal of Chemical Physical*, 142:104506.

Latinwo, F., Stillinger, F. H., and Debenedetti, P. G. (2016). Molecular model for chirality phenomena. *The Journal of Chemical Physics*, 145(15):154503.

Lee, T. D. and Yang, C. N. (1952). Statistical Theory of Equations of State and Phase Transitions. II. Lattice Gas and Ising Model. *Physical Review*, 87(3):410–419.

Lefever, R., Carati, D., and Hassani, N. (1995). Comment on "Monte Carlo Simulations of Phase Separation in Chemically Reactive Binary Mixtures". *Physical Review Letters*, 75(8):1674–1674.

Li, Y. I. and Cates, M. E. (2020). Non-equilibrium phase separation with reactions: a canonical model and its behaviour. *Journal of Statistical Mechanics: Theory and Experiment*, 2020(5):053206.

Lide, D. R. (2003). *CRC Handbook of Chemistry and Physics*. CRC Press, Boca Raton, FL, 85 edition.

Loerting, T., Fuentes-Landete, V., Handle, P. H., Seidl, M., Amann-Winkel, K., Gainaru, C., and Böhmer, R. (2015). The glass transition in high-density amorphous ice. *Journal of Non-Crystalline Solids*, 407:423–430.

Longo, T. J. and Anisimov, M. A. (2021). A mean field theory of phase transitions affected by interconversion. *ArXiv*.

Longo, T. J. and Anisimov, M. A. (2022). Phase transitions affected by natural and forceful molecular interconversion. *Journal of Chemical Physics*, 156:084502.

Luo, J., Xu, L., Angell, C. A., Stanley, H. E., and Buldyrev, S. V. (2015). Physics of the jagla model as the liquid-liquid coexistence line slope varies. *Journal of Chemical Physics*, 142:224501.

Luo, K. (2006). The morphology and dynamics of polymerization-induced phase separation. *European Polymer Journal*, 42(7):1499–1505.

Mazenko, G. F. and Valls, O. T. (1984). Theory of domain growth in an order-disorder transition. *Physical Review B*, 30(11):6732–6748.

McWilliams, R. S., Dalton, D. A., Mahmood, M. F., and Goncharov, A. F. (2016). Optical properties of fluid hydrogen at the transition to a conducting state. *Physical Review Letters*, 116:255501.

Metropolis, N. and Ashenhurst, R. L. (1963). Basic Operations in an Unnormalized Arithmetic System. *IEEE Transactions on Electronic Computers*, EC-12(6):896–904.

Morales, M. A., Pierleoni, C., Schwegler, E., and Ceperley, D. M. (2010). Evidence for a first-order liquid-liquid transition in high-pressure hydrogen from ab initio simulations. *Proceedings of the National Academy of Science*, 107(29):12799–803.

Ohta, K., Ichimaru, K., Einaga, M., Kawaguchi, S., Shimizu, K., Matsuoka, T., Hirao, N., and Ohishi, Y. (2015). Phase boundary of hot dense fluid hydrogen. *Scientific Reports*, 5(16560).

Petsev, N. D., Stillinger, F. H., and Debenedetti1, P. G. (2021). Effect of configuration-dependent multi-body forces on interconversion kinetics of a chiral tetramer model. *Journal of Chemical Physics,* 155:084105.

Pierleoni, C., Morales, M. A., Rillo, G., Holzmann, M., and Ceperley, D. M. (2016). Liquid–liquid phase transition in hydrogen by coupled electron–ion Monte Carlo simulations. *Proceedings of the National Academy of Sciences*, 113(18):4953–57.

Plašienka, D., Cifra, P., and Martoňák, R. (2015). Structural transformation between long and short-chain form of liquid sulfur from ab initio molecular dynamics. *Journal of Chemical Physics*, 142:154502–154512.

Poole, P. H., Grande, T., Angell, C. A., and McMillan, P. F. (1997). Polymorphic phase transitions in liquids and glasses. *Science*, 275:322–323.

Poole, P. H., Sciortino, F., Essmann, U., and Stanley, H. E. (1992). Phase behavior of metastable water. *Nature*, 360:324–328.

Povodyrev, A. A., Anisimov, M. A., and Sengers, J. V. (1999). Crossover Flory model for phase separation in polymer solutions. *Physica A: Statistical Mechanics and its Applications*, 264(3):345–369.

Press, W. H., Teukolsky, S. A., Vetterling, W. T., and Flannery, B. P. (2007). *Numerical Recipes: The Art of Scientific Computing.* Cambridge Univesity Press, Cambridge, United Kingdom, 3rd edition.

Rapaport, D. C. (2004). *The Art of Molecular Dynamics Simulation.* Cambridge University Press, Cambridge, UK, second edition.

Ricci, F., Stillinger, F. H., and Debenedetti, P. G. (2013). A computational investigation of attrition-enhanced chiral symmetry breaking in conglomerate crystals. *Journal of Chemical Physics*, 139:174503.

S. Chapman, T. C. (1970). *The Art of Molecular Dynamics Simulation*. Cambridge University Press, Cambridge, UK, third edition.

Saika-Voivod, I., Sciortino, F., Grande, T., and Poole, P. H. (2004). Phase diagram of silica from computer simulation. *Physical Review. E*, 70:061507.

Sastry, S. and Angell, C. A. (2003a). Liquid–liquid phase transition in supercooled silicon. *Nature Materials*, 2:739–743.

Sastry, S. and Angell, C. A. (2003b). Liquid–liquid phase transition in supercooled silicon. *Nature Materials*, 2:739–743.

Sauer, G. E. and Borst, L. B. (1967). Lambda transition in liquid sulfur. *Science*, 158(3808):1567–1569.

Schmitt, A. (2015). Introduction to superfluidity. volume 888 of *Lecture Notes in Physics*. Springer International Publishing, Cham.

Schwarz, H. A. (1972). *Gesammelte mathematische Abhandlungen*. American Mathematical Soc.

Sciortino, F. (2011). Liquid–liquid transitions: Silicon in silico. *Nature Physics,* 7:523–524.

Senthil, T. and Fisher, M. P. A. (2000). Z_2 gauge theory of electron fractionalization in strongly correlated systems. *Physical Review B*, 62(12):7850–7881.

Shumovskyi, N. A., Longo, T. J., Buldyrev, S. V., and Anisimov, M. A. (2021). Phase amplification in spinodal decomposition of immiscible fluids with interconversion of species. *Physical Review. E*, 103:L060101.

Shumovskyi, N. A., Longo, T. J., Buldyrev, S. V., and Anisimov, M. A. (2022). Modeling fluid polyamorphism through a maximum-valence approach. *Physical Review. E*, 106:015305.

Silvera, I. F., Zaghoo, M., and Salamat, A. (2017). Reply to "comment on 'evidence of a first-order phase transition to metallic hydrogen' ". *Phys. Rev. B*, 96:237102.

Skibinsky, A., Buldyrev, S. V., Franzese, G., Malescio, G., and Stanley, H. E. (2004). Liquid-liquid phase transitions for soft-core attractive potentials. *Physical Review. E*, 69:61206–15.

Speedy, R. J. and Debenedetti, P. G. (1994). The entropy of a network crystal, fluid and glass. *Molecular Physics*, (81).

Speedy, R. J. and Debenedetti, P. G. (1994). The entropy of a network crystal, fluid and glass. *Molecular Physics*, 81(1):237–249.

Speedy, R. J. and Debenedetti, P. G. (1996). The distribution of tetravalent network glasses. *Molecular Physics*, 88(5):1293–1316.

Stanely, H. E. (2013). *Liquid Polymorphism*, volume 152 of *Advances in Chemical Physics*. JohnWiley & Sons.

Stell, G. and Hemmer, P. C. (1972). Phase transitions due to softness of the potential core. *Journal of Chemical Physics*, 56:4274.

Stillinger, F. H. and Head-Gordon, T. (1993). Perturbational view of inherent structures in water. *Physical Review. E*, 47:2484–2490.

Strobl, G. R. (1985). Structure evolution during spinodal decomposition of polymer blends. *Macromolecules*, 18:559–563.

Takae, K. and Tanaka, H. (2020). Role of hydrodynamics in liquid–liquid transition of a single-component substance. *Proceedings of the National Academy of Sciences*, 117(9):4471–4479.

Tanaka, H. (2020). Liquid–liquid transition and polyamorphism. *Journal of Chemical Physics,* 153:130901.

Teubner, M. and Strey, R. (1987). Origin of the scattering peak in microemulsions. *Journal of Chemical Physics,* 87:3195.

Tobolsky, A. V. and Eisenberg, A. (1959). Equilibrium polymerization of sulfur. *Journal of the American Chemical Society,* 81(4):780–782.

Uralcan, B., Longo, T. J., Anisimov, M. A., Stillinger, F. H., and Debenedetti, P. G. (2021). Interconversion-controlled liquid-liquid phase separation in a molecular chiral model. *Journal of Chemical Physics,* 155:204502.

Verdasca, J., Borckmans, P., and Dewel, G. (1995). Chemically frozen phase separation in an adsorbed layer. *Physical Review. E*, 52:R4616–R4619.

Vollhardt, D. and Wölfle, P. (1990). *The Superfluid Phases of Helium 3*. Taylor and Francis, London, UK.

Xu, A., Gonnella, G., and Lamura, A. (2004). Phase separation of incompressible binary fluids with lattice Boltzmann methods. *Physica A: Statistical Mechanics and its Applications*, 331(1):10–22.

Xu, L., Buldyrev, S. V., Angell, C. A., and Stanley, H. E. (2006). Thermodynamics and dynamics of the two-scale spherically symmetric jagla ramp model of anomalous liquids. *Physical Review. E*, 74:031108.

Xu, L., Buldyrev, S. V., Giovambattista, N., Angell, C. A., and Stanley, H. E. (2009). A monatomic system with a liquid-liquid critical point and two distinct glassy states. *Journal of Chemical Physics*, 130:054505.

Xu, L., Kumar, P., Buldyrev, S. V., Chen, S.-H., Poole, P. H., Sciortino, F., and Stanley, H. E. (2005). Relation between the widom line and the dynamic crossover in systems with a liquid–liquid phase transition. *Proc. Natl. Acad. Sci.*, 102:16558.

Zaccarelli, E., Buldyrev, S. V., Nave, E. L., Moreno, A. J., Saika-Voivod, I., Sciortino, F., and Tartagliae, P. (2005). Model for reversible colloidal gelation. *Physical Review Letters*, 94:218301.

Zaghoo, M., Salamat, A., and Silvera, I. F. (2016). Evidence of a first-order phase transition to metallic hydrogen. *Physical Review B*, 93:155128.

Zaghoo, M. and Silvera, I. F. (2017). Conductivity and dissociation in liquid metallic hydrogen and implications for planetary interiors. *Proceedings of the National Academy of Sciences of the United States of America,* 114(45): 11873–11877.